



UNIVERSIDADE ESTADUAL DE CAMPINAS
Faculdade de Engenharia Mecânica

GABRIELA PEREIRA TOLEDO

Modeling for Pressure Waves Propagation Velocity in Slug Flow

Modelagem para a Velocidade de Propagação de Ondas de Pressão em Escoamentos Padrão Golfadas

CAMPINAS
2023

GABRIELA PEREIRA TOLEDO

Modeling for Pressure Waves Propagation Velocity in Slug Flow

Modelagem para a Velocidade de Propagação de Ondas de Pressão em Escoamentos Padrão Golfadas

Dissertation presented to the School of Mechanical Engineering of the University of Campinas in partial fulfillment of the requirements for the degree of Master in Mechanical Engineering in the area of Thermal and Fluids.

Dissertação apresentada à Faculdade de Engenharia Mecânica da Universidade Estadual de Campinas como parte dos requisitos exigidos para a obtenção do título de Mestra em Engenharia Mecânica, na Área de Térmica e Fluidos.

Orientador: Prof. Dr. Ricardo Augusto Mazza

ESTE TRABALHO CORRESPONDE À VERSÃO FINAL DA DISSERTAÇÃO DEFENDIDA PELA ALUNA GABRIELA PEREIRA TOLEDO, E ORIENTADA PELO PROF. DR. RICARDO AUGUSTO MAZZA.

**CAMPINAS
2023**

Ficha catalográfica
Universidade Estadual de Campinas
Biblioteca da Área de Engenharia e Arquitetura
Rose Meire da Silva - CRB 8/5974

T575m Toledo, Gabriela Pereira, 1997-
Modeling for pressure waves propagation velocity in slug flow / Gabriela Pereira Toledo. – Campinas, SP : [s.n.], 2023.

Orientador: Ricardo Augusto Mazza.
Dissertação (mestrado) – Universidade Estadual de Campinas, Faculdade de Engenharia Mecânica.

1. Escoamento bifásico. 2. Escoamento intermitente. 3. Propagação de ondas. 4. Escoamento instável (Dinâmica dos fluidos). 5. Espectro de frequência. I. Mazza, Ricardo Augusto, 1969-. II. Universidade Estadual de Campinas. Faculdade de Engenharia Mecânica. III. Título.

Informações Complementares

Título em outro idioma: Modelagem para a velocidade de propagação de ondas de pressão em escoamentos padrão golfadas

Palavras-chave em inglês:

Two-phase flow

Slug flow

Waves propagation

Transient flow (Fluid dynamics)

Frequency spectrum

Área de concentração: Térmica e Fluidos

Titulação: Mestra em Engenharia Mecânica

Banca examinadora:

Ricardo Augusto Mazza [Orientador]

Flávio de Campos Bannwart

Rigoberto Eleazar Melgarejo Morales

Data de defesa: 12-04-2023

Programa de Pós-Graduação: Engenharia Mecânica

Identificação e informações acadêmicas do(a) aluno(a)

- ORCID do autor: <https://orcid.org/0000-0001-8920-6256>

- Currículo Lattes do autor: <http://lattes.cnpq.br/1621649731623023>

UNIVERSIDADE ESTADUAL DE CAMPINAS
FACULDADE DE ENGENHARIA MECÂNICA
DISSERTAÇÃO DE MESTRADO ACADÊMICO

Modeling for Pressure Waves Propagation Velocity in Slug Flow

Modelagem para a Velocidade de Propagação de Ondas de Pressão em Escoamentos Padrão Golfadas

Autora: Gabriela Pereira Toledo

Orientador: Prof. Dr. Ricardo Augusto Mazza

A Banca Examinadora composta pelos membros abaixo aprovou esta Dissertação:

Prof. Dr. Ricardo Augusto Mazza, Presidente
DE/FEM/UNICAMP

Prof. Dr. Flávio de Campos Bannwart
DE/FEM/UNICAMP

Prof. Dr. Rigoberto Eleazar Melgarejo Morales
DAMEC/UTFPR

A Ata de Defesa com as respectivas assinaturas dos membros encontra-se no SIGA/Sistema de Fluxo de Dissertação/Tese e na Secretaria do Programa da Unidade.

Campinas, 12 de abril de 2023.

Agradecimentos

Acredito que tudo que conquistamos não são frutos apenas dos nossos esforços. Também incluem o esforço e dedicação daqueles que nos cercam e estão do nosso lado. Com o desenvolvimento desse projeto não foi diferente. Tive apoio direto e indireto de muitas pessoas queridas que não posso deixar de agradecer.

Primeiramente eu agradeço a Deus pela minha vida e por todas as oportunidades que tive ao longo dela. Por se fazer presente todos os dias por meio das pessoas e por ter me concedido saúde e disposição para buscar meus objetivos.

Também agradeço imensamente à minha família. Aos meus pais, Martinha e Antônio, por todo amor, dedicação, apoio em todas as decisões que já tomei e por se esforçarem para me dar as oportunidades que não tiveram. Aos meus avós, por todo carinho, cuidado e por comemorarem comigo cada passo da minha vida. Gostaria de agradecer em especial à minha mãe e à minha avó, Terezinha, por serem mulheres exemplo e por incentivarem os meus estudos desde quando eu era criança. Agradeço também ao meu irmão, Geraldo, por todo cuidado e parceria ao longo da vida. Por fim, ao meu namorado, Kairon, por todo companheirismo, incentivo e apoio em todos os momentos.

Aos meus amigos, especialmente aqueles que se fizeram presentes ao longo do mestrado. Vocês foram essenciais nos momentos que eu precisei de incentivo ou de descontração.

Aos professores que fizeram parte da minha trajetória, por contribuírem na minha formação técnica e pessoal e compartilharem conhecimentos que levo para a vida. Em especial, agradeço ao meu orientador, Prof. Dr. Ricardo Mazza, pela oportunidade em desenvolver este trabalho, pela paciência e pelos ensinamentos compartilhados ao longo desses dois anos.

Por fim, agradeço à CAPES pelo provimento da minha bolsa de mestrado. O presente trabalho foi realizado com apoio da Coordenação de Aperfeiçoamento de Pessoal de Nível Superior - Brasil (CAPES) - Código de Financiamento 001.

*“Não se espante com a altura do voo.
Quanto mais alto, mais longe do perigo.
Quanto mais você se eleva, mais tempo há de reconhecer uma pane.
É quando se está próximo do solo que se deve desconfiar.”*

Santos Dumont

Resumo

TOLEDO, Gabriela Pereira. Modelagem para a Velocidade de Propagação de Ondas de Pressão em Escoamentos Padrão Golfadas. Campinas: Faculdade de Engenharia Mecânica, Universidade Estadual de Campinas. 2023. 123p. Dissertação (Mestrado).

O padrão golfadas está presente em diversas situações industriais como no segmento de petróleo e químico. Devido à sua ampla aplicação, é necessário aprimorar constantemente o entendimento deste padrão. A mudança das condições operacionais induz um transiente no escoamento, gerando o fenômeno de propagação de ondas de pressão. Portanto, é essencial conhecer as características da onda de pressão para o projeto e operação dos sistemas, visto que grandes ondas de pressão podem causar a falha de equipamentos. Modelos simplificados não conseguem capturar a propagação da onda de pressão em escoamento padrão golfadas. Recentemente o modelo de dois fluidos vem sendo utilizado para preencher esta lacuna, apresentando bons resultados. No entanto, esses trabalhos não apresentaram como determinar a frequência, que é um parâmetro de entrada importante nesses modelos. Este estudo utiliza o modelo de seguimento de pistões para obter essa frequência de oscilação por meio de uma análise dos sinais de pressão e velocidade de translação da bolha ao longo do tempo usando a Transformada Discreta de Fourier (TDF). A frequência foi comparada com correlações para a frequência de passagem disponíveis na literatura. Além disso, a velocidade da onda de pressão estimada pelo modelo de dois fluidos com a frequência mencionada acima, foi comparada com os dados experimentais de Maria e Rosa (2016). O modelo de dois fluidos estimou a velocidade da onda de pressão com um desvio médio de 17% e com desvio menor que 30% para todos os casos usando o resultado de frequência da análise da TDF. Utilizando as correlações de frequência de passagem é obtido um desvio médio semelhante. O método proposto para determinar a frequência de oscilação se mostrou apropriado para o modelo de dois fluidos capturar a velocidade de propagação de ondas em padrão golfadas.

Palavras-chave: onda de pressão, velocidade da onda, frequência de oscilação, escoamento bifásico, escoamento intermitente, transiente, modelo de dois fluidos

Abstract

TOLEDO, Gabriela Pereira. Modeling for Pressure Waves Propagation Velocity in Slug Flow. Campinas: School of Mechanical Engineering, University of Campinas. 2023. 123p. Dissertation (Master).

The slug flow pattern occurs in many industrial situations, such as in the petroleum and chemical sectors. Because of the wide occurrence of this pattern, a constant improvement in understanding the slug flow behavior is necessary. Changes in the operational conditions induce a flow transient, generating the pressure wave propagation phenomenon. Therefore, knowing the pressure propagation characteristics is essential for designing and managing the systems since great pressure waves may cause equipment failure. Simple models cannot capture the pressure wave propagation in slug flow. The Two-Fluid Model (TFM) has been used to fill this gap with good results; however, these works did not present how to set up the frequency, an important input parameter in these models. This study uses the slug tracking model to assess this frequency, using signal analysis of pressure and bubble nose velocity over time using the Discrete Fourier Transform (DFT). The frequency is compared to the correlations for the frequency of passage. Moreover, the pressure propagation velocity using the TFM with the frequency mentioned above is compared with the experimental campaign of Maria and Rosa (2016). Using the frequency from the DFT analysis, the two-fluid model could predict the experimental pressure wave velocity with a mean deviation of 17% and less than 30% deviation for all cases. In addition, using the frequency correlations, a similar mean deviation was obtained. The proposed method to determine the oscillation frequency proved appropriate for the two-fluid model to capture the pressure wave propagation velocity in slug flow.

Keywords: pressure wave, wave velocity, oscillation frequency, two-phase flow, slug flow, transient, two-fluid model

List of Figures

Figure 1.1. Flow patterns for horizontal gas-liquid flows. From top to bottom: bubbly, stratified, slug, and annular.	18
Figure 1.2. Flow patterns for vertical gas-liquid flow. From left to right: bubbly, slug, churn, and annular.	19
Figure 1.3. Representation of the elongated bubble and liquid slug in a unit cell.....	20
Figure 2.1. Diagram of the two-phase flow models.	27
Figure 2.2. The unit cell for inclined and horizontal flow.....	28
Figure 2.3. Idealized model of slug flow of Henry et al. (1971).....	31
Figure 3.1. Properties and cell indexes in the slug tracking model - Rosa et al. (2015) adapted.	45
Figure 4.1. Experimental test section from Maria and Rosa (2016).....	47
Figure 4.2. Pressure signals as a function of time for Test #1 at Station S#1: — random, and — periodic conditions. The last two graphs also show a zoom of the signal periodic oscillation.	50
Figure 4.3. Pressure signals as a function of time for Test #1 from Gonçalves and Mazza (2022). From top to bottom Stations S#1, S#2, S#3, and S#4.	51
Figure 4.4. Pressure signals as a function of time for Test #2 from Gonçalves and Mazza (2022). From top to bottom Stations S#1, S#2, S#3, and S#4.	52
Figure 4.5. Pressure signals as a function of time for Test #3 from Gonçalves and Mazza (2022). From top to bottom Stations S#1, S#2, S#3, and S#4.	53
Figure 4.6. Pressure signals as a function of time for Test #4 from Gonçalves and Mazza (2022). From top to bottom Stations S#1, S#2, S#3, and S#4.	54
Figure 4.7. Method flowchart.	58
Figure 5.1. Pressure wave velocity as a function of frequency: —■— run #1, —●— run #2, —◆— run #3, —▲— run#4.....	62
Figure 5.2. Normalized pressure wave velocity as a function of frequency: — Li et al. (2022a), — $J_L = 0.60$ m/s and $J_G = 0.30$ m/s, and — $J_L = 2.10$ m/s and $J_G = 0.60$ m/s.....	63
Figure 5.3. Signals power in the frequency spectrum of pressure signal for Test #1 at Station S#1: — random condition, and — periodic condition.	64

Figure 5.4. The fundamental frequency and harmonics of the pressure signal at the second steady state for Test #1 at Station S#1; f_0 is the fundamental frequency, and H indicates the harmonics.	65
Figure 5.5. The frequency spectrum of the pressure signal at the second steady state for Test #1 for all stations: — pressure, and — bubble nose velocity signals.	67
Figure 5.6. The frequency spectrum of the pressure signal at the second steady state for Tests #2 to #4 for all stations: from top to bottom #2, #3 and, #4.	68
Figure 5.7. Comparison between the frequency predicted by the correlations and the frequency found via DFT.	71
Figure 5.8. Comparison between the experimental data with the numerical prediction of the pressure wave velocity.	73
Figure 5.9. Flow pattern map for horizontal flow contains five patterns: dispersed bubble, intermittent, annular, stratified smooth, and stratified wavy; × indicates the points evaluated in the case study.	75
Figure 5.10. Liquid’s superficial velocity influence in the pressure wave velocity curve; Case A has $J_L = 0.3$ m/s and increases progressively by 0.3 m/s until Case G, where $J_L = 2.1$ m/s.	77
Figure 5.11. Maximum pressure wave velocity versus the prediction by previous models.	80
Figure 5.12. Attenuation coefficient for the four tests as a function of the oscillation frequency: —■— run #1, —●— run #2, —◆— run #3, and —▲— run #4.	81
Figure B.1. Properties and index of the cells in the slug tracking model - Rosa et al. (2015) adapted.	110

List of Tables

Table 4.1. Experimental test grid from Maria and Rosa (2016).	48
Table 4.2. Flow properties at the second steady state for each run.	55
Table 4.3. Fluids' properties.	56
Table 5.1. Fundamental frequency for the four tests and the ratio of the superficial velocities at the second steady state.....	69
Table 5.2. The average frequency of passage prediction and its normalized RMS deviation.	70
Table 5.3. Numerical and experimental pressure wave velocity and the deviation between them.	72
Table 5.4. Predicted pressure wave velocity, the relative deviation with the experimental data from Maria and Rosa (2016), and the average relative deviation for each correlation.	74
Table 5.5. Case study's points and the void fraction prediction by the drift relation.....	76
Table 5.6. Pressure wave propagation velocity at 0.5 and 30 Hz and the difference between them.	78
Table 5.7. Comparison of the pressure wave velocity predicted by previous models and the maximum value from the two-fluid model.....	79

Notations

Latin Letters

A – cross-section	[m ²]
a _G – sound velocity propagation in the gas phase	[m/s]
a _L – sound velocity propagation in the liquid phase	[m/s]
C _f – Fanning friction factor	[-]
c _{dg} – drag coefficient	[-]
c _{vm} – virtual mass coefficient	[-]
c _p – pressure propagation velocity	[m/s]
C ₀ – distribution parameter	[-]
C _∞ – drift coefficient	[-]
D – pipe inside diameter	[m]
f – frequency	[Hz]
f ₀ – fundamental frequency	[Hz]
F – force	[N]
Fr – Froude's number	[-]
F _s – sampling frequency	[Hz]
g – gravity	[m.s ⁻²]
h – height	[m]
H – harmonic	[Hz]
J – superficial velocity	[m.s ⁻¹]
k – spring stiffness	[N. m ⁻¹]
K – Bulk modulus	[kPa]
L – length	[m]
m – mass	[kg]
\dot{m} – mass flow rate	[kg.s ⁻¹]
N – number of samples	[-]
P – pressure	[kPa]
\dot{Q} – volumetric flow rate	[m ³ .s ⁻¹]
R _b – bubble radius	[m]

S – wetted perimeter	[m]
t – time	[s]
T – time window	[s]
u – absolute velocity	[m.s ⁻¹]
U _T – Taylor bubble nose velocity	[m.s ⁻¹]
v – relative velocity using a reference moving with the bubble nose velocity (U _T)	[m.s ⁻¹]
V – phase in situ velocity	[m.s ⁻¹]
x – tail position of the elongated gas bubble	[m]
y – nose position of the elongated gas bubble	[m]
z – axial position	[m]
Z – generic variable	[m]

Greek Letters

α – void fraction	[-]
β – intermittence factor	[-]
γ – polytropic constant	[-]
Δ - interval	[-]
ε – pipe roughness	[m]
ϕ – frequency of passage	[Hz]
κ – wave number	[rad.m ⁻¹]
θ – pipe inclination	[rad]
μ – dynamic viscosity	[Pa.s]
ξ – represents the center of pressure coordinate	[-]
ρ – density	[kg.m ⁻³]
σ – relative deviation	[-]
τ – shear stress	[N.m ⁻²]
ω – angular frequency	[rad.s ⁻¹]

Subscripts

b – dispersed bubbles
d – drift
D – drag

f – liquid film region
G – gas phase
GL – gas-liquid interface
i – gas-liquid interface
j – cell index
k - phase
L – liquid phase
M –gas-liquid mixture in the liquid slug
S – liquid slug
U – unit cell
vm – virtual mass
WG – wall-gas interface
WL – wall-liquid interface

Abbreviations

CFD – Computational Fluid Dynamics
DFM – Drift-Flux Model
DFT – Discrete Fourier Transform
FFT – Fast Fourier Transform
HFM – Homogeneous Flow Model
ID – Inside Diameter
MPT – Mud Pulse Telemetry
MWD – Measurement While Drilling
OLGA – Oil and Gas Simulator
PLAC – Pipeline Analysis Code
TFM – Two-Fluid Model
TUFFP – Tulsa University Fluid Flow Projects

Contents

1	INTRODUCTION.....	17
1.1	Objectives	21
1.2	Research outline.....	22
2	LITERATURE REVIEW.....	23
2.1	Multiphase flow variables.....	23
2.2	Slug flow models	27
2.3	Pressure propagation in multiphase flow.....	30
2.4	Two-fluid models.....	36
2.5	Literature review gaps	38
3	MATHEMATICAL MODEL	40
3.1	Two-fluid model	40
3.2	Slug tracking model	44
4	SIMULATIONS AND FREQUENCY ANALYSIS	47
4.1	Setup	47
4.2	Boundary conditions	48
4.3	Discrete Fourier Transform (DFT)	56
4.4	Method flowchart.....	57
4.5	Frequency of passage correlations	58
5	RESULTS.....	61
5.1	Model behavior	61
5.2	Frequencies	63
5.3	Pressure wave propagation	71

5.4 Case study	74
5.5 Comparison with previous models	78
5.6 Attenuation coefficient	80
6 CONCLUSIONS	82
References.....	84
APPENDIX A – Review of pressure wave propagation velocity	91
APPENDIX B – Two-fluid model mathematical details	103
Closure relations	103
Two-fluid model	105
APPENDIX C – Slug tracking model details	110
Liquid and gas mass equation.....	112
Momentum equation	113
APPENDIX D – Two-fluid model code on Wolfram Mathematica	119
APPENDIX E – MATLAB code to obtain the FFT	122

1 INTRODUCTION

The feature of the multiphase flow is the presence of two or more phases. These phases may be immiscible liquids, pure substances, or a combination of miscible substances at the saturation point. Phase is any substance portion separated from the surrounding fluid by a tiny layer resulting from the interfacial tension. In the two-phase flow, the phases can be gas-liquid, liquid-liquid, or solid-liquid mixtures. A two-phase air-water flow is the focus of this study.

When two fluids flow in a pipe, the phases can arrange themselves in different flow patterns. These flow patterns depend on the fluids' superficial velocities and the pipe configuration, such as internal diameter and inclination. Understanding the flow patterns and their characteristics is essential for developing two-phase flow models since each flow pattern has its particular hydrodynamics.

Identifying a pattern is challenging because it relies on the observer's subjective judgment. That is why the number of flow patterns and their transition boundaries may differ among the authors. Nonetheless, some patterns are a consensus between them. Flow maps are used for pattern classification based on the proposed criteria. There are flow maps for horizontal, inclined, and vertical pipe orientation to help to identify the flow pattern for each pair of superficial velocities. Taitel and Dukler (1976) are one of the most accepted maps for horizontal flow, and Taitel et al. (1980) for vertical flow.

The main patterns for horizontal gas-liquid flows are bubbly, stratified, slug, and annular (BERTOLA, 2003; SHOHAM, 2006). Figure 1.1 shows the spatial configuration for the horizontal flow patterns. In addition, the following paragraphs describe each horizontal pattern shown in Fig. 1.1 from top to bottom:

Bubbly flow is featured by tiny spherical gas bubbles dispersed in the liquid. In the case of horizontal flow, these bubbles tend to concentrate in the upper part of the pipe due to buoyancy and may or may not coalesce. In this flow pattern, there is no slip between the phases and flow is considered homogenous.

Stratified flow is featured by the gas phase flowing above the liquid, showing a complete detachment between the two phases. This pattern occurs at low gas and liquid flow rates.

Slug flow is characterized by an alternated sequence of elongated bubbles and liquid slugs both in time and space. For the horizontal flows, the long bubble is eccentric and located

in the upper part of the pipe due to buoyancy. In this case, the aeration in the liquid slug is slight and can be neglected in most cases.

Annular flow corresponds to a gas core and a liquid film around the pipe wall. Furthermore, some liquid can flow as droplets in the gas core. This flow pattern occurs at high gas flow rates.

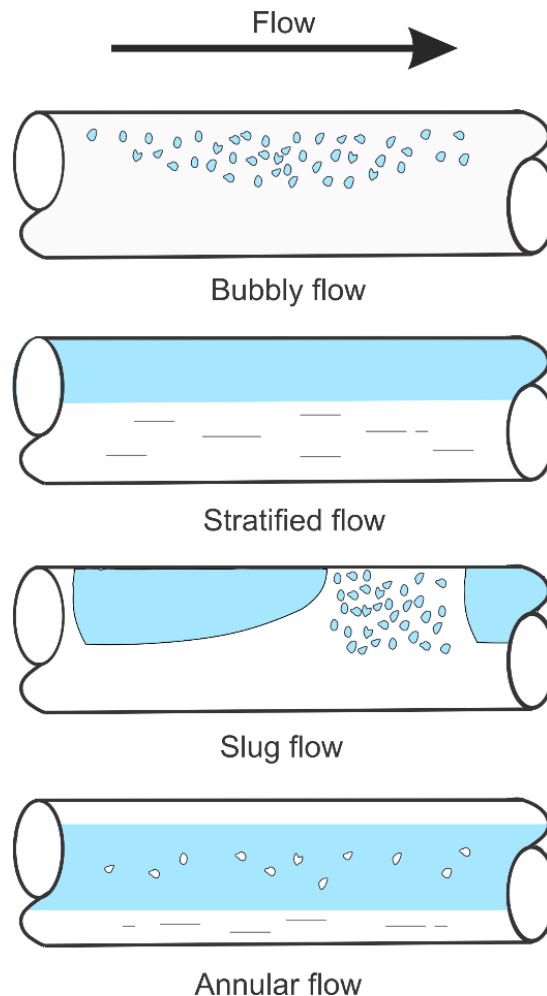


Figure 1.1. Flow patterns for horizontal gas-liquid flows. From top to bottom: bubbly, stratified, slug, and annular.

For vertical gas-liquid flow, the consensual patterns among the researchers are bubbly, slug, churn, and annular (HEWITT; HALL-TAYLOR, 1970; TAITEL et al., 1980). Figure 1.2 shows the patterns' spatial configurations for vertical flow. Moreover, the following paragraphs describe each vertical flow pattern in Fig. 1.2 from left to right:

Bubbly flow in vertical sections is featured by spherical gas bubbles evenly dispersed in the liquid or tending to concentrate in the center of the pipe.

Slug flow in an upward vertical orientation is characterized by an elongated bubble that carries most of the gas mass in the cell. This long bubble has a bullet shape known as the Taylor bubble. This Taylor bubble is concentric, and its diameter is almost equal to the pipe diameter. Unlike the horizontal case, the effects of the liquid slug aeration and the gas expansion are important.

Churn flow occurs when the superficial gas velocity increases, and the elongated gas bubbles deform, assuming an amorphous shape. This pattern is usually avoided in practical applications due to its complex hydrodynamics.

Annular flow in vertical inclinations is similar to the horizontal case.

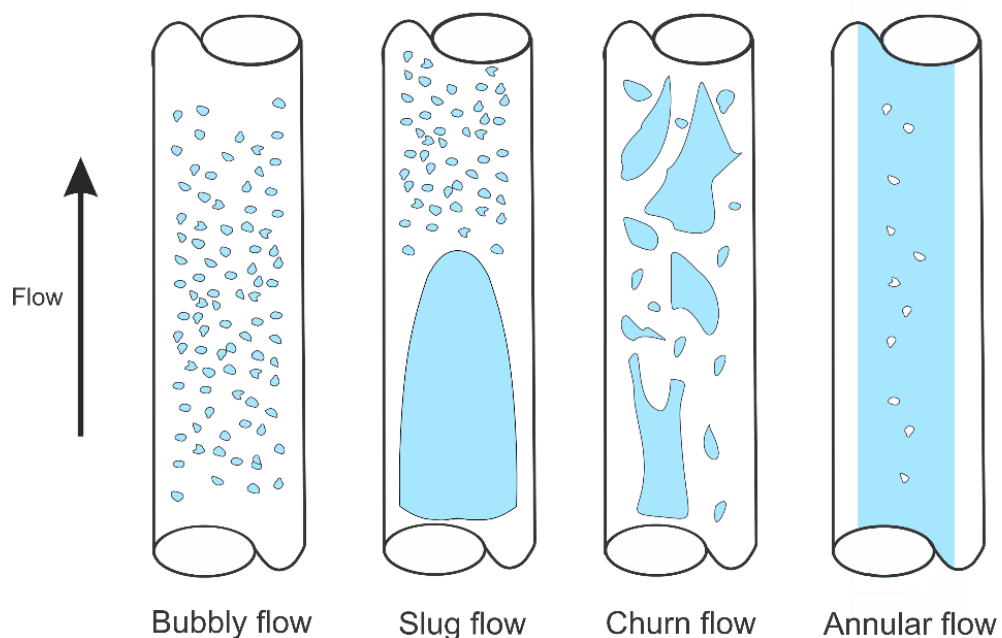


Figure 1.2. Flow patterns for vertical gas-liquid flow. From left to right: bubbly, slug, churn, and annular.

Among all these patterns, the slug flow plays an essential role in industry due to its occurrence in the petroleum, chemical, nuclear, and space industries (FERNANDES et al., 1983; SAIDJ et al., 2018; SHOHAM, 2006). As shown in Figs. 1.1 and 1.2, the slug flow contains all the other patterns. It consists of an alternated sequence of elongated bubbles and liquid slugs in time and space.

Wallis (1969) introduced the concept of a unit cell to describe the slug flow characteristics. A unit cell consists of an elongated bubble and an aerated liquid slug. Besides, it considers that all cells have the same properties along the pipe. Thus, this modeling assumes

that the slug flow has a periodic nature. Figure 1.3 shows a slug flow unit cell and its main structures.

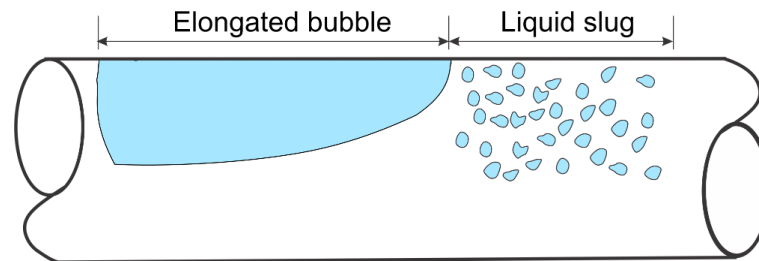


Figure 1.3. Representation of the elongated bubble and liquid slug in a unit cell.

Many authors employed this definition to develop their models for horizontal, slightly inclined, and vertical flows (ANDREUSSI et al., 1993; COOK; BEHNIA, 1997; DUKLER; HUBBARD, 1975; FERNANDES et al., 1983; ORELL; REMBRAND, 1986; SYLVESTER, 1987; KOKAL; STANISLAV, 1989; NICHOLSON et al., 1978; TAITEL; BARNEA, 1990). These models focus on predicting the slug flow behavior in a steady-state regime.

Transient operations frequently occur in the petroleum industry, such as the startup and shutdown of pipelines, gas kicks while well-drilling, pipeline rupture detection, and pigging, among other issues. Because of the industry's vast applications, studying the slug flow in transient regimes is necessary. According to Shoham (2006), a transient slug flow occurs when the inlet (as gas and liquid flow rates) or outlet conditions (as pressure) change. Fabre et al. (1995) showed that the flow properties, as pressure and void fractions, propagate as waves when the inlet or outlet conditions change abruptly. According to Xu and Gong (2008), the propagation of great pressure waves can cause failure in the entire pipe system. In addition, they suggested that predicting the pressure pulse propagation in long piping systems is challenging due to gas compressibility, flow pattern change, and energy and mass transfers.

The pressure propagation velocity is a crucial parameter in petroleum operations, such as mud pulse telemetry (MPT), gas influx detection, and well-dynamic control response (LI et al., 2016). Many authors have focused their studies on pressure propagation velocity prediction using the mixture's models since the '70s (AKAGAWA et al., 1982; CAUSSADE et al., 1989; FABRE et al., 1995; SAMUEL MARTIN; PADMANABHAN, 1979; WALLIS, 1969). However, the mixture models suppose the gas phase is evenly distributed into the liquid. Therefore, these models do not capture the property changes due to the elongated bubble.

The two-fluid model has been recently used to predict the pressure propagation velocity and attenuation coefficient (LI et al., 2022a, 2012, 2016; LI et al., 2022b; LIN et al., 2013).

Their models need frequency, void fraction, and superficial velocities of the phases as input variables. Superficial velocities are operational conditions, and the void fraction is a known variable from the drift relationship; however, there is no information about how to obtain the frequency. For example, they used a frequency bigger than the slug flow oscillation frequency as input for all void fractions. The present research was motivated by this gap. We aim to obtain a method to determine the oscillation frequency in slug flow to use as an input parameter in the two-fluid model. We suggest using the slug tracking model to assess the slug flow oscillation frequency. Therefore, this research analyzes the oscillation frequency in slug flow and obtains the pressure wave propagation velocity in a two-phase air-water horizontal flow. The numerical results are compared with the experimental outcomes in Maria and Rosa (2016) of a horizontal test section of 26 mm ID and 1,009D long.

1.1 Objectives

This work aims at developing a straightforward method to obtain the pressure propagation velocity in slug flow. The focus will be on the oscillation frequency analysis and its use in the two-fluid model. The following specific objectives must be accomplished to achieve the fundamental goal:

- Assess the signals of the nose bubble velocity and pressure through time using slug tracking simulations;
- Determine the oscillation frequency of slug flow by analyzing the signals using the discrete Fourier transform (DFT);
- Compare the oscillation frequency with different frequencies of passage correlations;
- Calculate the pressure wave propagation velocity and attenuation coefficient using the two-fluid model;
- Compare the numerical results with the experimental campaign of Maria and Rosa (2016) and previous models of pressure pulse velocity.

1.2 Research outline

This study is organized into six chapters. The first one introduced the study theme: the definition of multiphase flow, the flow patterns, the modeling in steady-state and transient regimes, the research motivation, and the objectives. The following five chapters are described next.

Chapter 2 - Literature review: This chapter reviews the multiphase flow variables, the slug flow models, including the slug tracking model, and the previous research in the transient slug focusing on those investigating the pressure wave velocity.

Chapter 3 - Mathematical model: This chapter describes the considerations and the mathematical formulations of the two-fluid and slug tracking models. This chapter also presents the pressure wave velocity equation and the numerical solution method.

Chapter 4 – Simulations and frequency analysis: This chapter describes the experimental setup from Maria and Rosa (2016) and the boundary conditions of the numerical simulations performed by Gonçalves and Mazza (2022). In addition, it presents the signal features and the methods to determine the frequency using the Discrete Fourier Transform (DFT). Finally, it presents nine literature correlations to predict the frequency of passage.

Chapter 5 – Results: This chapter shows the model sensitivity for different frequency values. In addition, it presents the frequency analysis and its results and discusses a more straightforward closure to the two-fluid model. It also shows the results for the pressure wave propagation and the comparison with the experimental data from Maria and Rosa (2016). Furthermore, a parametric analysis of the influence of the liquid's superficial velocity on the model is performed for the experimental point that presented the biggest RMS. This chapter presents the attenuation coefficient prediction for the experimental tests of Maria and Rosa (2016).

Chapter 6 – Conclusions: This chapter contains the conclusion of this research and suggestions for future studies.

2 LITERATURE REVIEW

This chapter contains four sections reviewing the features of the two-phase slug flow. Section 2.1 presents the main variables and notations in multiphase flow studies. Then, Section 2.2 examines the mixture and separated-phase models. In addition, it shows the unit cell definition and the slug tracking model. Section 2.3 reviews the transient modeling in two-phase flow, focusing on experimental and numerical works of pressure wave propagation. Section 2.4 treats the previous modeling of pressure propagation using the two-fluid model. Finally, Section 2.5. discusses the main works mentioned in this chapter, pointing out the main weaknesses of each one.

2.1 Multiphase flow variables

We first need to review notations and multiphase flow variables used in this work. The mass flow rate is the only property conserved in these types of flows. It is defined as the amount of mass flowing through a pipe's cross-sectional area per unity of time, according to Eq. (2.1):

$$\dot{m}_k = \frac{m_k}{\Delta t}, \quad (2.1)$$

where the subscript k indicates the phase. The total mass flow rate is the sum of the mass flow rate of each phase, as shown in Eq. (2.2):

$$\dot{m} = \sum \dot{m}_k . \quad (2.2)$$

The volumetric flow rate is the volume of fluid k flowing through a cross-sectional area per unit of time, as shown in Eq. (2.3):

$$\dot{Q}_k = \frac{V_k}{\Delta t}, \quad (2.3)$$

where ∇_k is the phase k volume. Likewise, in the case of the mass flow rate, the total volumetric flow rate is the sum of the volumetric flow rate of each phase, according to Eq. (2.4):

$$\dot{Q} = \sum \dot{Q}_k . \quad (2.4)$$

Another important variable in multiphase flow is superficial velocity. The superficial velocity is the ratio of the volumetric flow rate of each phase to the pipe's cross-sectional area, as in Eq. (2.5):

$$J_k = \frac{\dot{Q}_k}{A}, \quad (2.5)$$

where A is the pipe cross-sectional area. Equation (2.6) gives the total superficial velocity, which is the sum of each phase's superficial velocities:

$$J = \sum J_k . \quad (2.6)$$

There are many geometric definitions of void fractions from different averages, like the ensemble and time averages; however, all definitions have the same results in ergodic processes. The sum of the void fractions of each phase is the unit, as shown in Eq. (2.7):

$$\sum \langle \alpha_k \rangle = 1, \quad (2.7)$$

where the time average of the variable defines the average operator, as shown in Eq. (2.8):

$$\langle \rangle = \frac{1}{T} \int_0^T f(t) . dt . \quad (2.8)$$

As shown in Eq. (2.9), the volumetric void fraction is defined as the ratio of the volume occupied by the phase to the total measured volume. The quick-close valves' technique usually determines the experimental volumetric void fraction.

$$\langle \alpha_k \rangle^{\forall} = \frac{\forall_k}{\forall}. \quad (2.9)$$

The area-based void fraction is the ratio of the area occupied by the phase to the pipe cross-sectional area, as shown in Eq. (2.10). Optical methods can measure the experimental area void fraction.

$$\langle \alpha_k \rangle^A = \frac{A_k}{A}. \quad (2.10)$$

Considering that the two-phase flow is an ergodic process, the volumetric and area void fractions are the same:

$$\langle \alpha_k \rangle^{\forall} = \langle \alpha_k \rangle^A. \quad (2.11)$$

This study focuses on the gas-liquid two-phase flow. From here, subscript G indicates the gas phase, L is the liquid phase, f is the elongated bubble region, S is the liquid slug, and U is the unit cell.

The liquid hold-up definition complements the void fraction definition. While the void fraction determines the presence of the gas phase in a pipe's section, the liquid hold-up determines the presence of the liquid phase. Equations (2.12) and (2.13) show the hold-up in the liquid film region and the liquid slug for two-phase slug flows:

$$\langle R_f \rangle = 1 - \langle \alpha_f \rangle, \quad (2.12)$$

$$\langle R_S \rangle = 1 - \langle \alpha_S \rangle. \quad (2.13)$$

The average operator $\langle \rangle$ will be suppressed from now on for simplification.

The slug flow consists of an alternated sequence of elongated bubbles and liquid slugs. An elongated bubble and a liquid slug together form what is known as a unit cell. Thus, the length of a unit cell is the sum of the liquid film and the liquid slug lengths, as shown in Eq. (2.14):

$$L_U = L_f + L_s. \quad (2.14)$$

The intermittence factor is the ratio of the liquid film length to the unit cell length, as shown in Eq. (2.15):

$$\beta = \frac{L_f}{L_U}. \quad (2.15)$$

The slug flow frequency is the inverse of the transit time of a unit cell. This frequency is related to the nose bubble velocity and the unit cell length, as shown in the following:

$$\phi = \frac{U_T}{L_U}. \quad (2.16)$$

From the definition of phases, we can determine a model for the fluid properties based on the length-weighted average. Equation (2.17) shows the unit cell void fraction:

$$\alpha_U = \beta\alpha_f + (1 - \beta)\alpha_s. \quad (2.17)$$

Similarly, the void fraction-weighted average gives the mixture density and dynamic viscosity, as shown in Eqs. (2.18) and (2.19):

$$\rho_U = \alpha_U\rho_G + (1 - \alpha_U)\rho_L, \quad (2.18)$$

$$\mu_U = \alpha_U\mu_G + (1 - \alpha_U)\mu_L, \quad (2.19)$$

where ρ is the density and μ is the dynamic viscosity.

It is noteworthy that these definitions are valid only for immiscible fluids. The study of emulsions involves modeling it as a single fluid with unique properties that must be measured in the laboratory for each case.

2.2 Slug flow models

There are two categories of multiphase flow models: the flow mixture models and the separated flow models. The flow mixture models include the Homogeneous Flow Model (HFM) and the Drift-Flux Model (DFM). The Two-Fluid Model (TFM) is a separate flow model. Figure 2.1 shows the diagram of the two-phase flow models.

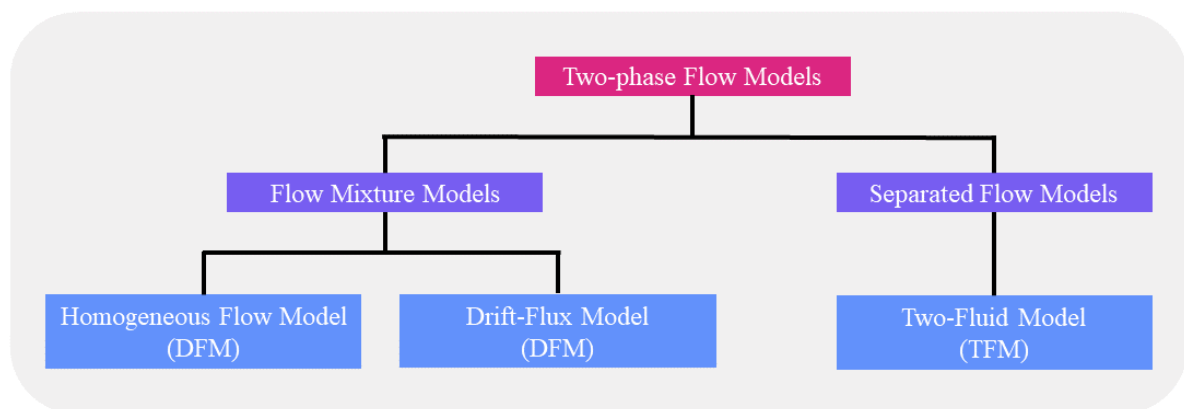


Figure 2.1. Diagram of the two-phase flow models.

The homogeneous flow model considers that the two-phase flow mixture behaves as a single pseudo-fluid with specific properties, given by the weighted average of the elongated bubble and liquid slug lengths. In this case, it assumes no-slip condition between the phases, and the two phases are well mixed and in equilibrium.

The drift-flux model is similar to the homogeneous flow model. However, it is an improvement over the HFM because it considers the slippage between the phases. The model uses the mixture's continuity, momentum, and energy equations. In addition, it requires one extra continuity equation for one of the phases. Therefore, the DFM consists of four equations plus a drift velocity closure relation.

The two-fluid model treats the two phases separately. The model includes the continuity, momentum, and energy equations for both phases, totaling six equations. Furthermore, it needs one closure relationship to obtain the interfacial shear stress.

The mixture models do not capture the abrupt properties variation caused by the elongated bubbles; thus, these models are unsuitable for studying the pressure wave propagation in slug flows. Omgba-Essama (2009) pointed out that the two-fluid model better represents the

dynamic interaction between the phases; consequently, this model is more suitable for studying wave propagation phenomena. In addition, Gonçalves and Mazza (2022) noted that a slug tracking approach is also a good option for studying this phenomenon because of its ability to capture the interaction between neighboring cells.

The slug flow consists of an intermittent sequence of elongated bubbles and liquid slugs. The studies on slug flow started with the definition of the unit cell proposed by Wallis (1969). The unit cell comprises an elongated bubble and a liquid slug, and the model assumes that the cell keeps its characteristics along the pipe. Figure 2.2 shows a unit cell and its variables for horizontal and slightly inclined flows. It is worth mentioning that the elongated bubble is concentric to the pipe for larger inclination angles and vertical flows.

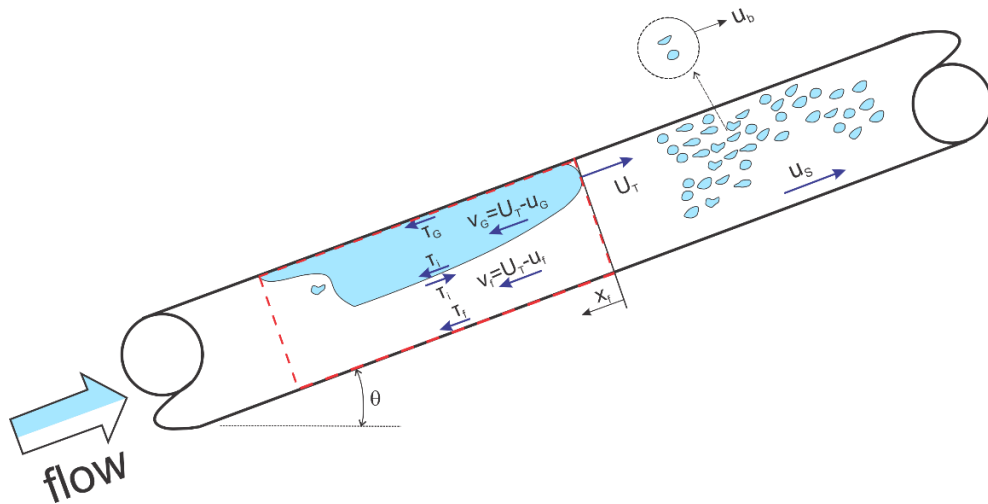


Figure 2.2. The unit cell for inclined and horizontal flow.

In Fig. 2.2, the liquid slug flow properties are the bubbles u_b and liquid slug u_s velocities. In addition, the film or elongated bubble region properties are the gas and liquid film relative velocities v_G and v_f . The shear stress is τ , and the subscripts G , i , and f mean the gas, interface, and liquid film, respectively.

Many authors used the unit cell concept to model the liquid film around the elongated bubble for horizontal and slightly inclined flows (ANDREUSSI et al., 1993; COOK; BEHNIA, 1997; DUKLER; HUBBARD, 1975; KOKAL; STANISLAV, 1989; NICHOLSON et al., 1978). In addition, Fagundes Netto et al. (1999) proposed a liquid film model specific to horizontal flows, and Fernandes et al. (1983) and Sylvester (1987) presented their models for vertical flows. Finally, Taitel and Barnea (1990) proposed a model suitable for horizontal, inclined, and vertical flows. Furthermore, it is currently the most accepted liquid film model.

The slug tracking model employs a transient control volume analysis based on the one-dimensional mass and momentum balances applied to a unit cell flowing throughout the pipe. The spatial integrals condense the mass and momentum into a point, representing the lumped properties of the j^{th} cell; nonetheless, the time analysis is continuous. The model tracks each cell down throughout the domain, capturing the evolution of the flow variables over time.

The approach of the slug tracking model started with Barnea and Taitel (1993). Earlier models could predict the slug length average; however, slug length has the characteristic of having a variance around its average value. The authors proposed a model capable of predicting the slug length distribution at any point along the pipe. They used two distribution types at the inlet: random and normal, and found that slug length distribution is not sensitive to the distribution at the entrance. They also found that their model agrees with the experimental data from van Hout et al. (1992) for upward vertical flow.

Zheng et al. (1994) developed a slug-tracking model to simulate the slug flow behavior in a hilly terrain pipeline using the liquid mass balance. The authors approached two cases: one in which the slugs maintain their shape when passing to another section, and the other when new slugs can be generated while others can dissipate, and the slug length can change. They compared the numerical results with experimental data of air-kerosene in a test section of 77.9 mm ID and 5,395D long with slope variation along its length. They found that the model could predict the mechanism of slug generation and dissipation.

Taitel and Barnea (1998) developed a Lagrangian model, i.e., capable of following the mass elements, and it is only time-dependent. They consider the gas compressibility and assume that all slugs at the inlet have the same length using a similar model to Barnea and Taitel (1993). However, the authors neglected the time derivative terms in the momentum balances. Their numerical results were for the case of horizontal air-water flow. They concluded that the significant gas compressibility effect occurs in the elongated bubble region.

Based on the model proposed by Taitel and Barnea (1998), Al-Safran et al. (2004) developed a transient slug tracking model to study the flow in hilly terrain pipes. They compared the numerical results with experimental data of horizontal air-oil flow of 50.8 mm ID and 840D long test section with slope variations. The comparison shows a good fitting between the experimental and the numerical results. The authors emphasize its capacity to predict the maximum slug length at the outlet with less than 8% deviation.

In addition, Wang et al. (2006) also developed a slug tracking model based on Taitel and Barnea's (1998) model; however, they consider the wake effect and the pressure drop caused by acceleration. The authors assumed that liquid slugs with random lengths entered the

test section and compared the results with experimental data from a horizontal air-water flow in a test section of 50 mm ID and 2,660D long. The model presented a good agreement in predicting the mean, maximum, and distribution slug length at 1,557D; however, the average slug length was underestimated at 2,609D, showing the model's difficulty in capturing the slug evolution as it flows along the pipe.

The slug-tracking model used in this research follows the formulation of Rosa et al. (2015). Their formulation includes all the terms considered in previous models plus the advective term. The model is capable of simulating horizontal and inclined flows. The authors compared the numerical results with experiments in a 26 mm ID and 900D long horizontal test section, presenting a good fit in predicting the average slug flow properties. They also concluded from both numerical and experimental results that the effect of the type of entrance on the slug flow properties reduces along the pipe, agreeing with Barnea and Taitel's (1993) statement.

2.3 Pressure propagation in multiphase flow

The pressure pulse propagation studies in two-phase flow started with Wallis (1969). He developed a one-dimensional model for single and two-phase flows from the continuity equations and considered the fluid density variation due to the pressure change. For the homogeneous case, Wallis (1969) presented the Eq. (2.20):

$$c_p = \frac{1}{\sqrt{[\alpha_U \rho_G + (1 - \alpha_U) \rho_L] \left(\frac{1 - \alpha_U}{\rho_L a_L^2} + \frac{\alpha_U}{\rho_G a_G^2} \right)}}, \quad (2.20)$$

where α_U is the unit cell void fraction and a is the acoustic velocity. Analyzing the equation above, Wallis (1969) concluded that the propagation velocity in a homogeneous two-phase flow is smaller than the acoustic velocity of each phase. In addition, he found that the propagation velocity achieves its minimum at 50% of the void fraction.

The lack of experimental data and models for two-phase flow motivated the work of Henry et al. (1971). The authors studied the pressure wave for different flow patterns presenting

the modeling and experimental data. For slug flow, they assumed an idealized form of this pattern: the gas and liquid phases enter alternately in the pipe and fill the entire cross-section, as shown in Fig. 2.3.

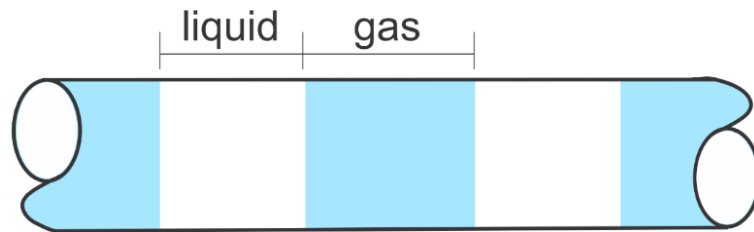


Figure 2.3. Idealized model of slug flow of Henry et al. (1971).

The model depends on the void fraction and each phase acoustic velocity, as shown in Eq. (2.21). The model indicates that the pressure wave velocity decreases when the void fraction increases. Their experimental data of air-water flow in a vertical test section of 50.8 mm ID and 38D long agreed with the model proposed. The authors concluded that the flow pattern influences the pressure wave velocity flow.

$$c_p = \left[\frac{\alpha}{a_G} + \frac{(1-\alpha)}{a_L} \right]^{-1}. \quad (2.21)$$

Miyazaki et al. (1971) studied the pressure propagation experimentally in a stagnant air-water mixture to focus on the drift study. The experiment was carried out in a 40 mm hydraulic diameter and 52D long vertical test section; they compared the results with a homogeneous, adiabatic, and no-slip model. The authors evaluated the pressure wave velocity with a single model and the void fractions spanning from 0 to 60%. The model diverges for higher void fractions. The authors agreed with Wallis (1969) that the pressure wave velocity in a two-phase flow is slower than in each phase due to the gas compressibility and the liquid inertia. In addition, they concluded that the two-phase system has a natural frequency featured by a coupled oscillation.

Later, Samuel Martin and Padmanabhan (1979) claimed that the model of Henry et al. (1971) did not consider the wave reflection caused when the pulse travels from one media to another. The authors used the homogenous and drift-flux models and compared the results with experimental air-water flow data. The experimental loop has a 26 mm ID and 723D total length.

It consists of vertical upward, horizontal, and downward parts that form an inverted U. They presented the Eq. (2.22) for the homogeneous case:

$$\frac{c_P}{a_G} = \frac{1}{\sqrt{\alpha_U (1 - \alpha_U) \frac{\rho_L}{\rho_G} + \alpha_U^2 + \left(\frac{a_G}{a_L}\right)^2 \left[(1 - \alpha_U)^2 + \alpha_U (1 - \alpha_U) \frac{\rho_G}{\rho_L} \right]}}. \quad (2.22)$$

The homogenous model shown in Eq. (2.22) underpredicts the pulse wave velocity. However, it presents a significant improvement when compared to the model of Henry et al. (1971). They concluded that the pressure wave velocity calculated by the drift-flux model is the same as the calculated by the homogenous model for slug flow. The authors suggested that a two-fluid model would be more suitable.

Unlike Henry et al. (1971), who linked the pressure velocity to the void fraction only, Matsui et al. (1979) suggested that the number of cells within the pipe also influences the pressure propagation. The authors assumed an idealized slug model and used an analogy to a mass-spring system with linear and non-linear approaches to obtain their model, as shown in Eq. (2.23).

$$c_P = \sqrt{\frac{\gamma P}{\rho_L \beta (1 - \beta)}}, \quad (2.23)$$

where γ is the polytropic constant, P is the bubble pressure, and β is the intermittence factor. The experimental test section is horizontal and has high- and low-pressure chambers totaling 618D and 5 mm ID. They fed water and air alternately to the pipe to reproduce the slug in its idealized form and compared the results with their model. The experimental results agreed qualitatively with the model; however, the quantitative results approached the experimental results for more than ten cells within the pipe. The natural frequency is symmetrical and with a minimum when the intermittence factor is 0.5. Consequently, the pressure wave velocity also is lowest with this intermittence factor. The authors also found that the pressure wave has a dispersive feature, i.e., its shape changes while the propagation occurs.

Nguyen et al. (1981) claimed that no models could predict the pressure pulse for all void fractions and flow patterns. Thus, the authors studied the pressure propagation velocity in stratified, slug, and bubbly flows, the last one using the homogenous flow model. For the slug

flow regime, they found the same equation proposed by Henry et al. (1971), as shown in Eq. (2.21).

Aiming to study the transient flow features caused by a quick-close valve, Akagawa et al. (1982) developed an oscillatory model based on a mass-spring system. They used a homogenous model such as a water hammer analysis. The authors suggest that the transient profile depends on the initial configuration adjacent to the valve when it closes. This configuration can be of two types: slug and gas. The first occurs when a liquid slug is adjacent to the valve; the last occurs when there is an elongated bubble. The authors compared the results with experimental data from a horizontal test section of 20.7 mm ID and 894D long. They claimed that the transient profile of the slug type has the characteristics of high-frequency oscillations and a fast amplitude decrease. The analogous mass-spring model gives good results compared to the experimental data when the adjacent configuration is gas-type. The authors concluded that the pressure profile depends on the initial configuration adjacent to the valve and can differ even for the same gas and liquid flow rates.

Caussade et al. (1989) studied the transient regime in slug flow with the drift-flux model. They compared the results with experimental data from a horizontal test section of 53 mm ID and 1,698D total length. The authors found out that the pressure wave propagates faster than the void fraction wave. In addition, they described the propagation mechanism of these two waves: when a disturbance reaches a particular pipe section, the pressure at this section changes abruptly; and remains approximately constant until the void fraction wave comes to the same area; moreover, when the void fraction wave reaches the pipe outlet, the pressure wave reaches its second steady-state. They also concluded that the void fraction wave is conservative, i.e., it maintains its shape while traveling along the pipe.

Vigneron et al. (1995) studied the transient features experimentally in slug and stratified patterns and compared the results with the predictions of three commercial software (TUFFP, PLAC, and OLGA). The horizontal test section has a 77.9 mm ID and is 5,392D long. Without drift, the void propagation velocity in slug flow is almost equal to the bubble translational velocity at the second steady state, either for an increase or decrease in the liquid flow rate. The experimental results showed that a change in the gas flow rate causes fast transients, while a change in the liquid flow rate causes slow transients.

Fabre et al. (1995) investigated the transient regime experimentally, focusing on the waves induced by a sudden change in the operational conditions. The experiments were conducted by Théron (1989) and Gadoin (1993). The experimental test section consists of a long horizontal pipe of 50 mm ID and 1,800D flowing air and water. Their principal findings

are: that the void wave is shape-conservative and propagates with the bubble's nose velocity; the pressure wave presented a dispersive shape as it traveled along the pipe. These pressure waves propagate due to the fluid density variation and can propagate upstream and downstream. In addition, they presented a void fraction and pressure wave model based on Fabre et al. (1989) generalized drift-flux model. This model can predict the void wave velocity with an acceptable agreement; however, it tends to underestimate the pressure wave velocity.

Huang et al. (2005) performed an experimental study of propagation velocity and attenuation coefficient for both bubbly and slug patterns. The authors observed that the pressure wave in the slug flow pattern has a more accentuated dispersive feature when compared with the bubbly flow. They concluded that the pressure propagation velocity for the slug flow pattern has no significant change for void fractions less than 50%. After that, the velocity increases with the void fraction. Furthermore, they found that the angular frequency increases the pressure wave velocity and attenuation coefficient.

Ambrose et al. (2016) studied the oscillation of the Taylor bubble rising in a stagnant liquid column. It is common sense that a pressure unbalance causes the oscillations; however, details about how these oscillations occur were not provided previously. They suggested that the oscillations are due to the difference between the Taylor bubble pressure and the hydrostatic pressure at the bubble's nose. The authors compared the numerical results with an analytical model and experimental data from Pringle et al. (2015) of a 290 mm ID and 34D long vertical test section. The numerical results were obtained using Computational Fluid Dynamics (CFD) techniques. They observed that the analytical and numerical solutions agreed with the experimental data only in the initial part of the pipe. As the bubble approaches the outlet, divergences with the experimental data appear. These divergences were expected for the analytical model. The model does not consider the behavior of the liquid ahead of the bubble; however, they did not expect this divergence in the CFD numerical simulation. They reported that the oscillation frequency depends on the average bubble length, and the amplitude depends on the fluid viscosities.

Using a lumped-mass approach, Ishikawa et al. (2014) developed a method to model the pressure wave in a two-phase steam-water flow. They claimed that no wave propagation model included the mass transfer between the phases; thus, they considered mass transfers caused by condensation and vaporization. Their model assumes that all cells have the same property; consequently, the analogous system has the same mass, spring constant, and damping factor. For the more straightforward case, without mass transfer and no damping considered, the propagation velocity is given by Eq. (2.24):

$$c_p = \sqrt{\frac{K_G}{\alpha_U [\rho_G \alpha_U + \rho_L (1 - \alpha_U)]}}, \quad (2.24)$$

where K_G is the Bulk modulus of the gas phase. The authors compared the numerical results with experimental data of an air conditioning system and found a good agreement between them.

Maria and Rosa (2016) experimentally investigated the propagation of pressure and void waves in an air-water slug flow. The horizontal test section has a 26 mm ID and is 1,009D long. The authors carried out four experimental runs. In the first two runs, the liquid velocity was constant at 0.6 m/s, and the transient was introduced due to a change in the gas's superficial velocity (halved in Test #1 and doubled in Test #2). In the last two runs, the gas velocity was fixed at 0.6 m/s, while the liquid velocity changed (halved in Test #3 and doubled in Test #4), causing the transient. They repeated the experiment 100 times for each run aiming to filter the natural intermittent behavior of the slug flow, especially for visualizing the void fraction wave. They presented the experimental pressure and void propagation velocity for each case. In addition, they concluded that the void wave is conservative and the pressure wave has a dispersive feature.

Gonçalves and Mazza (2022) used the slug tracking model to investigate the behavior of void and pressure waves. They also used an analogy between the mass-spring-damper system using the slug tracking model to estimate the time delay between the two steady-states. In this analogy, the gas compressibility represents the spring, while the liquid viscosity represents the damper. The authors used an approach based on Navarro's (2010) proposed method to couple the system by the liquid slug velocity as shown in Eq. (2.25):

$$b_1 \ddot{u}_s + b_2 \dot{u}_s + b_3 u_s = f(t), \quad (2.25)$$

where b_1 , b_2 , and b_3 are the terms analogous to the mass, spring constant, and damping factor, respectively. The authors determined these terms by algebraic manipulations in the slug tracking mathematical formulation. In addition, they compared the results with the experimental campaign of Maria and Rosa (2016), achieving less than a 10.0% deviation for predicting the pressure wave velocity.

2.4 Two-fluid models

Xu and Gong (2008) claimed that most models consider the void fraction as the only parameter influencing the propagation velocity. In addition, the results from those models also diverged between them. The authors were the first to use the two-fluid model to study the pressure wave propagation velocity. Their model considers no liquid drops in the gas phase and neglects the mass transfer between phases and the heat transfer with the surroundings. The authors used the virtual mass force to include phase moment transfer; they believed it significantly influences the pressure wave velocity in bubbly and slug flows. Thus, the authors divided the virtual mass force into weak and intensive, depending on the virtual mass coefficient, as shown in Eq. (2.26).

$$\begin{cases} c_{vm} \approx 0; & \text{weak (stratified)} \\ c_{vm} > 1; & \text{intensive (bubbly, slug)} \end{cases}, \quad (2.26)$$

where c_{vm} is the virtual mass coefficient. The authors presented the Eq. (2.27) to predict the pressure wave velocity:

$$c_P = \sqrt{\frac{\left[\frac{c_{vm}\rho_L}{\alpha_U(1-\alpha_U)^2} + \frac{\rho_G}{\alpha_U} + \frac{\rho_L}{(1-\alpha_U)} \right]}{\left[\frac{\rho_L}{(1-\alpha_U)a_G^2} + \frac{\rho_G}{\alpha_U a_L^2} \right] \left\{ 1 + c_{vm} \left[\frac{\alpha_U}{(1-\alpha_U)} + \frac{\rho_L}{\rho_G} \right] \right\}}}. \quad (2.27)$$

The authors highlighted a significant drop in the propagation velocity when the void fraction spans from 0 to 5% for all virtual mass coefficients. Moreover, they observed that the curves of pressure wave velocity for different void fractions remain practically the same for a virtual mass coefficient bigger than 1. The model agreed with the experimental data obtained by several authors. Although they used the two-fluid model, they did not mention the wave's oscillation frequency.

Li et al. (2012) used the two-fluid model to calculate the aerated drilling mud's wave propagation and attenuation coefficient. They assumed there was no heat transfer with the surroundings, no mass transfer between the phases, and the gas phase distributed evenly in the

liquid phase. They analyzed the influence of the void fraction, system pressure, and frequency on the attenuation coefficient and wave propagation velocity. They observed that the pressure wave velocity increases with the angular frequency until 100 rad/s (~16 Hz); the velocity achieves a limit above this value. In addition, they mention that the measurement while drilling (MWD) usually uses a pulse frequency in three ranges 0.02 to 0.2 rad/s, 0.5 to 4.0 rad/s, and 12 to 24 rad/s; however, they fixed a value of 50 rad/s when analyzing the influence of the void fraction and the system pressure. The authors also compared the results with experimental data of MWD and found a good agreement between them.

Unlike other models that disregarded the influence of oil well depth in the propagation velocity, Lin et al. (2013) used the two-fluid model to obtain the pressure wave velocity in annular pipes. Their model encompasses the virtual mass and drag forces, oil well depth, and temperature. The numerical results were compared with previous experimental data using an angular frequency fixed at 50 rad/s. The results were similar to Xu and Gong (2008): the propagation velocity suddenly decreases in the void fraction range from 0 to 5%, and the wave velocity versus void fraction curve presents a U shape behavior. Nonetheless, they affirmed that the pressure wave velocity achieves a constant value for angular frequencies bigger than 500 rad/s, unlike Li et al.'s (2012) statement.

Li et al. (2016) employed the perturbation theory and the two-fluid model to predict pressure wave propagation and attenuation in a two-phase slug flow. As in the model of Lin et al. (2013), the interfacial momentum interaction is due to the drag and virtual mass forces. Their one-dimensional model has four linear equations from each phase's mass and momentum conservation. The authors compared the predicted pressure wave velocity with experimental data from Henry et al. (1971) for a void fraction range from 0 to 0.25. They found that most points were in the $\pm 25\%$ deviation range, but others presented more considerable deviations. The authors also compared the attenuation factor with the experimental data from Huang et al. (2005). In addition, they evaluated the model's sensitivity to void fraction, system pressure, and temperature for wave velocity and attenuation coefficient using three angular frequency values: 10, 50, and 100 rad/s. As reported previously, the pressure propagation velocity versus void fraction curves has a U shape.

Li et al. (2022a) used the mathematical model of Li et al. (2016) to identify the flow-influencing parameters on the mud pulse, aiming to improve the mud pulse telemetry method. They analyzed the influence of the void fraction, operating frequency, and system pressure on the wave velocity and attenuation coefficient. For the model's sensitivity analysis with void fraction and pressure, they fixed the angular frequency at 50 rad/s. The curve shapes of void

fraction and system pressure agree with the results of Li et al. (2016). In addition, they presented that the wave velocity rapidly increases at lower frequencies until it achieves a constant value.

Li et al. (2022b) sought a model to predict the gas kick occurrence. Previous models neglected operational parameters and compared results with laboratory tests using air and water as working fluids. Like other two-fluid models, the authors used the interfacial momentum interaction as the sum of drag and virtual mass forces. However, the final equation is different from the models of Li et al. (2016) and Lin et al. (2013). The model's results were compared with experimental data from Henry et al. (1971) and Huang et al. (2005) for the 0 to 30% void fraction range, finding a good agreement between them.

2.5 Literature review gaps

Many works presented in the literature review have used the homogeneous or drift-flux models to study the pressure wave propagation velocity (AKAGAWA et al., 1982; CAUSSADE et al., 1989; FABRE et al., 1995; SAMUEL MARTIN; PADMANABHAN, 1979; WALLIS, 1969). However, the mixture models suppose that the gas phase is evenly distributed into the liquid, which does not occur in the slug flow. Therefore, these models do not capture the property change caused by the elongated bubble and the intermittent nature of the slug flow.

Another approach assumes that the liquid and gas phases fill the entire pipe cross-section. That is the idealized model of slug flow first proposed by Henry et al. (1971) and used later also by Matsui et al. (1979) and Nguyen et al. (1981). Nonetheless, the idealized model does not reproduce the real hydrodynamics of the slug flow. In addition, the final equation of Henry et al. (1971) and Nguyen et al. (1981) are the same and presented significant divergence with experimental data, as reported by Maria and Rosa (2016).

Ishikawa et al. (2014) employed a lumped-mass model to obtain the pressure wave velocity; however, they developed their model for a one-component two-phase bubbly flow, which has different hydrodynamics of the slug flow pattern.

The experimental approach is time-consuming, needs particular installation, and cannot be generalized. The Maria and Rosa (2016) experimental approach involved the test repetition 100 times for each point.

Furthermore, Gonçalves and Mazza (2022) used the slug tracking model and a mass-spring-damper analogy to estimate the pressure wave velocity. Despite the simulations

presenting a good agreement with the experimental data of Maria and Rosa (2016), the simulation of pressure and void waves using slug tracking is demanding. In addition, the slug tracking needs an initial condition, which they used the experimental data. However, when no experimental data is available, it is complex to provide this initial condition.

Xu and Gong (2008) were the first to study the pressure wave velocity using the two-fluid model. Nevertheless, they did not mention the wave's oscillation frequency. Another two-fluid model, as presented by Li et al. (2022a, 2012, 2016), Li et al. (2022b), and Lin et al. (2013), only needs constitutive relations for each pattern, thus simplifying the model. In addition, obtaining the attenuation coefficient of the pressure wave is simple. However, the two-fluid model needs the oscillation frequency as an input value. The authors neglected the analysis of this parameter, which presented a sensitivity analysis or used an arbitrary value. Therefore, determining this parameter is necessary due to the frequency's influence on this model. With the frequency parameter, it will be possible to estimate the pressure wave propagation relatively quickly.

Further, Appendix A presents a comparative table of the models presented in the literature review containing the methods adopted, the main results, the research gaps identified, and the simplified equation when is the case.

3 MATHEMATICAL MODEL

This chapter presents the two-fluid and the slug tracking models straightforwardly. The mathematical details for both models are in Appendix B and C.

3.1 Two-fluid model

This section presents the two-fluid modeling based on the models of Li et al. (2022a, 2012, 2016), Li et al. (2022b), and Lin et al. (2013). It is worth noticing that we corrected a few typographical issues in the previous models. The two-fluid model herein presented is based on the following assumptions:

- The flow is one-dimensional;
- The gas phase is compressible and treated as an ideal gas;
- The liquid phase is incompressible;
- There is no mass transfer between the phases;
- The model neglects the non-linear effects and high-order terms;
- The shear force in the gas-wall interface is neglected.

Equations (3.1) and (3.2) show the mass conservation equations for the gas and the liquid phases:

$$\frac{\partial}{\partial t}(\alpha_U \rho_G) + \frac{\partial}{\partial x}(\alpha_U \rho_G V_G) = 0, \quad (3.1)$$

$$\frac{\partial}{\partial t}[(1-\alpha_U)\rho_L] + \frac{\partial}{\partial x}[(1-\alpha_U)\rho_L V_L] = 0. \quad (3.2)$$

The first and second terms of Eqs. (3.1) and (3.2) represent the temporal mass change and mass flow rate, respectively.

Equations (3.3) and (3.4) show the momentum conservation equations for the gas and the liquid phases:

$$\frac{\partial}{\partial t}(\alpha_U \rho_G V_G) + \frac{\partial}{\partial x}(\alpha_U \rho_G V_G^2) + \alpha_U \frac{\partial P}{\partial x} = -F_{GL} - F_{WG} - \alpha_U \rho_G g \sin \theta, \quad (3.3)$$

$$\frac{\partial}{\partial t}[(1 - \alpha_U) \rho_L V_L] + \frac{\partial}{\partial x}[(1 - \alpha_U) \rho_L V_L^2] + (1 - \alpha_U) \frac{\partial P}{\partial x} = F_{GL} - F_{WL} - (1 - \alpha_U) \rho_L g \sin \theta, \quad (3.4)$$

where F_{GL} , F_{WG} , and F_{WL} are the forces in the gas-liquid, wall-gas, and wall-liquid interfaces, respectively. The last RHS term represents the force due to gravity. In the LHS of both equations, the first term represents the temporal momentum variation, the second represents the momentum rate along the axial distance, and the third represents the pressure force term.

Thus, we obtain a set of linear equations by rewriting the continuity and momentum equations, applying the perturbation theory, and using the following closure relations: force in the wall-liquid interface, Fanning friction factor, bubble radius, drag, and virtual mass forces, and drag and virtual mass coefficients. Writing the final equations as an inhomogeneous linear system, we obtain Eq. (3.5). The mathematical model details are in Appendix B.

$$\begin{bmatrix} M_{11} & M_{12} & M_{13} & 0 \\ M_{21} & M_{22} & 0 & M_{24} \\ M_{31} & M_{32} & M_{33} & M_{34} \\ M_{41} & M_{42} & M_{43} & M_{44} \end{bmatrix} \cdot \begin{Bmatrix} \alpha_U' \\ P' \\ J_G' \\ J_L' \end{Bmatrix} = \begin{bmatrix} 0 \\ 0 \\ \alpha_0 i \rho_{G0} g \sin \theta \\ -(1 - \alpha_0) i \rho_{L0} g \sin \theta \end{bmatrix}, \quad (3.5)$$

where the terms of the matrix in Eq. (3.5) are:

First line:

$$\begin{aligned} M_{11} &= \rho_G (\omega - \kappa V_{G0}), \\ M_{12} &= \frac{\alpha_{U0}}{a_G^2} (\omega - \kappa V_{G0}), \\ M_{13} &= -\alpha_{U0} \rho_G \kappa, \end{aligned} \quad (3.6)$$

Second line:

$$\begin{aligned}
 M_{21} &= -\rho_L (\omega - \kappa V_{L0}), \\
 M_{22} &= \frac{(1 - \alpha_{U0})}{a_L^2} (\omega - \kappa V_{L0}), \\
 M_{24} &= -(1 - \alpha_{U0}) \rho_L \kappa,
 \end{aligned} \tag{3.7}$$

Third line:

$$\begin{aligned}
 M_{31} &= \rho_G V_{G0} (\omega - \kappa V_{G0}) - i \rho_G g \sin \theta, \\
 M_{32} &= \frac{\alpha_{U0} V_{G0}}{a_G^2} (\omega - \kappa V_{G0}) - \alpha_{U0} \kappa, \\
 M_{33} &= \alpha_{U0} (\rho_G + c_{vm} \rho_L) (\omega - \kappa V_{G0}) - \rho_G V_{G0} \alpha_{U0} \kappa + \frac{3}{4} i \frac{c_{dg} \alpha_{U0} \rho_L V_{L0}}{R_b}, \\
 M_{34} &= -c_{vm} \alpha_{U0} \rho_L (\omega - V_{L0} \kappa) + \frac{3}{4} i \frac{c_{dg} \alpha_{U0} \rho_L V_{G0}}{R_b},
 \end{aligned} \tag{3.8}$$

Fourth line:

$$\begin{aligned}
 M_{41} &= \rho_L V_{L0} (\omega - \kappa V_{L0}) - i \rho_L g \sin \theta, \\
 M_{42} &= -\frac{V_{L0}}{a_L^2} (1 - \alpha_{U0}) (\omega - \kappa V_{L0}) + \kappa (1 - \alpha_{U0}), \\
 M_{43} &= c_{vm} \alpha_{U0} \rho_L (\omega - \kappa V_{G0}) + \frac{3}{4} i \frac{c_{dg} \alpha_{U0} \rho_L V_{L0}}{R_b}, \\
 M_{44} &= -\rho_L [(1 - \alpha_{U0}) + c_{vm} \alpha_{U0}] (\omega - \kappa V_{L0}) + \kappa (1 - \alpha_{U0}) V_{L0} \rho_L + \frac{3}{4} i \frac{c_{dg} \alpha_{U0} \rho_L V_{G0}}{R_b} + \\
 &\quad + \frac{4}{D} i C f_{wL} \rho_L V_{L0}
 \end{aligned} \tag{3.9}$$

The linear system reduces to a homogeneous system for the horizontal case since the RHS is a null matrix for $\theta = 0$. Therefore, for the system to admit a solution different from the trivial, the matrix determinant must be equal to zero, as shown in Eq. (3.10):

$$\begin{vmatrix} M_{11} & M_{12} & M_{13} & 0 \\ M_{21} & M_{22} & 0 & M_{24} \\ M_{31} & M_{32} & M_{33} & M_{34} \\ M_{41} & M_{42} & M_{43} & M_{44} \end{vmatrix} = 0. \quad (3.10)$$

Equation (3.10) gives a fourth-degree polynomial whose solution consists of four complex roots of the wave number. Two of these roots have high real values and yield small wave velocities. The other two roots have almost equal values except for their opposite signs, indicating that the pressure wave propagates upstream and downstream. Thus, we search for these opposite-signed roots using the Newton-Raphson method on Mathematica. Appendix D shows this implementation.

Finally, the angular frequency divided by the real part of the wave number gives the pressure wave velocity, as shown in Eq. (3.11).

$$c_p = \frac{I}{2} \left[\frac{\omega}{|Re(\kappa_1)|} + \frac{\omega}{|Re(\kappa_2)|} \right], \quad (3.11)$$

where κ_1 and κ_2 are the two opposite-signed roots. Similarly, the imaginary part of the wave number gives the attenuation coefficient, as shown in Eq. (3.12):

$$\eta = \frac{I}{2} \left[|Im(\kappa_1)| + |Im(\kappa_2)| \right]. \quad (3.12)$$

The two-fluid model needs the oscillation frequency as an input parameter. However, a method to determine this parameter is still lacking in the literature. We suggest using the slug tracking model to assess the slug flow oscillation frequency. The slug tracking model is briefly presented in the next section.

3.2 Slug tracking model

The slug tracking model used in this research follows the formulation of Rosa et al. (2015). Their model includes all terms considered in previous models plus the advective term. The model is capable of simulating horizontal and inclined flows. The following hypotheses compose the slug tracking model used in this research:

- The referential is inertial;
- The model is condensed in space and discrete in time;
- The flow is isothermal;
- The liquid phase is incompressible;
- The liquid film is non-aerated; therefore, all the gas present in this region is transported by the elongated gas bubble;
- The gas phase is treated as an ideal gas;
- The gas phase density is constant in a cell; however, it can vary in the other cells due to pressure changes;
- The gas pressure is constant in the elongated bubble.

Figure 3.1 shows the representation of the j^{th} cell, its structures, and the variables of interest. In Fig. 3.1, the coordinates x and y are parallel to the pipe axis and are measured from a stationary frame of reference. The flow parameters associated with the liquid slug are the slug length L_S and the liquid hold-up in the liquid slug R_S . Similarly, the flow properties of the elongated bubble are the liquid film length L_f , the liquid film R_f , the bubble pressure P , the gas velocity u_G , and the liquid film velocity u_f .

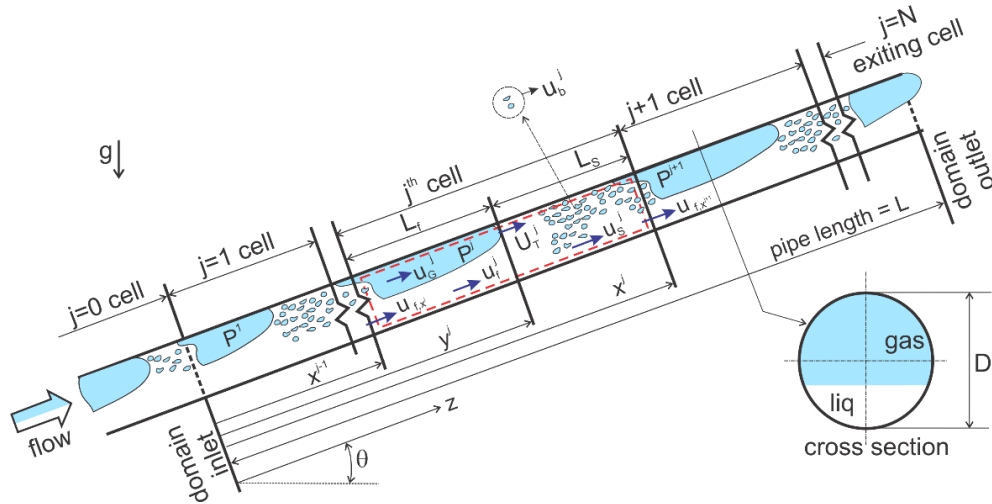


Figure 3.1. Properties and cell indexes in the slug tracking model - Rosa et al. (2015) adapted.

The equations that compose the slug tracking model are the mass and momentum balances. The mathematical details of the slug tracking model are in Appendix C. In addition, the system of equations in Rosa et al. (2015) is evaluated numerically using the Object Oriented Programming in FORTRAN and the fourth-order Runge-Kutta method. Modeling and programming details are in Rosa et al. (2015) and Rodrigues (2009). The simplified form of the mass balance applied to the j^{th} cell, as shown in Fig. 3.1, is reproduced below as Eq. (3.13).

$$\begin{aligned} \left[(1-R_f^j)L_f^j + (1-R_s^j)L_s^j \right] \frac{1}{P_G^j} \frac{dP_G^j}{dt} = & \frac{u_s^{j-1}R_s^{j-1}}{1-C_0^{j-1}(1-R_s^{j-1})} - \frac{u_s^jR_s^j}{1-C_0^j(1-R_s^j)} + \\ & + \frac{u_d^{j-1}(1-R_s^{j-1})}{1-C_0^{j-1}(1-R_s^{j-1})} - \frac{u_d^j(1-R_s^j)}{1-C_0^j(1-R_s^j)} \end{aligned} \quad (3.13)$$

In Eq. (3.13), the LHS term is the gas density temporal variation in the cell. The first two RHS terms represent the gas phase crossing neighboring cell boundaries; the two last are the drift terms. Equation (3.14) shows the simplified form of momentum balance applied to the j^{th} cell:

$$\begin{aligned} \frac{du_s^j}{dt} = & -(u_s^j)^2 \left\{ \frac{1}{L_s^j} \left(\frac{R_s^j}{R_f^{j+1}} - 1 \right) \left(1 - \frac{dx^j/dt}{u_s^j} \right)^2 \right\} + \frac{(P_G^j - P_G^{j+1})}{R_s^j L_s^j \rho_L} - g \sin \theta + \\ & -u_s^j \left[2Cf^j \frac{\rho_M^j}{\rho_L} \frac{|u_M^j|}{D} \frac{1}{R_s^j} \frac{R_s^j}{1-C_0^j(1-R_s^j)} + 2Cf^j \frac{\rho_M^j}{\rho_L} \frac{|u_M^j|}{DR_s^j} \frac{u_d^j}{u_s^j} \frac{(1-R_s^j)}{1-C_0^j(1-R_s^j)} \right] \end{aligned} \quad (3.14)$$

In Eq. (3.14), the LHS is the time derivative of the liquid slug velocity. In the RHS of this equation, the first term is the momentum exchange; the second is the pressure difference between consecutive cells; the third is the force due to gravity; and the last is the friction with the wall at the liquid slug.

The slug tracking model allows performing transient operations numerically and obtaining the evolution of the slug properties over time. Therefore, we can get a signal of the pressure and bubble nose velocity through time. We can transform this signal to the frequency domain using the Discrete Fourier Transform (DFT) to access the dominant frequencies.

4 SIMULATIONS AND FREQUENCY ANALYSIS

This chapter contains the simulation details and the frequency analysis methodology. Section 4.1 presents the experimental setup and the test grid from Maria and Rosa's (2016) study. In addition, Section 4.2 presents the random and periodic boundary conditions, the time window of the numerical simulations, the properties of the fluids, and the flow properties at the second steady state. Section 4.3 shows the Discrete Fourier Transform (DFT) and how we transform the signal from a time domain to a frequency domain. Finally, Section 4.4 shows the main correlations of the slug frequency of passage, which we will use to complete the two-fluid model.

4.1 Setup

The experimental data used as a base of comparison to the model presented is from the work of Maria and Rosa (2016). Their experimental campaign consists of a horizontal-oriented pipe of 26 mm ID and 1,009D long. Four stations along the test section count with pressure transducers and conductive probes. These stations are identified as S#1, S#2, S#3, and S#4, and their positions are at 153D, 307D, 551D, and 870D from the injector, respectively. Figure 4.1 shows the experimental test section as described.

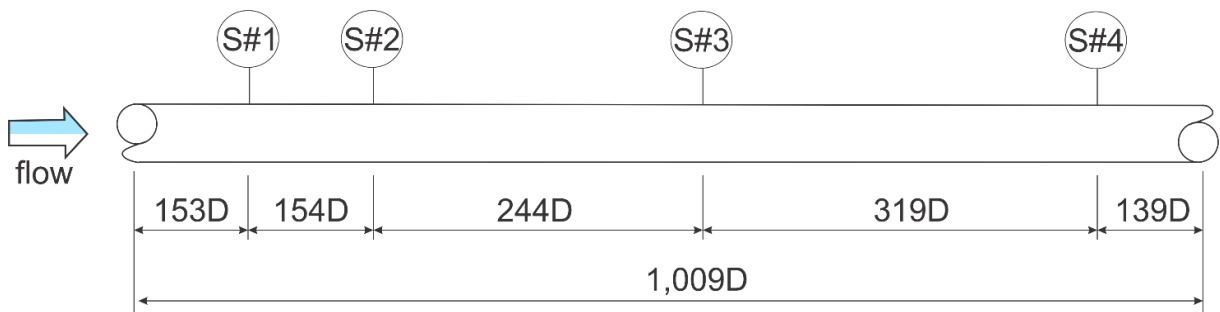


Figure 4.1. Experimental test section from Maria and Rosa (2016).

These researchers conducted four runs: for Tests #1 and #2, the liquid superficial velocity was fixed at 0.60 m/s, and the superficial gas velocity was halved in Test #1 and

doubled in Test #2; for Test #3 and #4, the superficial gas velocity was fixed at 0.60 m/s, and the liquid superficial velocity was halved in Test #3 and doubled in Test #4. Further details on the experimental setup and execution are in Maria and Rosa (2016). Table 4.1 shows the experimental test grid of Maria and Rosa (2016) in both initial and final states.

Table 4.1. Experimental test grid from Maria and Rosa (2016).

Test	First Steady State		Second Steady State	
	J_G [cm/s]	J_L [cm/s]	J_G [cm/s]	J_L [cm/s]
#1	54	60	27	60
#2	28	60	53	59
#3	54	60	57	30
#4	57	30	57	60

The experimental runs started with the first steady state. At 30 s, they imposed the transient for all cases, causing disturbances in the flow. These disturbances are the pressure and void waves that propagate along the pipe. The void wave propagates with much less velocity than the pressure wave. A new steady state will be achieved after an imposed transient. This new steady state, called Second Steady State, is achieved when this void wave reaches the outlet. The time it occurs changes for each case; however, all cases already achieved the second steady state at 60 s. The total data acquisition time is 100 s.

4.2 Boundary conditions

Aiming to numerically obtain the pressure wave propagation velocity, Gonçalves and Mazza (2022) used the slug tracking model to reproduce Maria and Rosa's (2016) experimental runs. They assumed two entrance conditions to reproduce the experimental campaign: random and periodic.

A periodic signal presents a repetition of its shape at constant time intervals. The periodic condition implies that all cells entering the test section have the same properties: liquid film and liquid slug lengths, unit cell void fraction, and superficial velocities of the phases.

These values are the average values measured experimentally. On the other hand, a random signal does not repeat itself at uniform intervals. Thus, the random condition consists of cells entering the test section with different properties. Both entrance conditions will be analyzed to assess the frequency influence beyond the passage frequency and to obtain the frequency features of each condition.

The time window is from 0 to 100 s, and the imposed transient occurred at 30 s for all cases following the data acquisition time from the experimental campaign of Maria and Rosa (2016). Furthermore, we will analyze the complete signal that includes the time when the transient occurs (0 to 100 s), the first steady-state (0 to 30 s), and the second steady-state (60 to 100 s). Figure 4.2 shows the complete, first, and second steady-state pressure signals for Test #1 at Station S#1 for both random and periodic conditions. In addition, Fig. 4.2 shows a zoom at the bottom right corner for the steady states in the periodic condition. This zoom shows a periodic oscillation of the signal, representing the entrance frequency of the cells in the domain, which is the passage frequency of the cells.

It is worth noticing that the average of the steady states in the random condition should be close to the presented ones in the periodic condition. However, that differs from what happens; this divergence could be due to the reduced time window that is not large enough to compose the average. In the periodic condition, the flow is developed artificially and represents an average of many cells passing through the stations.

To help the signal visualization, the pressure signal through time for all cases will be reproduced, but only for periodic conditions. Figures 4.3 to 4.6 show the pressure signal for Tests #1 to #4 at the four stations.

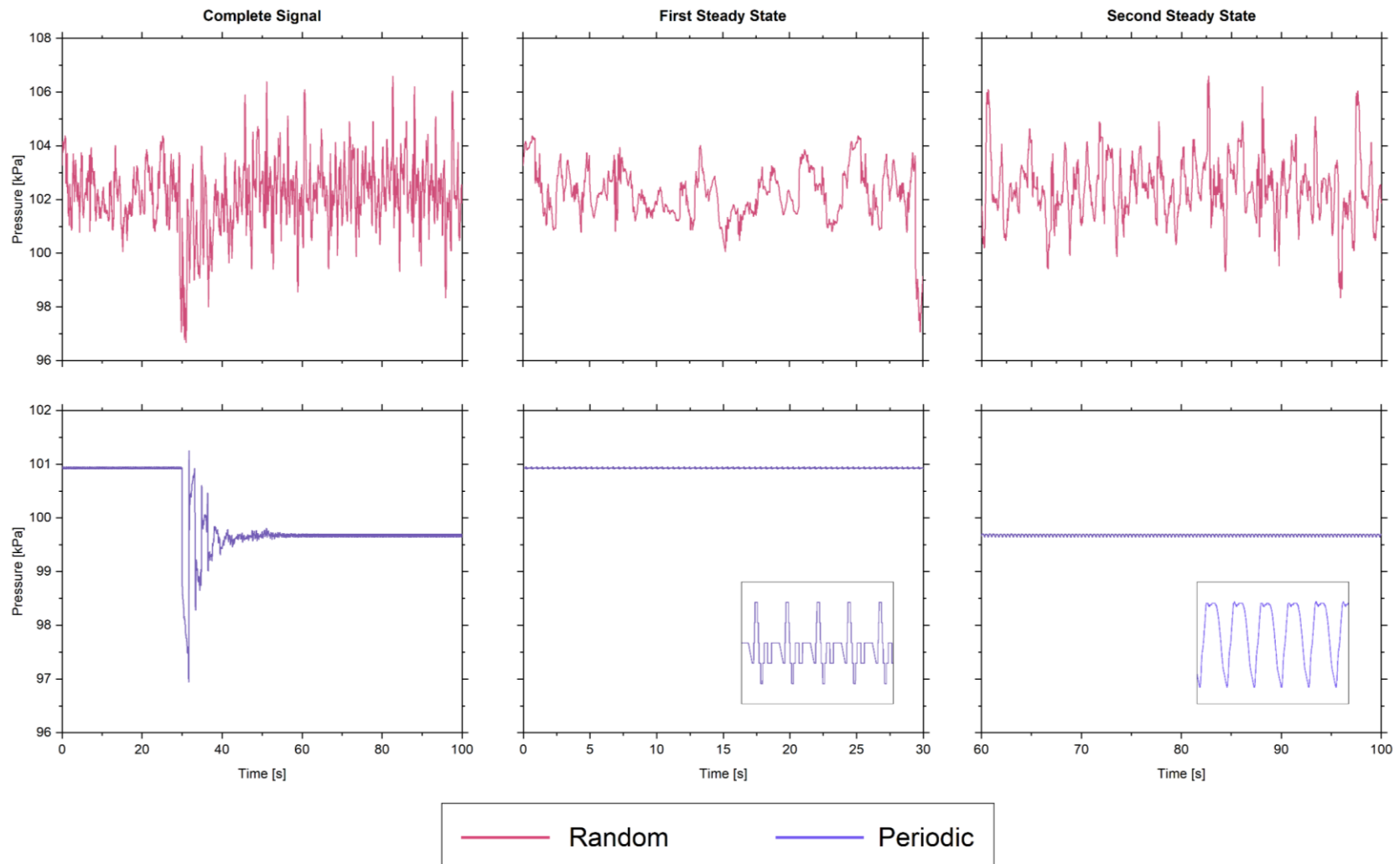


Figure 4.2. Pressure signals as a function of time for Test #1 at Station S#1: — random, and — periodic conditions. The last two graphs also show a zoom of the signal periodic oscillation.

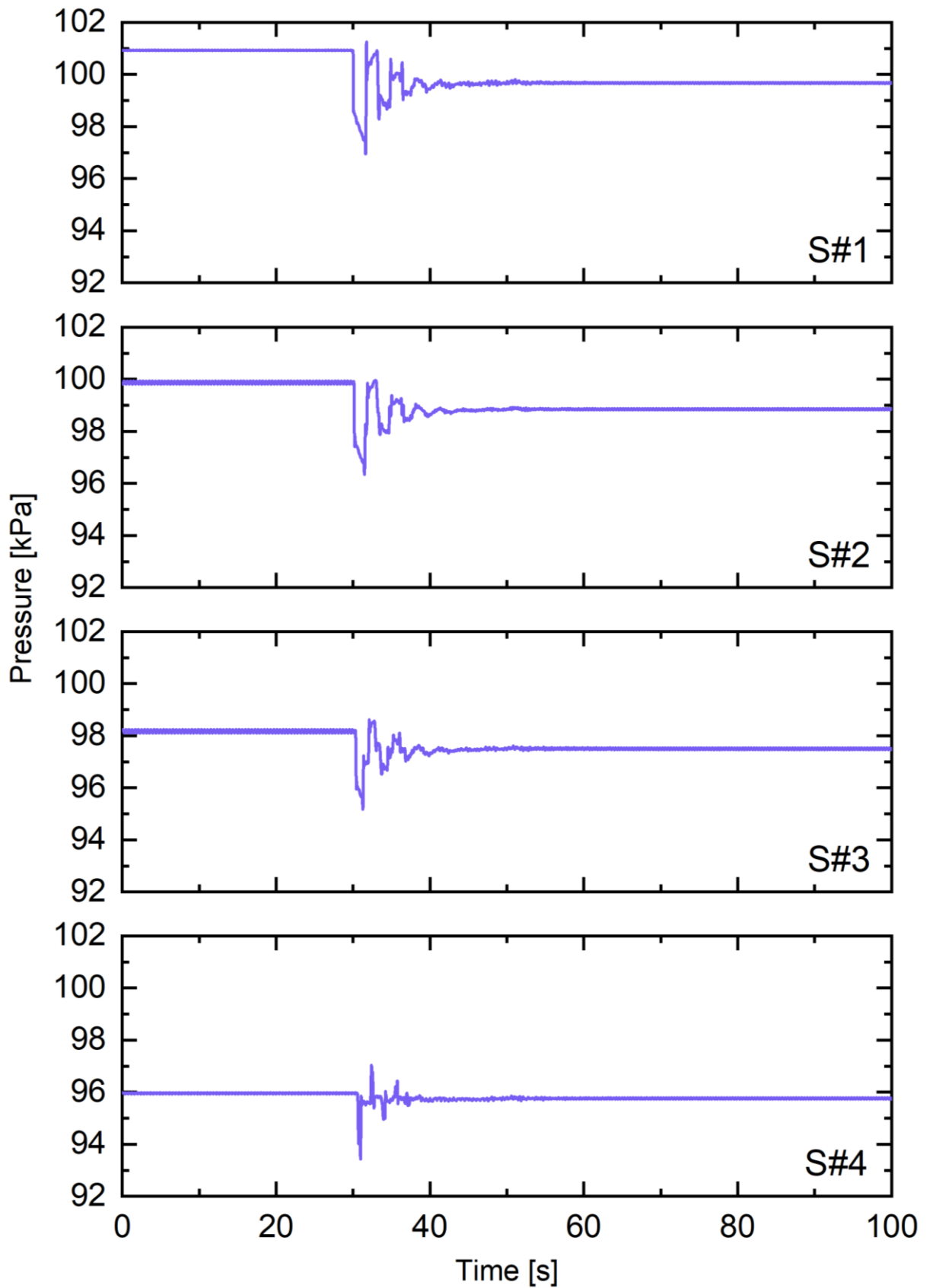


Figure 4.3. Pressure signals as a function of time for Test #1 from Gonçalves and Mazza (2022). From top to bottom Stations S#1, S#2, S#3, and S#4.

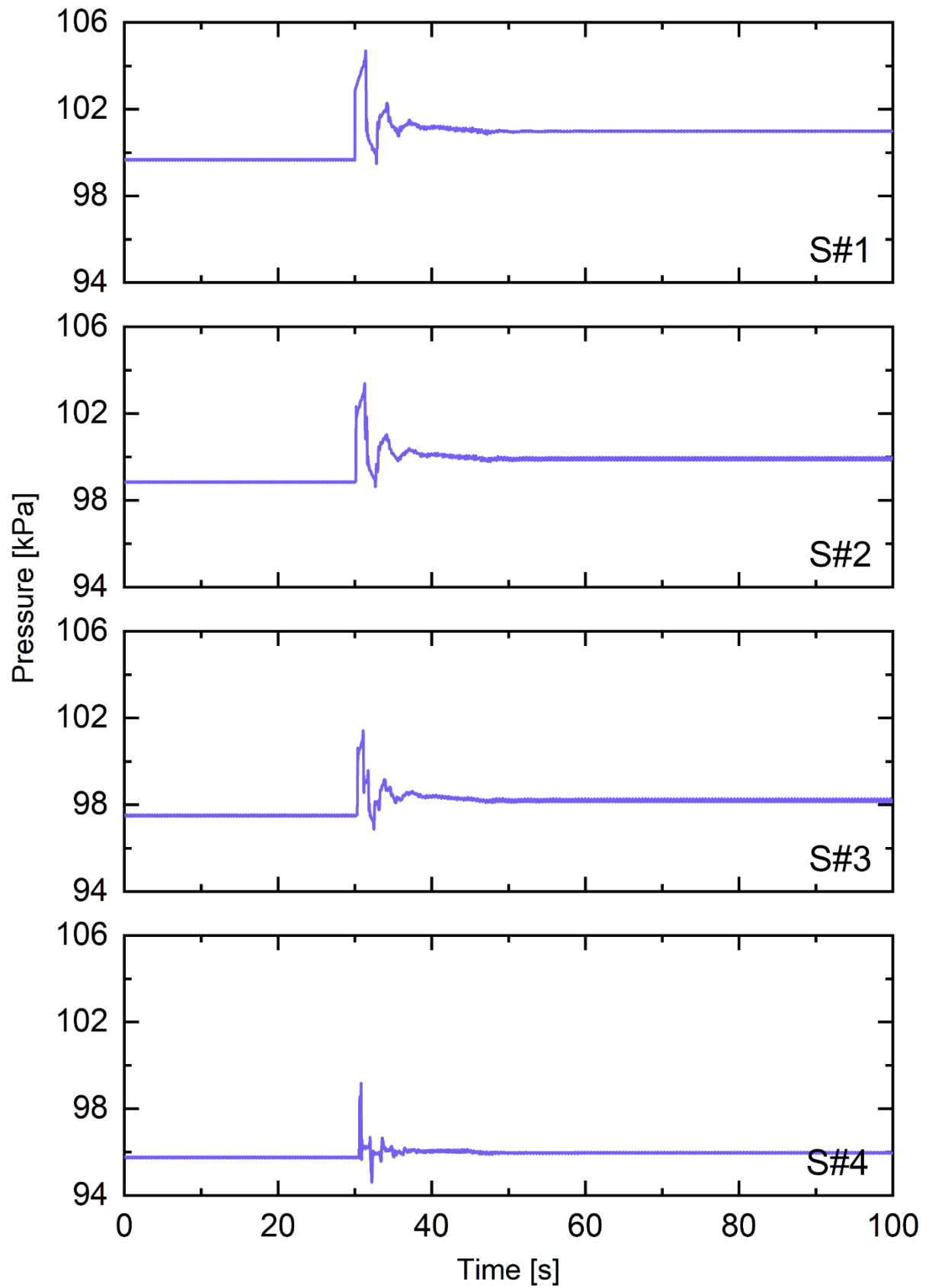


Figure 4.4. Pressure signals as a function of time for Test #2 from Gonçalves and Mazza (2022). From top to bottom Stations S#1, S#2, S#3, and S#4.

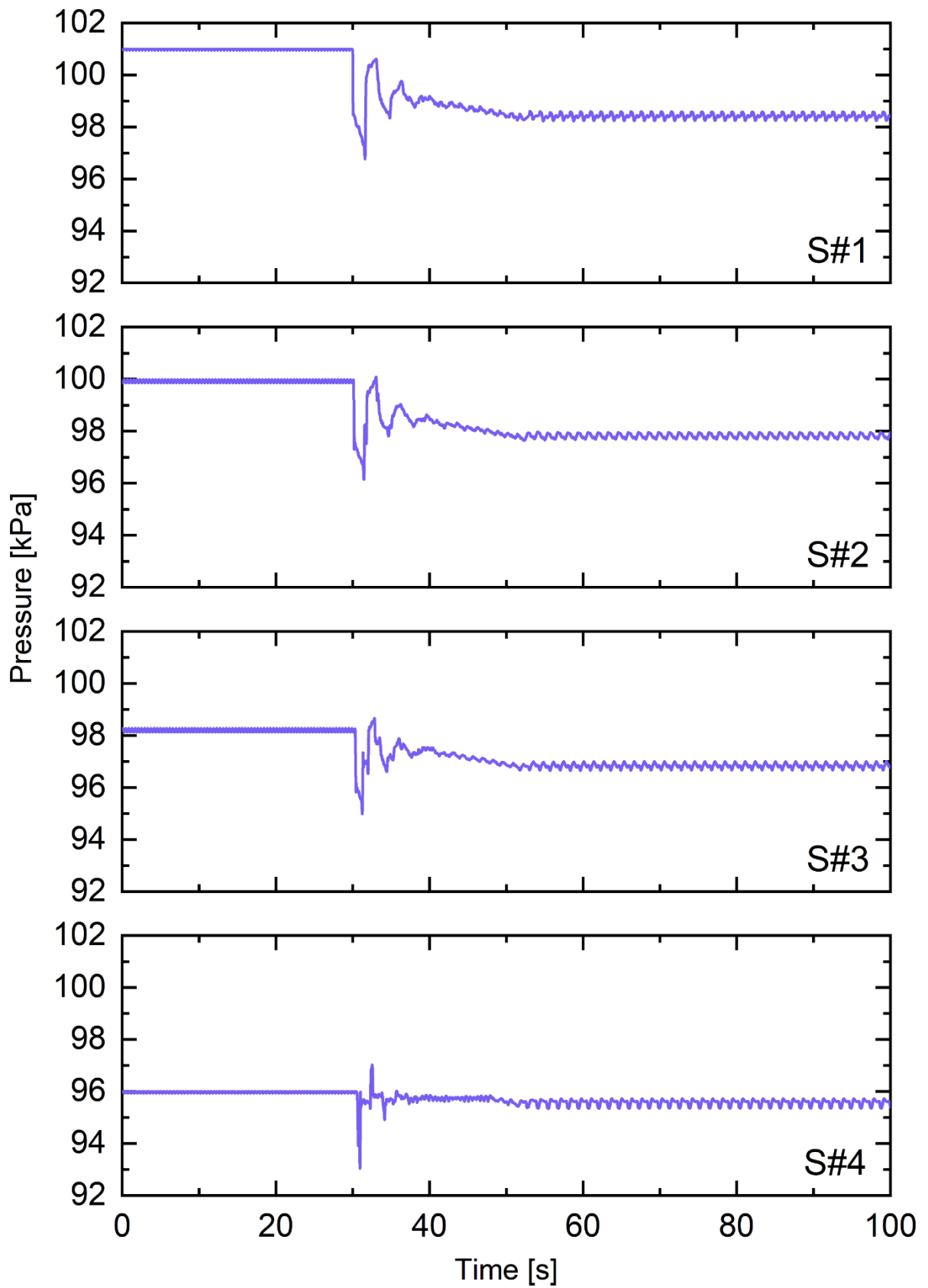


Figure 4.5. Pressure signals as a function of time for Test #3 from Gonçalves and Mazza (2022). From top to bottom Stations S#1, S#2, S#3, and S#4.

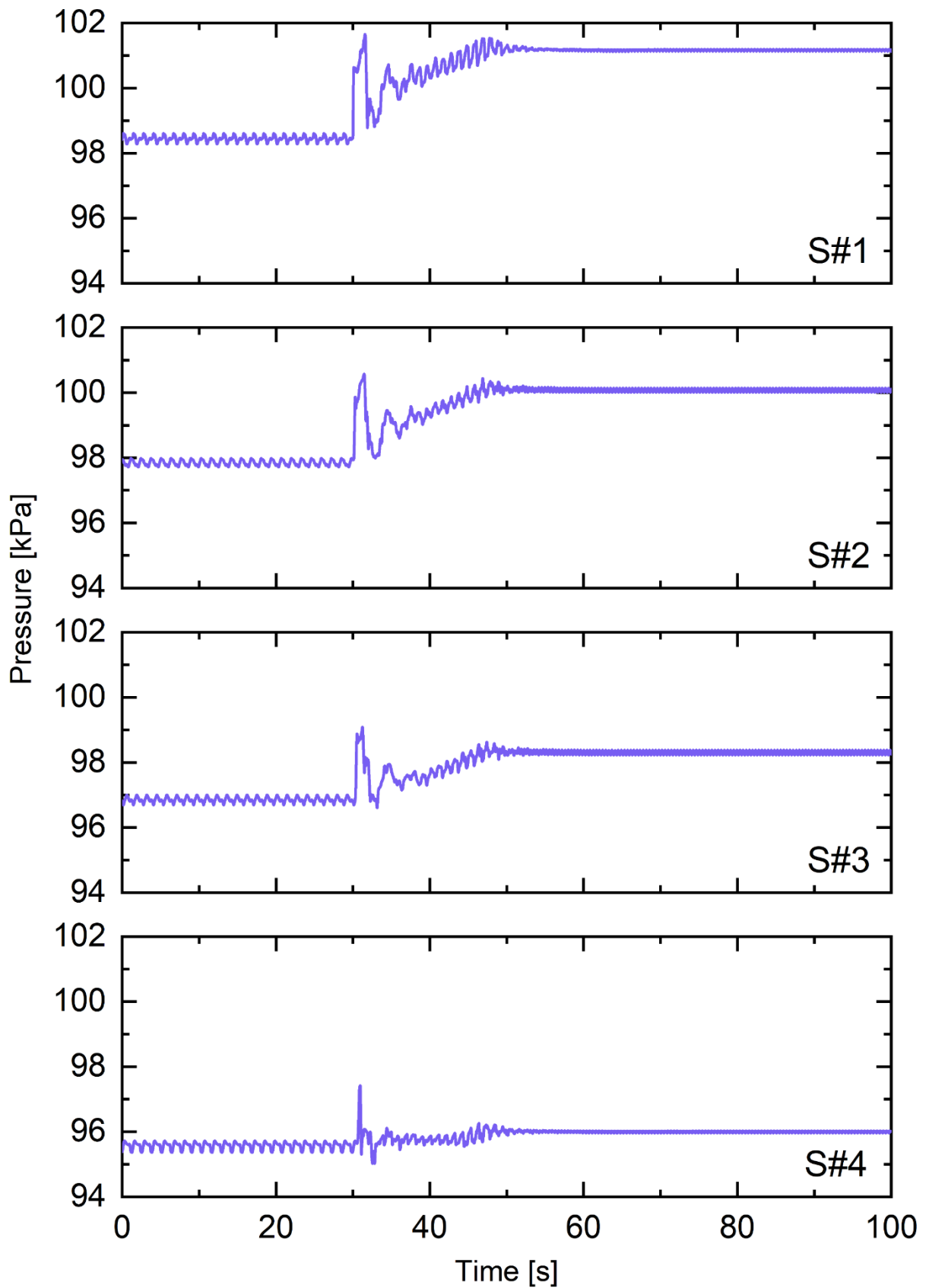


Figure 4.6. Pressure signals as a function of time for Test #4 from Gonçalves and Mazza (2022). From top to bottom Stations S#1, S#2, S#3, and S#4.

In Figs. 4.3 to 4.6, we can observe the change in the pressure signals as they travel along the pipe. This behavior demonstrates this wave's dispersive nature, as Fabre et al. (1995), Maria and Rosa (2016), and Matsui et al. (1979) pointed out previously. Another characteristic we can observe is the pressure decrease between stations because of the frictional pressure drop.

With the two-fluid model settled, we must simulate some input parameters: unit void fraction, gas and liquid superficial velocities, and the oscillation frequency. Maria and Rosa (2016) affirmed that the slug properties at the final state are more suitable for estimating the pressure wave propagation velocity. Therefore, we use the average properties simulated in slug tracking in the second steady state for the first three parameters. Table 4.2 shows each run and each station's slug flow properties at the second steady state.

Table 4.2. Flow properties at the second steady state for each run.

Test	S#	J_G [m/s]	J_L [m/s]	L_B/D [-]	L_S/D [-]	β [-]	α [-]	P_j [kPa]
#1	1	0.27	0.60	11.90	16.26	0.42	0.25	1.02E+02
	2	0.27	0.60	12.05	16.16	0.43	0.25	1.00E+02
	3	0.28	0.60	12.25	16.01	0.43	0.26	9.86E+01
	4	0.29	0.60	12.58	15.77	0.44	0.26	9.62E+01
#2	1	0.52	0.59	23.31	16.24	0.59	0.40	1.02E+02
	2	0.53	0.59	23.63	16.12	0.59	0.40	1.01E+02
	3	0.54	0.59	24.12	15.99	0.60	0.40	9.88E+01
	4	0.56	0.59	24.76	15.71	0.61	0.41	9.63E+01
#3	1	0.56	0.30	58.32	16.81	0.78	0.53	9.79E+01
	2	0.57	0.30	58.51	16.73	0.78	0.53	9.74E+01
	3	0.57	0.30	58.94	16.62	0.78	0.53	9.66E+01
	4	0.58	0.30	59.81	16.40	0.78	0.53	9.56E+01
#4	1	0.55	0.60	24.06	16.32	0.60	0.40	1.02E+02
	2	0.56	0.60	24.37	16.26	0.60	0.41	1.01E+02
	3	0.57	0.60	24.86	16.10	0.61	0.41	9.90E+01
	4	0.59	0.60	25.57	15.78	0.62	0.42	9.64E+01

Nonetheless, no information about the oscillation frequency is available. Thus, we will evaluate the frequency via the Discrete Fourier Transform presented in the next section.

In addition, we need some fluids properties for the slug tracking and two-fluid model simulations. Table 4.3 summarizes these properties: density, dynamic viscosity, the velocity of sound propagation, and superficial tension, respectively.

Table 4.3. Fluids properties.

Fluid	ρ [kg/m ³]	μ [Pa.s]	a [m/s]	σ [N/m]
Water	999	8.55 x 10 ⁻⁴	347.1	0.075
Air	1.18	1.70 x 10 ⁻⁵	1501	-

4.3 Discrete Fourier Transform (DFT)

The Fourier transform allows the analysis of a function in a domain different from the initial. The most common application is to transform a function from the time domain to the frequency domain. Equation (4.1) calculates the Fourier transform of a function analytically:

$$F(\omega) = \int_{-\infty}^{\infty} f(t) e^{-i\omega t} dt . \quad (4.1)$$

Besides the analytical transform, we can obtain the Fourier transform numerically. Therefore, we will use Matlab's Fast Fourier Transform (FFT) function to transform the signal to the frequency domain. The command "fft" calculates the Discrete Fourier Transform (DFT) using a fast Fourier transform algorithm.

To use this function, we need to determine the instant of time between each acquisition, as shown in Eq. (4.2):

$$dt = \frac{T}{N}, \quad (4.2)$$

where T is the time window, and N is the number of samples. In addition, Eqs. (4.3) and (4.4) gives the sampling frequency and the frequency differential:

$$F_s = \frac{1}{dt}, \quad (4.3)$$

$$dF_s = \frac{F_s}{N} . \quad (4.4)$$

Therefore, we can determine the frequency vector. The modulus of the “fft” command gives the function’s power in the frequency domain. Finally, we can plot the signal as a function of frequency for all cases. Appendix E contains the details of the Matlab implementation.

We used the Discrete Fourier Transform (DFT) to investigate the frequency spectrum. The oscillation frequency has not been extensively studied recently. The previous research using the two-fluid model to explore the pressure wave velocity used fixed frequency values higher than the slug’s oscillation frequency. Therefore, we will analyze the pressure and bubble nose velocity signals from the slug tracking simulations performed by Gonçalves and Mazza (2022) using the DFT to assess the oscillation frequency for slug flow.

4.4 Method flowchart

Figure 4.7 summarizes the steps needed to achieve our primary objective. The flowchart has three parts: in pink are the slug tracking simulations and signal analysis; in purple are the two-fluid model steps; in blue are the entrance conditions for both models.

The process begins by inputting the superficial velocities and void fraction in both models. Slug tracking numerical simulations obtain the pressure and elongated bubble’s nose velocity signal through time. The frequency spectrum for each signal is obtained using Discrete Fourier Transform (DFT). Analyzing these spectra, we obtain the frequency to use as an input parameter in the two-fluid model for each case.

The two-fluid model is solved using the frequency mentioned above, void fraction, and superficial velocities using the method of characteristics for gas and liquid phases mass and momentum conservation equations. This results in a fourth-degree polynomial equation. The real part of the roots gives the pressure wave velocity, and the imaginary part gives the attenuation factor. Finally, we compare the pressure wave velocity results with the experimental campaign of Maria and Rosa (2016).

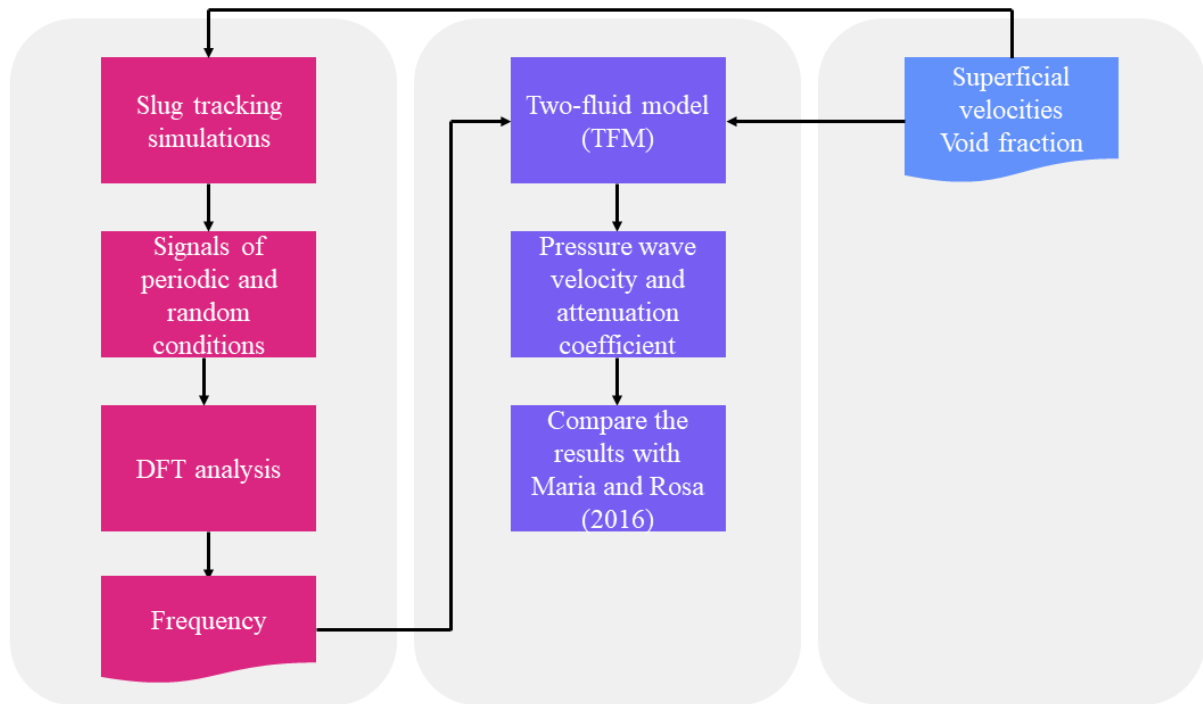


Figure 4.7. Method flowchart.

4.5 Frequency of passage correlations

Performing the slug tracking simulations and analyzing the frequency spectrum for each new case is time-consuming. Therefore, we aim to disclose the model to the frequency analysis for each case. We expect that the oscillation frequency is related to the slug's passage frequency.

Based on experimental data, many authors have suggested empirical correlations for the frequency of passage in slug flow. Gregory and Scott (1969) (G&Sc) proposed an empirical correlation based on their carbon dioxide and water experiments in a 19.05 mm ID horizontal pipe. Equation (4.5) shows this correlation:

$$\phi = 0.0226 \left[\frac{J_L}{gD} \left(\frac{19.75}{J} + J \right) \right]^{1.2}. \quad (4.5)$$

Greskovich and Shrier (1972) (G&Sh) suggested a modification in the formulation of Gregory and Scott (1969) to encompass the effect of using large pipes and the different fluids'

properties. They based the modification on their experiments with air-water and nitrogen-kerosene fluids using a 38.1 mm ID horizontal pipe. Equation (4.6) shows this correlation:

$$\phi = 0.0226 \left[\frac{J_L}{J} \left(\frac{2.02}{D} + \frac{J^2}{gD} \right) \right]^{1.2} . \quad (4.6)$$

Later, Heywood and Richardson (1979) (H&R) proposed a new correlation based on Gregory and Scott's (1969) procedure. They used their experimental data from an air-water horizontal system with 42 mm ID. The authors obtained a correlation similar to Greskovich and Shrier's (1972) correlation, as given in Eq. (4.7):

$$\phi = 0.0434 \left[\frac{J_L}{J} \left(\frac{2.02}{D} + \frac{J}{\sqrt{gD}} \right) \right]^{1.02} . \quad (4.7)$$

Nydal (1991) apud Schulkes (2011) (ND) suggested the Eq. (4.8) based on experimental data from a horizontal pipe flowing air and water; they analyzed different diameters in the range from 31 to 90 mm:

$$\phi = 0.088 \frac{(1.5 + J_L)^2}{gD} . \quad (4.8)$$

Manolis et al. (1995) (MN) proposed a new slug frequency correlation based on Gregory and Scott's (1969) correlation. Their experimental runs were in a horizontal setup with a 78 mm ID pipe flowing air and water. Equation (4.9) shows the final suggested correlation:

$$\phi = 0.0037 \left[\frac{J_L}{J} \frac{(25 + J^2)}{gD} \right]^{1.8} . \quad (4.9)$$

In addition, the Shell's slug frequency correlation is a well-accepted correlation for horizontal flows. This correlation was obtained by applying a curve fitting to Heywood and Richardson's (1979) data. Equation (4.10) gives this correlation:

$$\phi \sqrt{\frac{D}{g}} = 0.048 \left(\frac{J_L}{\sqrt{gD}} \right)^{0.81} + 0.73 \left(\frac{J_L}{\sqrt{gD}} \right)^{2.34} \left[\left(\frac{J_L}{\sqrt{gD}} + \frac{J_G}{\sqrt{gD}} \right)^{0.1} - 1.17 \left(\frac{J_L}{\sqrt{gD}} \right)^{0.064} \right]^2. \quad (4.10)$$

Zabaras (2000) (ZB) adapted the equation of Gregory and Scott (1969) to encompass the pipe's inclination effect. Their conclusion came out after analyzing a vast data set from many authors. The pipe's inclination ranged from 0 to 11 degrees from the horizontal, and the diameter ranged from 25.4 to 203.2 mm ID. In addition, the working fluids also differed. Equation (4.11) shows this correlation.

$$\phi = \left(0.836 + 2.75 \sin^{0.25} \theta \right) 0.0226 \left[\frac{J_L}{gD} \left(\frac{19.75}{J} + J \right) \right]^{1.2}. \quad (4.11)$$

Sakaguchi (2001) apud Rodrigues et al. (2007) (SK) proposed the Eq. (4.12) based on his experiments in vertical orientation:

$$\phi = \left[\frac{16,100 \left(\frac{D}{J} \right) \left(\frac{J_G}{J} \right)^{1.38} \left(\frac{J_L}{J} \right)^{-0.166} \left(\frac{J}{\sqrt{gD}} \right)^{-0.317} \left(\frac{\rho_L D J}{\mu_L} \right)^{1.61}}{\left(\frac{\rho_L D J^2}{\sigma} \right)^{-0.564} \left(\frac{\mu_G}{\mu_L} \right)^{0.333} \left(\frac{\rho_G}{\rho_L} \right)^{3.04} + 0.087} \right]^{-1}. \quad (4.12)$$

Lastly, Fossa et al. (2003) (Fossa) analyzed their experimental data from a horizontal test section flowing air and water. They performed the experimental runs in pipes of 40 and 60 mm ID. They suggested the following slug frequency correlation:

$$\phi = 0.044 \frac{J_G}{D} \frac{J_L}{J} \left[1 - 1.71 \frac{J_L}{J} + 0.7 \left(\frac{J_L}{J} \right)^2 \right]^{-1}. \quad (4.13)$$

We evaluated the pressure propagation velocity prediction using those nine correlations results as the input oscillation frequency in the two-fluid model.

5 RESULTS

This chapter contains the results of the pressure wave velocity prediction using the two-fluid model. Section 5.1 presents the model behavior for different frequency values to the four tests of Maria and Rosa's (2016) experimental study and a comparison with Li et al.'s (2022a) results. In addition, Section 5.2 show the results of the Discrete Fourier Transform for random and periodic boundary conditions and discusses the frequency to use in the two-fluid model. It also compares the frequency from DFT analysis with the predicted value by the nine slug frequency correlations shown in Section 4.5. Section 5.3 shows the pressure wave velocity predicted by the two-fluid model and the comparison with the experimental data from Maria and Rosa (2016).

Moreover, Section 5.4 presents a case study of the influence of the superficial velocity of the liquid phase on the two-fluid model. Section 5.5 compares the maximum value found by the two-fluid model and the previous models' predictions. Finally, Section 5.6 presents the attenuation coefficient prediction for the experimental tests.

5.1 Model behavior

The model presented in the articles of reference of this research has typographical errors that were corrected in Chapter 3. Therefore, we performed a parametric analysis for the four experimental runs varying the frequency from 0.5 to 30 Hz to obtain the fixed model behavior. Figure 5.1 shows this parametric analysis. The unit void fraction and superficial velocities are from the average properties of cells at the second steady-state from the slug tracking numerical simulations performed by Gonçalves and Mazza (2022). The model presented an asymptotic behavior for all cases. This trend agrees with the findings of Li et al. (2022a).

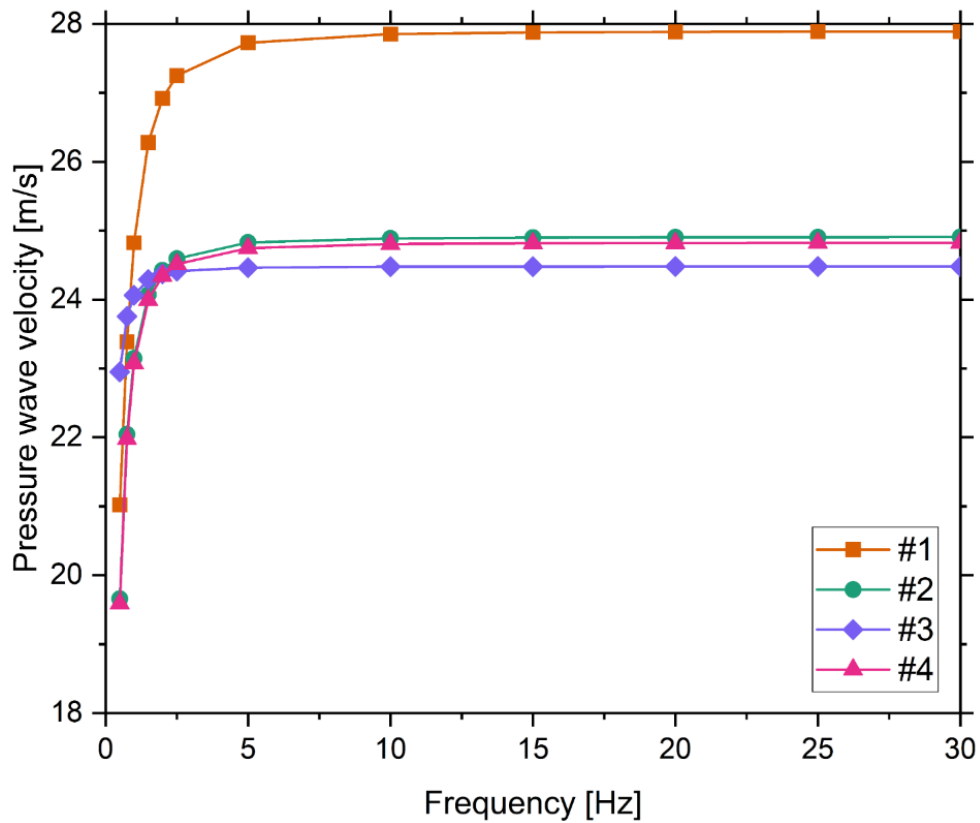


Figure 5.1. Pressure wave velocity as a function of frequency: —■— run #1, —●— run #2, —◆— run #3, —▲— run#4.

The superficial velocity of the liquid phase at the second steady state is 0.6 m/s, but Test #3. Especially this case (Test #3 - in purple) has a minor variation from minimum and maximum pressure wave velocity. Section 5.4 evaluated the influence of the liquid's superficial velocity on the pressure wave velocity with a case study.

Figure 5.2 compares the results of the model presented for Test #1 and the results presented by Li et al. (2022a). The maximum pressure wave velocity for each case normalized both curves. The curve for Test #1 presented a sharper increase in the wave velocity with the oscillation frequency than the results of Li et al. (2022a). However, no details about the superficial velocities of the phases or the unit cell void fraction were provided in the work of Li et al. (2022a). That is why we simulated a case with higher liquid and gas superficial velocities to verify its influence on the model. The liquid and gas superficial velocities are 2.10 m/s and 0.6 m/s, represented in purple in the figure. For this case, the model's curve approximates the curve presented by Li et al. (2022a), showing that the model presents coherent results.

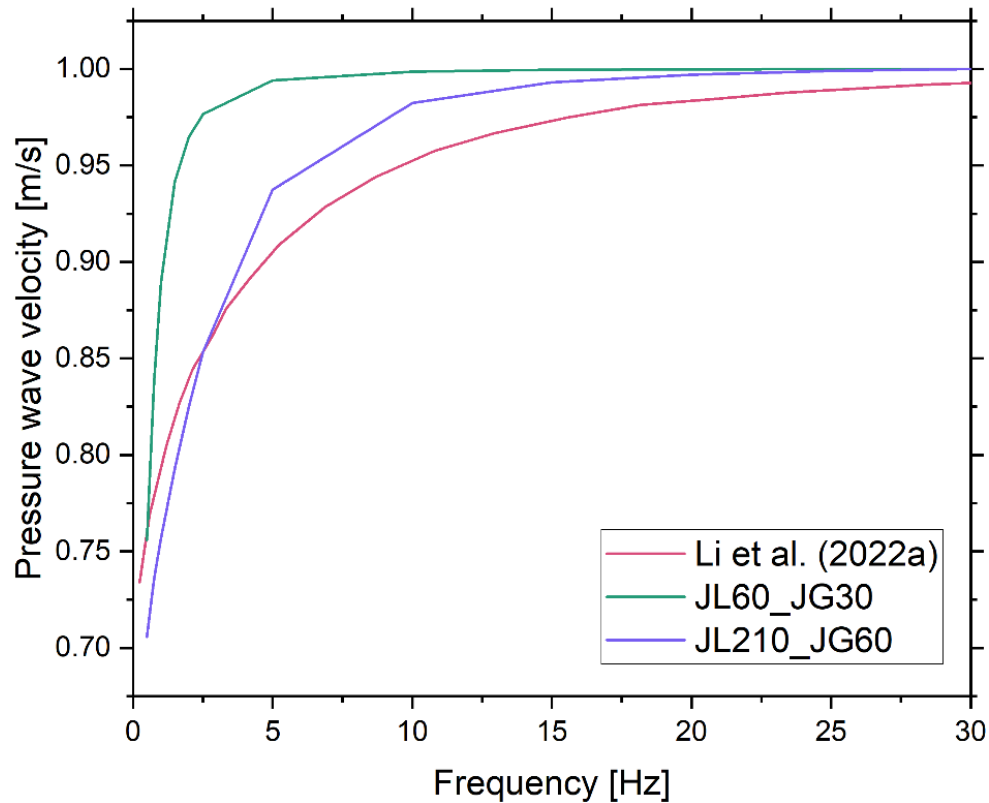


Figure 5.2. Normalized pressure wave velocity as a function of frequency: — Li et al. (2022a), — $J_L = 0.60$ m/s and $J_G = 0.30$ m/s, and — $J_L = 2.10$ m/s and $J_G = 0.60$ m/s.

5.2 Frequencies

Although many authors employed the two-fluid model to predict the pressure wave velocity, they did not investigate the frequency parameter that is an input in the model. Therefore, we transformed the pressure and bubble nose velocity signals to the frequency domain to comprehend the frequency characteristics. We analyzed the signal using the Discrete Fourier Transform (DFT) for both entrance conditions to get this. Figure 5.3 shows the signal power in the frequency domain for the complete signal (0 to 100 s) and first and second steady states for Test #1 at Station S#1.

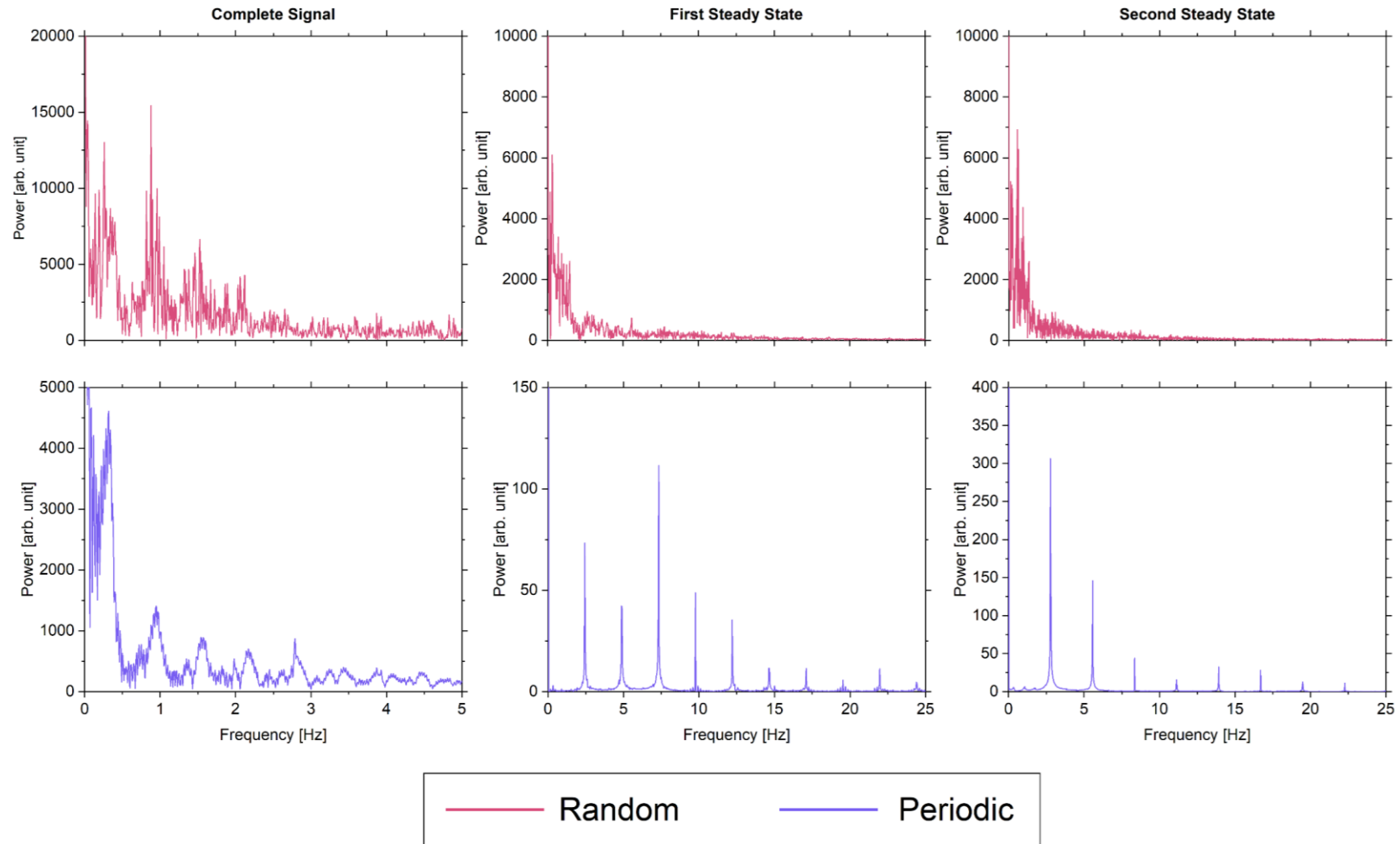


Figure 5.3. Signals power in the frequency spectrum of pressure signal for Test #1 at Station S#1: — random condition, and — periodic condition.

As shown in Fig. 5.3, the random conditions presented multiple dominant frequencies of high power for the complete signal, first and second steady states. This behavior can be due to the characteristic of the random entrance conditions. The Eq. (2.16) indicates that the frequency depends on the nose bubble velocity and the unit length. Therefore, multiple passage frequencies exist as cells of different properties enter the domain. This feature hinders identifying the dominant frequency due to oscillation.

On the contrary, we observed a more defined frequency spectrum in periodic conditions for the complete signal; even so, the changing of state (30 to 60 s) could be causing the multiple frequencies in this spectrum. However, the frequency spectrum for the first and second steady states presented a different feature. In these cases, we observed well-defined, equally spaced frequencies. This feature indicates the occurrence of harmonics, as shown in Fig. 5.4, for the pressure signal at the second steady state for Test #1 at Station #1.

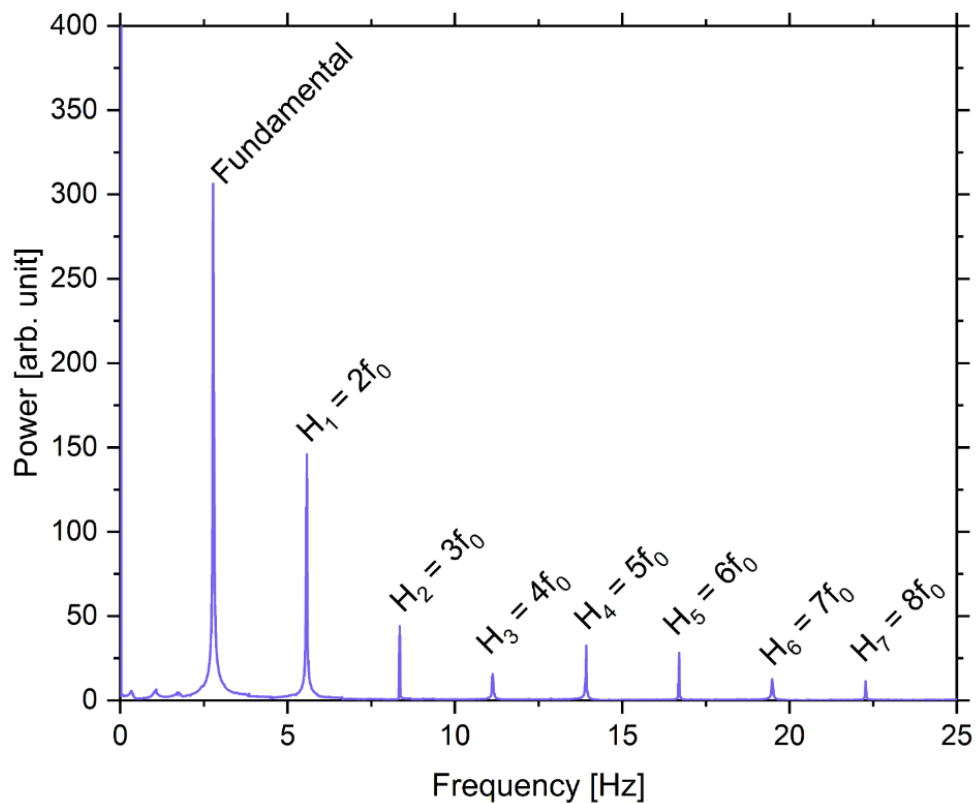


Figure 5.4. The fundamental frequency and harmonics of the pressure signal at the second steady state for Test #1 at Station S#1; f_0 is the fundamental frequency, and H indicates the harmonics.

In Fig. 5.4, the first frequency is the fundamental frequency (f_0), and the following frequencies are the harmonics. Equation (5.1) gives the harmonics for a given fundamental frequency:

$$H_n = (n+1)f_0, \quad n = 1, 2, 3, \dots \quad (5.1)$$

where the letter H indicates the harmonic.

However, the frequencies at the steady states' spectrum have lower power when compared to the complete signal in the periodic condition and all three cases of the random condition. That indicates the oscillation frequency could be hidden in the spectrum of the other cases. The second steady-state is the best alternative to obtain the pressure wave velocity using the periodic condition. The slug properties at the final state are more suitable for obtaining the pressure wave propagation velocity (Maria and Rosa, 2016).

Analyzing the frequency spectrum, we found that the frequency does not change along the pipe, having only a variance in power. Figure 5.5 shows the frequency spectrum of the pressure and bubble nose velocity signals for Test #1 for Stations S#1 to S#4. In the pressure signal case, the fundamental frequency is $f_0 = 2.775$ Hz.

In addition, by analyzing the elongated bubble's nose velocity signal through time, we also obtained a frequency spectrum in which fundamental and harmonic frequencies maintain their values. However, the power is much less than the frequency spectrum from the pressure signal. The power spectrum for the pressure signal is more than 10 times bigger than the nose velocity, as shown in Fig. 5.5. Therefore, the fundamental frequency from pressure signals and the elongated bubble's nose velocity at the second steady state are equal, needing to analyze only one of these signals.

Figure 5.6 shows the frequency spectrum of the pressure signal at the second steady state for Tests #2 to #4 for all stations. The fundamental frequencies are $f_0 = 2.425$ Hz, $f_0 = 0.775$ Hz, and $f_0 = 2.450$ Hz for Tests #2, #3, and #4. Test #3 has the lowest frequency of all tests. This behavior relates to the low liquid's superficial velocity at the second steady state.

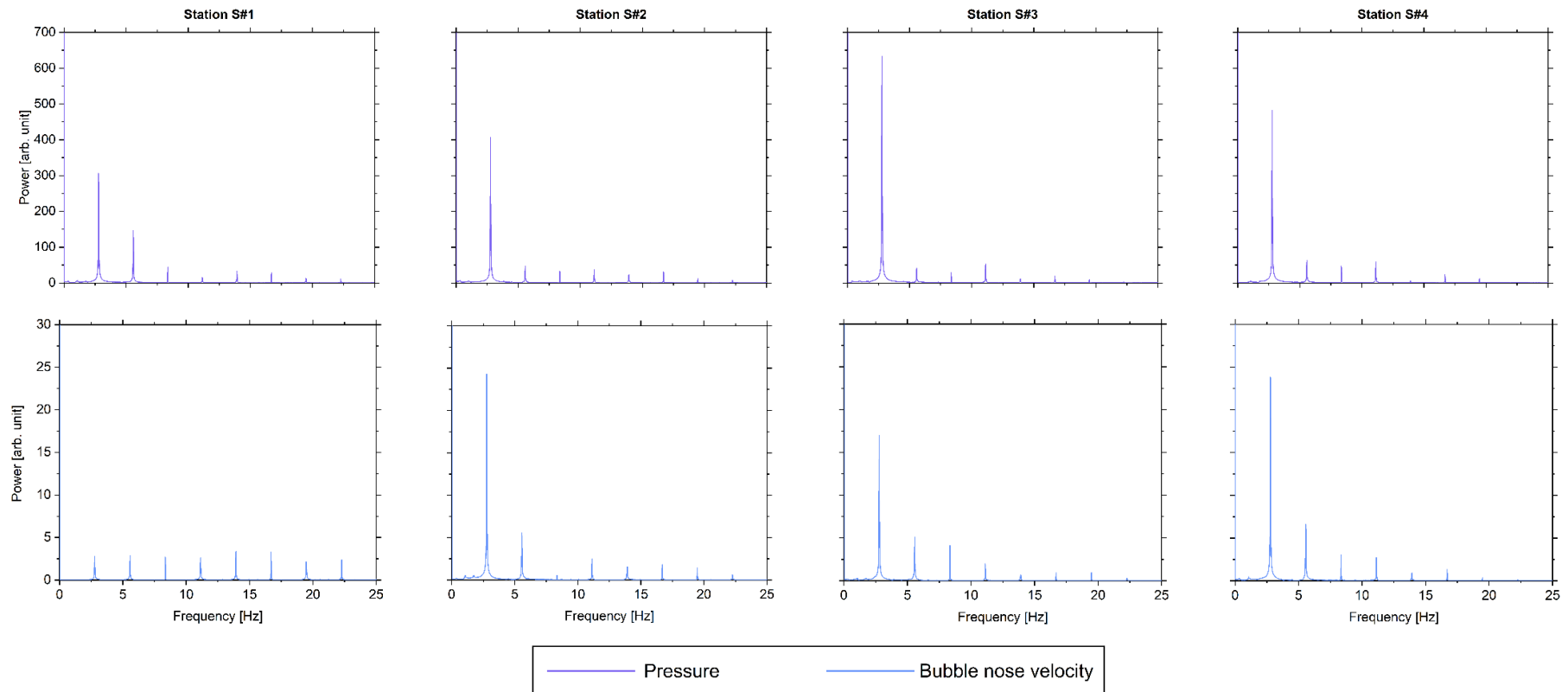


Figure 5.5. The frequency spectrum of the pressure signal at the second steady state for Test #1 for all stations: — pressure, and — bubble nose velocity signals.

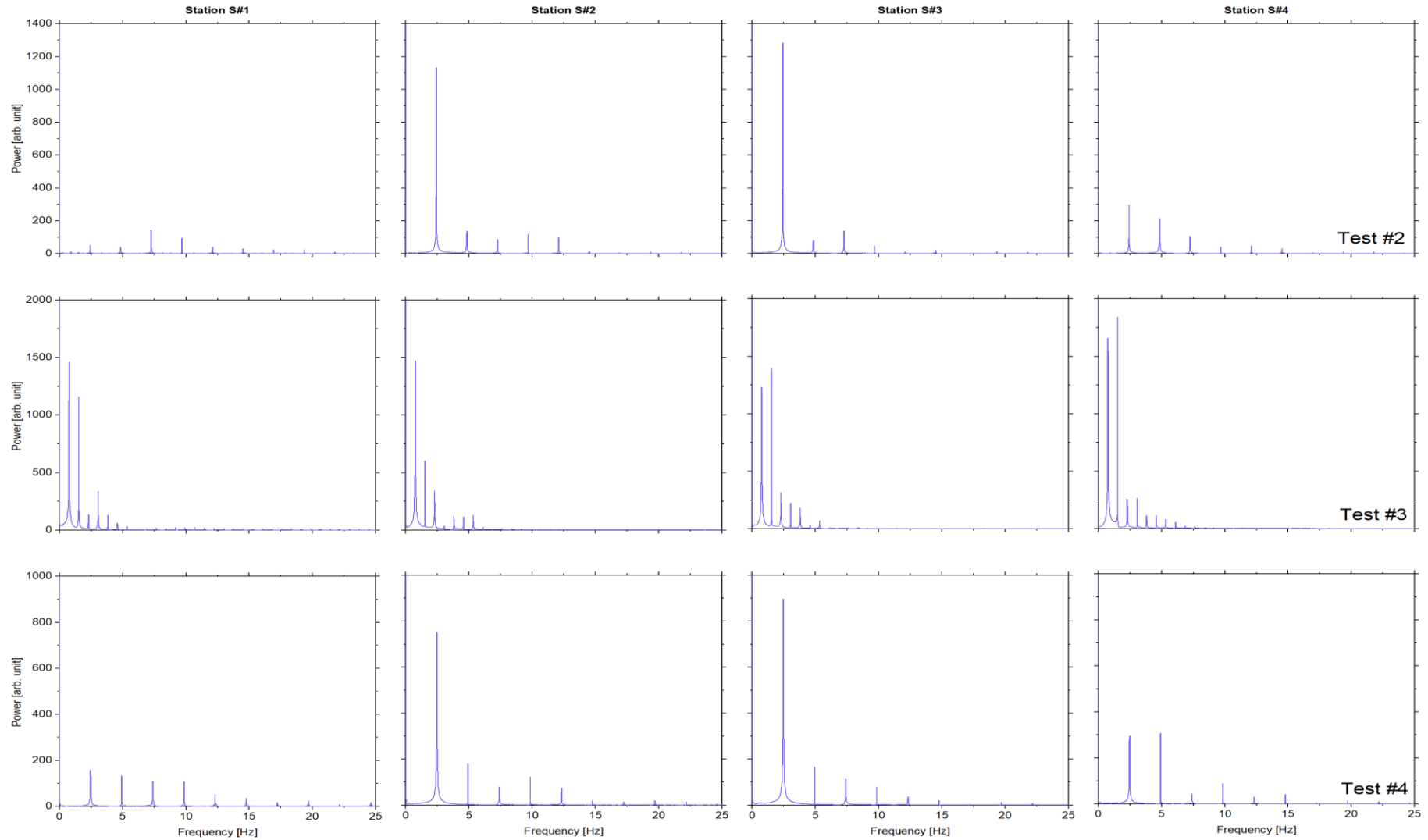


Figure 5.6. The frequency spectrum of the pressure signal at the second steady state for Tests #2 to #4 for all stations: from top to bottom #2, #3 and, #4.

Table 5.1 summarizes the fundamental frequencies for all cases and the ratio of the superficial velocities. Tests #2 and #4 show a ratio approximately equal to the unit; consequently, the fundamental frequency is almost the same. In Test #1, where the ratio is near two, we have smaller elongated bubbles; this led to a smaller compressibility of the gas phase. Finally, Test #3 has the more significant gas phase compressibility due to the bigger elongated bubbles.

Table 5.1. Fundamental frequency for the four tests and the ratio of the superficial velocities at the second steady state.

Test	J_L/J_G	Fundamental frequency [Hz] - f_0
#1	≈ 2	2.775
#2	≈ 1	2.425
#3	≈ 0.5	0.775
#4	≈ 1	2.450

The cell's stiffness is related to the ratio of the superficial velocities. It increases with the amount of liquid within the pipe. The equation (5.2) gives the oscillation frequency in a mass-spring-damper system. From this equation, we expected an increase in the frequency when increasing the stiffness. That is what happens. From Tab. 5.1, we observed that increasing the ratio increases the oscillation frequency. In addition, it is worth noting that the frequency remained almost constant when the ratio was doubled. On the contrary, the frequency significantly decreased when the ratio was halved.

$$f = \frac{1}{2\pi} \sqrt{\frac{k}{m}}, \quad (5.2)$$

where k is the spring stiffness, and m is the mass of a mass-spring-damper system.

Finding the oscillation frequency is challenging when using the two-fluid model to predict the pressure wave velocity. Using the slug tracking simulations to obtain the pressure signal through time and the Discrete Fourier Transform is a way to obtain this frequency; however, it is time-consuming. Analyzing the frequency values for each case in Tab. 5.1, we have observed that this frequency is comparable to the frequency of passage of the slug

structures. Thus, the oscillation frequency is related to the frequency of passage and can be estimated using correlations available in the literature.

Table 5.2 shows the frequency of passage predicted by nine correlations – Eqs. (4.5) to (4.13) – and the normalized RMS error compared to the DFT analysis results.

Table 5.2. The average frequency of passage prediction and its normalized RMS deviation.

Correlation	#1		#2		#3		#4	
	$\bar{\phi}$ [Hz]	NRMS [%]						
G&Sc (1969)	2.77	1.10	2.07	14.74	1.22	56.92	2.03	17.03
G&Sh (1972)	2.78	1.14	2.08	14.42	1.22	57.52	2.04	16.72
H&R (1979)	2.60	6.49	2.02	16.56	1.29	66.27	1.99	18.60
ND (1991)	1.52	45.17	1.51	37.85	1.12	44.24	1.52	37.90
MN (1995)	7.58	173.14	4.84	99.69	2.20	184.03	4.71	92.37
Shell	1.41	49.18	1.25	48.30	0.64	18.01	1.27	48.35
ZB (2000)	2.32	16.49	1.73	28.70	1.02	31.20	1.70	30.62
SK (2001)	9.62	246.59	8.90	266.87	7.17	825.49	8.89	263.03
Fossa (2003)	2.03	26.73	1.60	33.89	0.67	13.09	1.61	34.22

Note: G&Sc is the correlation of Gregory and Scott (1969), G&Sh indicates Greskovich and Shrier (1972), H&R is the Heywood & Richardson (1979) correlation, ND is Nydal (1991), MN is Manolis et al. (1995), ZB is from Zabarar (2000), SK is the correlation of Sakaguchi (2001), and last, the correlation Fossa et al. (2003) is Fossa.

The correlations from Manolis et al. (1995) and Sakaguchi (2001) predicted frequencies that presented the largest RMS deviation of all correlations in the four tests. Both correlations were developed for different applications than ours; the first for larger diameter pipes and the second for vertical flow. Therefore, we discarded these correlations from the pressure wave velocity prediction.

The Gregory and Scott (1969), Greskovich and Shrier (1972), and Heywood & Richardson (1979) correlations presented a good fit for Test #1 and a significant deviation for Test #3 (> 50%). The other correlations presented less than a 50% deviation for all tests. The correlations from Shell and Fossa et al. (2003) predicted the frequency in Test #3 more accurately, while the others overestimated it. Figure 5.7 compares the frequency via DFT and the predicted values by the nine correlations suggested in Chapter 4.

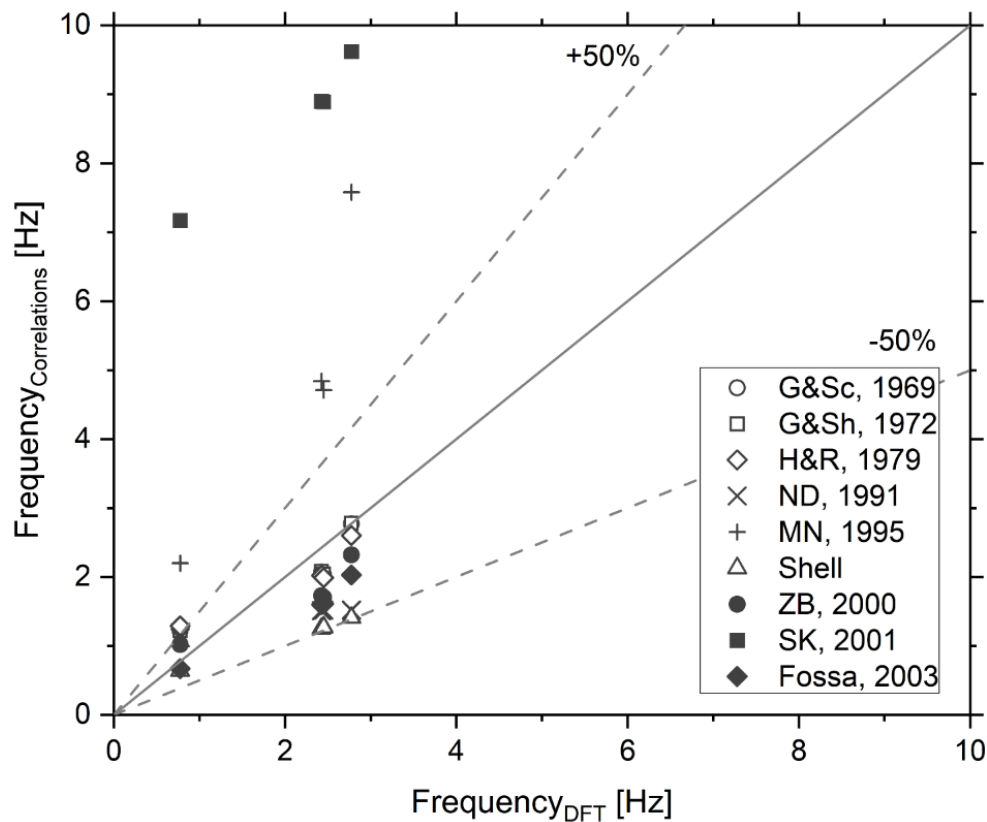


Figure 5.7. Comparison between the frequency predicted by the correlations and the frequency found via DFT.

5.3 Pressure wave propagation

After finding each case's frequency, we need to calculate the pressure wave velocity numerically. To do this, we used the two-fluid model. The determinant of Eq. (3.10) leads to a fourth-degree polynomial equation in which the roots are the wave numbers. We obtained the roots of this polynomial equation using the Newton-Raphson method. Thus, we obtain the numerical pressure wave velocity by Eq. (3.11) using the slug properties at the second steady

state. Table 5.3 shows the experimental and numerical pressure wave velocity and the deviation between these values. The lowest deviation occurs in Test #2 with 4.01%, and the most significant deviation occurs in Test #3 with 28.64%.

In addition, the frequency is directly related to the pressure wave velocity; higher oscillation frequencies result in higher pressure propagation velocity. Thus, we expected the highest propagation velocity in Test #1 and the lower propagation velocity in Test #3 due to the given frequencies for each case. That agrees with the numerical prediction shown in Tab. 5.3.

Table 5.3. Numerical and experimental pressure wave velocity and the deviation between them.

Test	Experimental c_p [m/s] Maria and Rosa (2016)*	Numerical c_p [m/s]	Deviation [%]
#1	23.0 ±1.3	27.365	18.98
#2	25.6 ±1.4	24.575	4.01
#3	18.5 ±1.0	23.799	28.64
#4	21.0 ±1.1	24.501	16.67

Note: *Maria and Rosa (2016) found a relative uncertainty of 5.5% of the average. This corresponds to a confidence interval of 95% using the Student's t-distribution.

The average deviation of all cases is 17.07%. Nonetheless, the deviation is less than 30% for all cases, as shown in Fig. 5.8. Although it appears to be a significant deviation, Li et al. (2016) found a similar deviation in predicting the pressure wave velocity using the two-fluid model with the maximum deviation is near 50%.

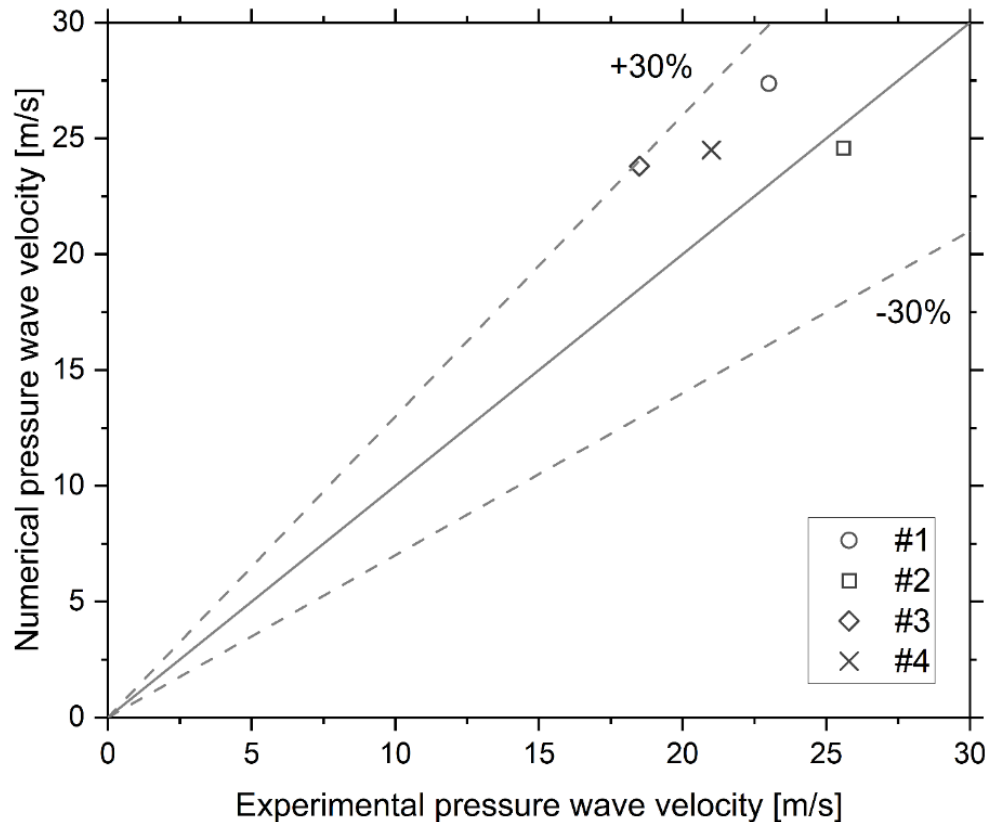


Figure 5.8. Comparison between the experimental data with the numerical prediction of the pressure wave velocity.

The deviation can result from simplifications and using correlations as the force in the wall-liquid interface, Fanning friction factor, bubble radius, drag and virtual mass forces, and drag and virtual mass coefficients.

Additionally, the most significant deviation occurs for Test #3. In this case, the ratio of superficial velocities is approximately 0.5, the smallest of the four cases. Therefore, we evaluated the influence of the liquid superficial velocity in the next section.

The comparison in Fig. 5.8 depends on the slug tracking simulations and signal analysis to obtain the frequency. Thus, we must remove this dependency to simplify the pressure wave velocity prediction. In this way, we compared the experimental pressure wave velocity and the predicted using the frequency correlations presented in Chapter 4: Fossa et al. (2003), Gregory and Scott (1969), Greskovich and Shrier (1972), Heywood and Richardson (1979), Nydal (1991), Shell, and Zabarar (2000). We did not test the correlations of Manolis et al. (1995) and Sakaguchi (2001) due to the most significant deviation between the predicted frequency and the results from the signal analysis. Table 5.4 shows the pressure wave velocity prediction by the two-fluid model using the frequency correlations and their relative deviation from the experimental data.

Table 5.4. Predicted pressure wave velocity, the relative deviation with the experimental data from Maria and Rosa (2016), and the average relative deviation for each correlation.

Correlation	#1		#2		#3		#4		$\bar{\sigma}$ [%]
	c_p [m/s]	σ [%]	c_p [m/s]	σ [%]	c_p [m/s]	σ [%]	c_p [m/s]	σ [%]	
G&Sc (1969)	27.36	18.97	24.45	4.48	24.19	30.78	24.36	16.00	17.56
G&Sh (1972)	27.37	18.99	24.46	4.46	24.20	30.79	24.36	16.02	17.57
H&R (1979)	27.29	18.67	24.43	4.55	24.23	30.95	24.34	15.92	17.52
ND (1991)	26.32	14.41	24.08	5.95	24.14	30.51	24.01	14.36	16.31
Shell	26.10	13.48	23.74	7.28	23.49	26.98	23.68	12.77	15.13
ZB (2000)	27.15	18.05	24.27	5.21	24.08	30.14	24.17	15.09	17.12
Fossa (2003)	26.95	17.17	24.17	5.59	23.59	27.53	24.10	14.75	16.26

Note: G&Sc is the correlation of Gregory and Scott (1969), G&Sh indicates Greskovich and Shrier (1972), H&R is the Heywood & Richardson (1979) correlation, ND is Nydal (1991), ZB is from Zabaras (2000), and last, the correlation Fossa et al. (2003) is Fossa.

The Shell correlation presented the lowest average relative deviation from these seven correlations. Many authors have used this correlation to predict the frequency in numerical studies of horizontal flow. However, all correlations predicted the pressure wave velocity with a similar deviation to when we used the frequency from the pressure signal analysis of slug tracking simulations.

5.4 Case study

In Section 5.3, we compared the numerical and experimental pressure wave velocities. Test #3 presented the most significant relative deviation of all cases in this comparison. This experimental point has the lowest ratio of liquid and gas superficial velocities. Therefore, we

performed this case study to investigate the influence of the liquid's superficial velocity on predicting the pressure wave velocity.

In this way, we maintained the superficial velocity of the gas phase of Test #3 at the second steady state ($J_G = 0.6$ m/s), and we progressively increased the liquid's superficial velocity by 0.3 m/s for each point from 0.3 to 2.1 m/s. In addition, we plotted these points on the flow map for horizontal flow to ensure that the pattern is the slug. Figure 5.9 shows the flow map and the points evaluated. All these points are in the intermittent region.

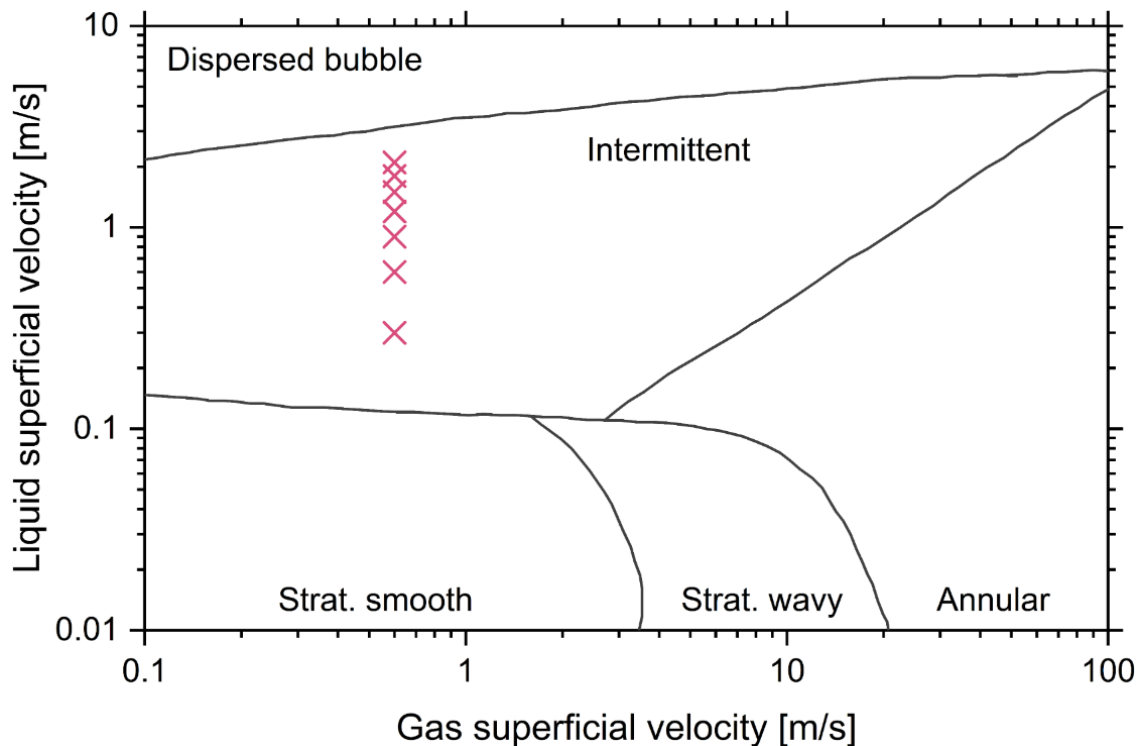


Figure 5.9. Flow pattern map for horizontal flow contains five patterns: dispersed bubble, intermittent, annular, stratified smooth, and stratified wavy; \times indicates the points evaluated in the case study.

In addition to the liquid and gas superficial velocities, we need the unit void fraction to employ the two-fluid model. For this purpose, we can use the unit cell model and correlations for the liquid slug aeration or the drift relation. The drift relationship represents the slug flow signature. Equation (5.3) shows this relation proposed by Zuber and Findlay (1965):

$$\frac{J_G}{\alpha_U} = C_0 J + C_\infty \sqrt{gD} . \quad (5.3)$$

Rearranging the terms in Eq. (5.3), we determine the unit void fraction by Eq. (5.4):

$$\alpha_U = \frac{J_G}{C_0 J + C_\infty \sqrt{gD}}, \quad (5.4)$$

where C_0 is the distribution parameter and C_∞ is the drift coefficient. Bendiksen (1984) proposed two closure relations to obtain the distribution parameter and the drift coefficient for horizontal and vertical flow. His relations depend on the liquid's superficial velocity and the pipe's diameter and inclination, as given by Eqs. (5.5) and (5.6):

$$C_0 = \begin{cases} 1.05 + 0.15 \sin^2 \theta, & Fr_{J_L} < 3.5 \\ 1.2 & , Fr_{J_L} \geq 3.5 \end{cases}, \quad (5.5)$$

$$C_\infty = \begin{cases} 0.54 \cos \theta + 0.35 \sin \theta, & Fr_{J_L} < 3.5 \\ 0.35 \sin \theta & , Fr_{J_L} \geq 3.5 \end{cases}, \quad (5.6)$$

where Fr_{J_L} is the liquid's superficial velocity Froude's number, as shown in Eq. (5.7):

$$Fr_{J_L} = \frac{J_L}{\sqrt{gD}}. \quad (5.7)$$

Therefore, we can obtain the unit void fraction for each point suggested. Table 5.5 shows the points and the predicted void fraction for each one.

Table 5.5. Case study's points and the void fraction prediction by the drift relation.

Case	J_G [m/s]	J_L [m/s]	α [-]
A	0.6	0.3	0.493
B		0.6	0.391
C		0.9	0.325
D		1.2	0.277
E		1.5	0.242
F		1.8	0.208
G		2.1	0.185

Finally, we performed a parametric analysis of the liquid's superficial velocity on the model employing the two-fluid model. We varied the frequency from 0.5 to 30 Hz to evaluate the curves. Figure 5.10 shows the liquid's superficial velocity influence on the prediction of pressure wave velocity.

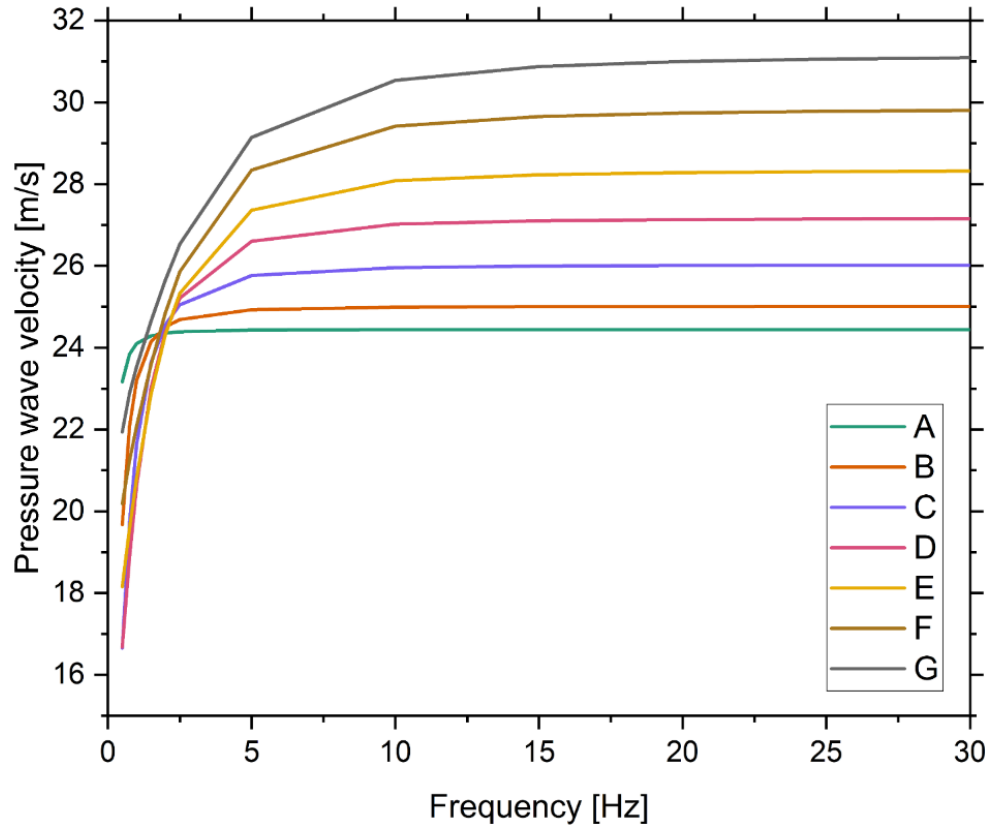


Figure 5.10. Liquid's superficial velocity influence in the pressure wave velocity curve; Case A has $J_L = 0.3$ m/s and increases progressively by 0.3 m/s until Case G, where $J_L = 2.1$ m/s.

Figure 5.10 shows some newsworthy features of the model. Case A is similar to Test #3; the curve presented the slightest variation of the pressure wave velocity between 0.5 Hz and 30 Hz frequencies. Table 5.6 shows the pressure wave velocity at the minor and major frequencies tested for each case and the difference between them.

Table 5.6. Pressure wave propagation velocity at 0.5 and 30 Hz and the difference between them.

Case	$c_{P@0.5Hz}$ [m/s]	$c_{P@30Hz}$ [m/s]	$ c_{P@30Hz} - c_{P@0.5Hz} $ [m/s]
A	23.171	24.445	1.275
B	19.676	25.011	5.335
C	16.653	26.018	9.365
D	16.680	27.154	10.475
E	18.158	28.318	10.160
F	20.186	29.803	9.617
G	21.940	31.091	9.151

As we increase the liquid's superficial velocity, the difference between the pressure wave velocity at these two frequencies increases until it reaches a value of around 10 m/s, as shown in Tab. 5.6. Therefore, overestimating the pressure wave velocity in Test #3 can be due to the small superficial velocity of the liquid phase at the second steady state due to the difference of minor and major pressure wave velocities.

In addition, the pressure wave velocity increases when the liquid's superficial velocity increases. This result agrees with the oscillatory mass-spring-damper system. In this case, a large amount of liquid compared to gas increases the oscillation frequency; consequently, the pressure wave velocity also increases.

Finally, we observed a displacement of the point where the pressure wave velocity achieves the maximum value; Case A achieves a constant value at 5 Hz, while Case G achieves it at approximately 20 Hz, for example.

5.5 Comparison with previous models

Many authors have been studying the pressure wave propagation velocity in two-phase flow since the '70s using the mixture's models as Wallis (1969), Henry et al. (1971), Samuel Martin and Padmanabhan (1979), and Matsui et al. (1979). More recently, Xu and Gong (2008) and Ishikawa et al. (2014) studied the pressure wave velocity using the two-fluid model and a

lumped-mass approach, respectively. All these authors presented a simple equation to predict the pressure wave velocity after some simplifications in their initial models.

As the pressure wave velocity achieves a constant value after a specific frequency, we suppose the previous models can estimate the maximum pressure wave velocity predicted by the two-fluid model. Therefore, we compared the value predicted by the previous models with the pressure wave velocity prediction by the two-fluid model at an oscillation frequency of 30 Hz. We established the polytropic constant γ equal to 1.4 for the model of Matsui et al. (1979) and the Bulk modulus of the air K_G equal to 142 kPa in the Ishikawa et al. (2014) model. Table 5.7 shows the pressure wave velocity predicted by previous models and the relative deviation compared to the maximum value calculated by the two-fluid model.

Table 5.7. Comparison of the pressure wave velocity predicted by previous models and the maximum value from the two-fluid model.

Model	#1		#2		#3		#4	
	c_p [Hz]	σ [%]						
Wallis (1969)	27.39	1.79	24.34	2.28	23.90	2.38	24.25	2.30
Henry et al. (1971)	812.96	2814.79	642.80	2480.92	543.55	2120.42	634.69	2456.88
SM&P (1979)	27.39	1.79	24.34	2.28	23.90	2.38	24.25	2.30
Matsui et al. (1979)	23.82	14.61	24.11	3.20	28.13	14.91	24.20	2.52
X&G (2008)	27.91	0.06	24.92	0.05	24.49	0.04	24.84	0.05
Ishikawa et al. (2014)	27.38	1.84	24.32	2.34	23.88	2.43	24.24	2.35

Note: SM&P corresponds to Samuel Martin and Padmanabhan's (1979) model, and the X&G is the model from Xu and Gong (2008).

All models could predict the maximum pressure wave velocity in the four cases with less than 15% deviation, but the Henry et al. (1971) model. Matsui et al. (1979) pointed out that the model of Henry et al. (1971) represents the fast pressure wave velocity, neglecting the strong wave attenuation when it passes from the liquid to the gas phase. On the other hand, Xu and Gong's (2008) model presented the best fit with a mean deviation of 5%; their model is also a

two-fluid model, showing the model's ability to study the slug flow in a transient regime. Figure 5.11 shows the maximum and the predicted pressure wave velocity for visualization. In this figure, we neglected the predicted value from Henry's model due to the higher deviation among the other models.

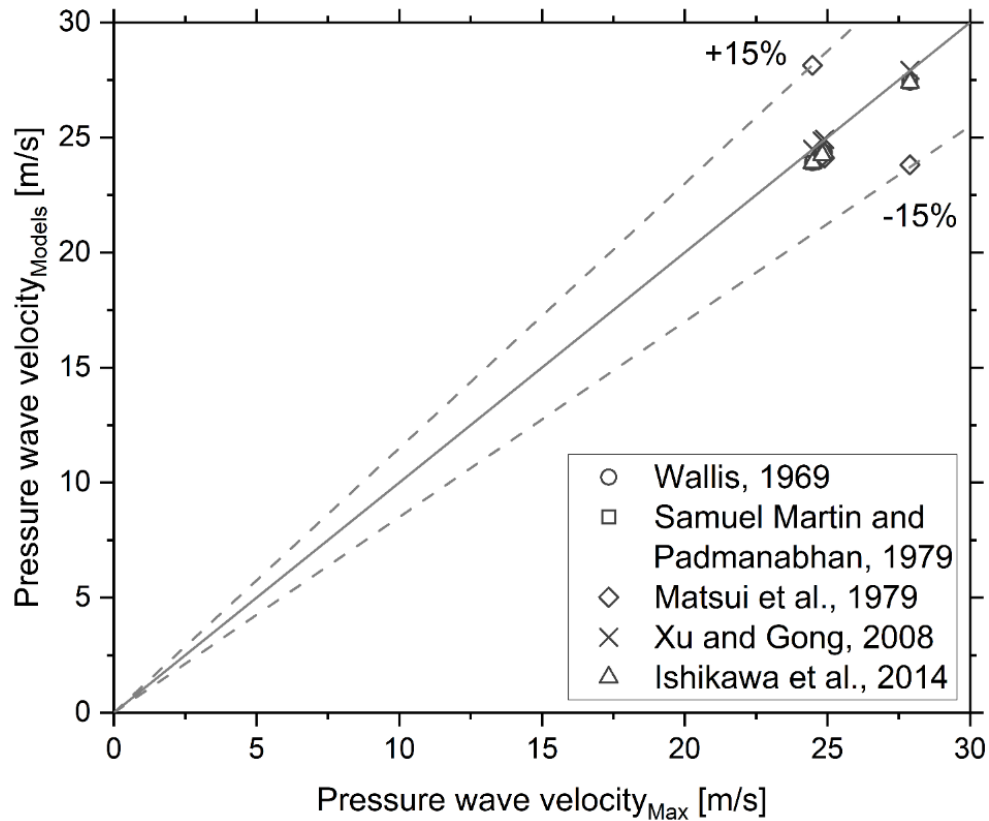


Figure 5.11. Maximum pressure wave velocity versus the prediction by previous models.

5.6 Attenuation coefficient

In addition to predicting the pressure wave velocity, the two-fluid model can also estimate the attenuation coefficient by the imaginary part of the wave number, as shown in Eq. (3.12). The results are in rad/m, and we converted them into dB/m. Although it is possible to calculate the numerical attenuation coefficient, Maria and Rosa (2016) did not obtain this variable experimentally. However, we can numerically observe the attenuation coefficient behavior for the four tests. Figure 5.12 shows the influence of the oscillation frequency on the attenuation coefficient for Tests #1 to #4.

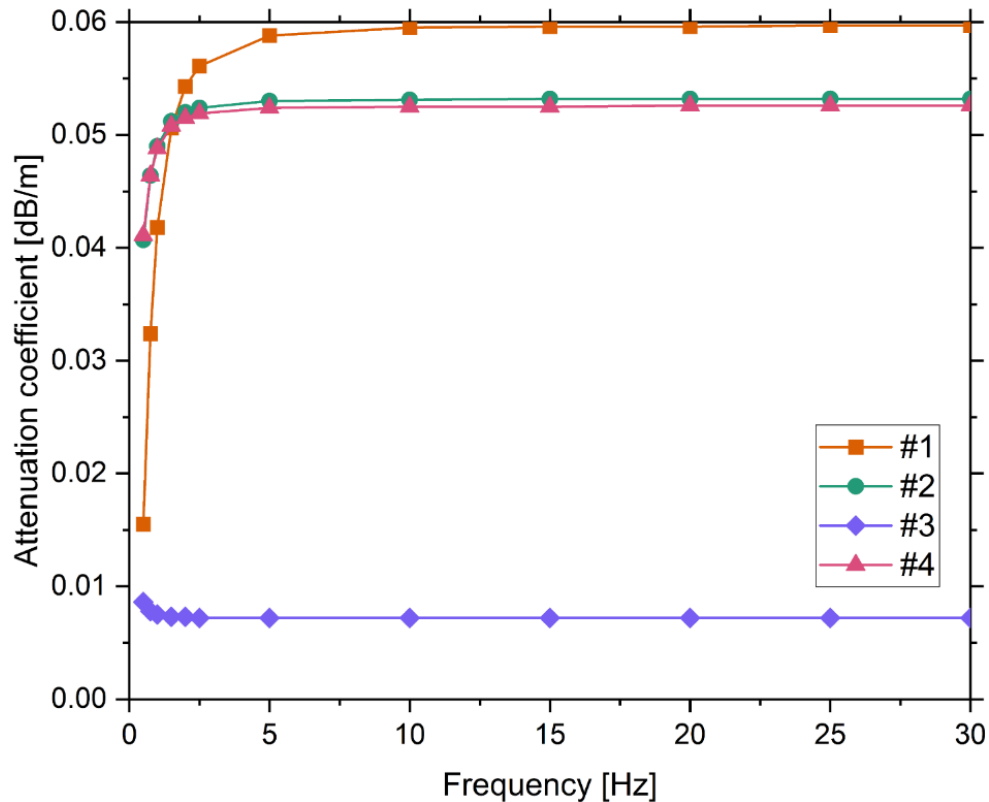


Figure 5.12. Attenuation coefficient for the four tests as a function of the oscillation frequency: —■— run #1, —●— run #2, —◆— run #3, and —▲— run #4.

The attenuation coefficient appears to have the same pressure wave velocity asymptotic behavior. However, this behavior differs from the one reported by Li et al. (2022a), where the attenuation coefficient presented a linear behavior with the frequency. The attenuation coefficient increased with the increase of the frequency for all Tests, but #3. This inverse behavior in Test #3 can be due to the small ratio of liquid's and gas' superficial velocities. Due to the liquid's viscosity, we expected more liquid within the pipe to cause a more significant attenuation coefficient. That is what happens. In the example of Test #1, where there is the biggest ratio of liquid and gas's superficial velocities, we also have the higher attenuation coefficient of all cases.

6 CONCLUSIONS

In this research, we have studied the pressure wave propagation phenomenon in a transient regime focusing on predicting the pressure wave velocity using the two-fluid model. The analytical two-fluid model presented was based on the models of Li et al. (2022a, 2012, 2016), Li et al. (2022b), and Lin et al. (2013). However, the model presented in this research has corrected typographical issues in the previous formulations.

In addition, we investigated the slug's frequency oscillations due to the importance of this parameter in the two-fluid model. The previous research neglected this analysis. The curve of pressure wave velocity as a function of frequency presents an asymptotic behavior, where the biggest variation occurs at minor frequencies. However, the oscillation frequency is located in this range of small frequencies. We analyzed the pressure and bubble's nose velocity signals from the slug tracking simulations performed by Gonçalves and Mazza (2022) to obtain this value. Both signals were analyzed using the Discrete Fourier Transform (DFT) to get a frequency spectrum for each case. We concluded from these analyses that the oscillation and passage frequency are related; thus, they can be estimated using one of the many correlations available in the literature.

Using the frequency resulting from the DFT analysis, we have calculated the pressure wave velocity employing the two-fluid model. The results were compared with the experimental data from the experimental campaign of Maria and Rosa (2016). Their experimental setup consists of a 26 mm ID horizontal pipe with four stations equipped with pressure and conductive sensors. The transient was imposed by changing the liquid and gas flow rates. The two-fluid model could predict the pressure wave velocity with a 17% mean deviation and less than 30% deviation for all cases. However, some points presented smaller deviations. This deviation is similar to the previously reported by Li et al. (2016).

The higher deviation occurs for Test #3. This point has the minor liquid's superficial velocity at the second steady state of all cases. Therefore, we performed a case study investigating the influence of the superficial velocity of the liquid phase on pressure wave propagation. Increasing the liquid's superficial velocity, we observed: an increase in the difference of the pressure wave velocity at 0.5 and 30 Hz, an increase in the maximum pressure wave velocity, and a displacement of the frequency where the maximum value is achieved.

As the oscillation frequency is related to the passage frequency, we compared the pressure wave velocity prediction using seven frequency of passage correlations with the experimental data from Maria and Rosa (2016). The Shell correlation resulted in a minor mean deviation of 15.13%. However, all correlations resulted in similar deviations when using the frequency resulting from DFT.

In addition, we can use the frequency of passage correlation and the drift relationship to close the two-fluid model. Therefore, we remove the need for previous experiments or slug-tracking simulations to estimate the pressure wave velocity using the two-fluid model. In this case, we only need to know the gas and liquid's superficial velocities at the second steady state. Thus, we can predict the pressure wave velocity relatively quickly.

We also compared the maximum pressure wave velocity predicted by the two-fluid model with previous models. All models could predict the maximum pressure wave velocity in the four cases with less than 15% deviation, but the Henry et al. (1971) model. However, Xu and Gong (2008) give the best fit with a mean deviation of 5%. Finally, we presented the numerical results of the attenuation coefficient as a function of the frequency.

For future works, we suggest performing an experimental study of the pressure wave propagation in horizontal flow for higher gas and liquid flow rates and compare with the two-fluid model. In addition, the study of the transient regime in a vertical experimental test section can be interesting due to the gas expansion effect and also in a pipe with slope variation along its length. Finally, exploring the two-fluid model to predict the pressure wave velocity in the vertical orientation could also be interesting.

References

AKAGAWA, K.; FUJII, T.; ITO, Y.; YAMAGUCHI, T.; FUKUHARA, K. Studies on shock phenomena in two-phase flow (2nd report, characteristics in slug flow region). **Bulletin of the JSME**, vol. 25, no. 201, p. 387–394, 1982. <https://doi.org/10.1299/jsme1958.25.387>.

AL-SAFRAN, E. M.; TAITEL, Y.; BRILL, J. P. Prediction of slug length distribution along a hilly terrain pipeline using slug tracking model. **Journal of Energy Resources Technology, Transactions of the ASME**, vol. 126, no. 1, p. 54–62, 2004. <https://doi.org/10.1115/1.1649971>.

AMBROSE, S.; HARGREAVES, D. M.; LOWNDES, I. S. Numerical modeling of oscillating Taylor bubbles. **Engineering Applications of Computational Fluid Mechanics**, vol. 10, no. 1, p. 578–598, 2016. <https://doi.org/10.1080/19942060.2016.1224737>.

ANDREUSSI, P.; BENDIKSEN, K. H.; NYDAL, O. J. Void distribution in slug flow. **Int. J. Multiphase Flow**, vol. 19, no. 5, p. 817–828, 1993. [https://doi.org/10.1016/0301-9322\(93\)90045-V](https://doi.org/10.1016/0301-9322(93)90045-V).

BARNEA, D.; TAITEL, Y. A model for slug length distribution in gas-liquid slug flow. **International Journal of Multiphase Flow**, vol. 19, no. 5, p. 829–838, 1993. [https://doi.org/10.1016/0301-9322\(93\)90046-W](https://doi.org/10.1016/0301-9322(93)90046-W).

BENDIKSEN, K. H. An experimental investigation of the motion of long bubbles in incline tubes. **Int. J. Multiphase Flow**, vol. 10, no. 4, p. 467–483, 1984. [https://doi.org/10.1016/0301-9322\(84\)90057-0](https://doi.org/10.1016/0301-9322(84)90057-0).

BERTOLA, V. **Modelling and experimentation in two-phase flow**. [S. l.]: Springer-Verlag Wien GmbH, 2003. <https://doi.org/10.1007/978-3-7091-2538-0>.

CAUSSADE, B.; FABRE, J.; JEAN, C.; OZON, P.; THERON, B. Unsteady phenomena in horizontal gas-liquid slug flow. 1989. **4th International Conference on Multi-Phase Flow [...]**. [S. l.: s. n.], 1989. p. 1–17.

COLEBROOK, C. F. Turbulent flow in pipes, with particular reference to the transition region between the smooth and rough pipe laws. **Journal of the Institution of Civil Engineers**, vol. 11, no. 4, p. 133–156, 1939. <https://doi.org/10.1680/ijoti.1939.13150>.

COOK, M.; BEHNIA, M. Film profiles behind liquid slugs in gas-liquid pipe flow. **AIChE Journal**, vol. 43, no. 9, p. 2180–2186, 1997. <https://doi.org/10.1002/aic.690430904>.

DUKLER, A. E.; HUBBARD, M. G. A model for gas-liquid slug flow in horizontal and near horizontal tubes. **Ind. Eng. Chem.**, vol. 14, no. 4, p. 337–347, 1975. <https://doi.org/10.1021/i160056a011>.

FABRE, J.; LINE, A. S.; PERESSON, L. Two-fluid/two-flow-pattern model for transient gas-liquid flow in pipes. 1989. **4th International Conference on Multi-Phase Flow** [...]. [*S. l.: s. n.*], 1989. p. 1–18.

FABRE, Jean; LINÉ, A.; GADOIN, E. Void and pressure waves in slug flow. 1995. **IUTAM Symposium on “Waves in Liquid/Gas and Liquid/Vapor Two Phase Systems”** [...]. [*S. l.: s. n.*], 1995. p. 1–20. https://doi.org/10.1007/978-94-011-0057-1_2.

FAGUNDES NETTO, J. R.; FABRE, J.; PERESSON, L. Shape of long bubbles in horizontal slug flow. **International Journal of Multiphase Flow**, vol. 25, no. 6–7, p. 1129–1160, 1999. [https://doi.org/10.1016/S0301-9322\(99\)00041-5](https://doi.org/10.1016/S0301-9322(99)00041-5).

FERNANDES, R. C.; SEMIAT, R.; DUKLER, A. E. Hydrodynamic model for gas-liquid slug flow in vertical tubes. **AIChE Journal**, vol. 29, no. 6, p. 981–989, 1983. <https://doi.org/10.1002/aic.690290617>.

FOSSA, M.; GUGLIELMINI, G.; MARCHITTO, A. Intermittent flow parameters from void fraction analysis. **Flow Measurement and Instrumentation**, vol. 14, no. 4–5, p. 161–168, 2003. [https://doi.org/10.1016/S0955-5986\(03\)00021-9](https://doi.org/10.1016/S0955-5986(03)00021-9).

GADOIN, E. **Régime intermittent “gaz-liquide” en conduite horizontale: écoulements non établis et transitoires**. 1993. 144 f. Institut National Polytechnique de Toulouse, 1993.

GONÇALVES, J. L.; MAZZA, R. A. A transient analysis of slug flow in a horizontal pipe using slug tracking model: Void and pressure wave. **International Journal of Multiphase Flow**, vol. 149, 2022. <https://doi.org/10.1016/j.ijmultiphaseflow.2022.103972>.

GREGORY, G. A.; SCOTT, D. S. Correlation of liquid slug velocity and frequency in horizontal co-current gas-liquid slug flow. **AIChE Journal**, vol. 15, no. 6, p. 933–935, 1969. <https://doi.org/10.1002/aic.690150623>.

GRESKOVICH, E. J.; SHRIER, A. L. Slug Frequency in Horizontal Gas-Liquid Slug Flow. **Industrial and Engineering Chemistry Process Design and Development**, vol. 11, no. 2, p.

317–318, 1972. <https://doi.org/10.1021/i260042a030>.

HENRY, R. E.; GROMES, M. A.; FAUSKE, H. K. **Pressure-pulse propagation in two-phase one- and two-component mixtures**. [S. l.]: Argonne National Laboratory, 1971. <https://doi.org/10.2172/4043485>.

HEWITT, G. F.; HALL-TAYLOR, N. S. **Annular two-phase flow**. [S. l.]: Pergamon Press, 1970. [https://doi.org/10.1016/0017-9310\(72\)90222-0](https://doi.org/10.1016/0017-9310(72)90222-0).

HEYWOOD, N. I.; RICHARDSON, J. F. Slug flow of air-water mixtures in a horizontal pipe: determination of liquid holdup by X-ray absorption. **Chemical Engineering Science**, vol. 34, no. 1, p. 17–30, 1979. [https://doi.org/10.1016/0009-2509\(79\)85174-X](https://doi.org/10.1016/0009-2509(79)85174-X).

HUANG, F.; TAKAHASHI, M.; GUO, L. Pressure wave propagation in air-water bubbly and slug flow. **Progress in Nuclear Energy**, vol. 47, no. 1–4, p. 648–655, 2005. <https://doi.org/10.1016/j.pnucene.2005.05.068>.

ISHII, M.; MISHIMA, K. Two-fluid model and hydrodynamic constitutive relations. **Nuclear Engineering and Design**, vol. 82, no. 2–3, p. 107–126, 1984. [https://doi.org/10.1016/0029-5493\(84\)90207-3](https://doi.org/10.1016/0029-5493(84)90207-3).

ISHIKAWA, S.; KONDOU, T.; MATSUZAKI, K.; EMOTO, H. Analysis of pressure wave in gas-liquid two-phase flows by concentrated mass model. **Transactions of the JSME (in Japanese)**, vol. 80, no. 814, p. 14, 2014. <https://doi.org/10.1299/transjsme.2014dr0166>.

KOKAL, S. L.; STANISLAV, J. F. An experimental study of two-phase flow in slightly inclined pipes I. **Chemical Engineering Science**, vol. 44, no. 3, p. 665–679, 1989. [https://doi.org/10.1016/0009-2509\(89\)85042-0](https://doi.org/10.1016/0009-2509(89)85042-0).

LI, H.; CHEN, R.; LI, X.; MENG, Y.; ZHU, L.; ZHAO, J. Investigation of pressure wave propagation and attenuation characteristics in wellbore gas-liquid two-phase flow. **Journal of Natural Gas Science and Engineering**, vol. 35, p. 1088–1100, 2016. <http://dx.doi.org/10.1016/j.jngse.2016.09.020>.

LI, H.; LI, G.; MENG, Y.; SHU, G.; ZHU, K.; XU, X. Attenuation law of MWD pulses in aerated drilling. **Petroleum Exploration and Development**, vol. 39, no. 2, p. 250–255, 2012. [https://doi.org/10.1016/S1876-3804\(12\)60039-1](https://doi.org/10.1016/S1876-3804(12)60039-1).

LI, H.; LIANG, J.; LI, C.; LI, G.; MENG, Y.; YANG, P.; LIU, J.; XU, L. A novel method to improve mud pulse telemetry performance during gaseated underbalanced drilling. **Journal of**

Petroleum Science and Engineering, vol. 213, no. February, p. 110400, 2022.
<https://doi.org/10.1016/j.petrol.2022.110400>.

LI, X.; ZHANG, J.; TANG, X.; LI, C.; LI, B.; WANG, Y.; ZHAO, Z. Propagation characteristics and application effects of measurement-while-drilling pressure wave for early gas-kick detection. **Journal of Loss Prevention in the Process Industries**, vol. 76, p. 104741, 2022. <https://doi.org/10.1016/j.jlp.2022.104741>.

LIN, Y.; KONG, X.; QIU, Y.; YUAN, Q. Calculation analysis of pressure wave velocity in gas and drilling mud two-phase fluid in annulus during drilling operations. **Mathematical Problems in Engineering**, vol. 2013, p. 1–17, 2013. <https://doi.org/10.1155/2013/318912>.

MANOLIS, I. G.; MENDES-TATSIS, M. A.; HEWITT, G. F. The effect of pressure on slug frequency in two-phase horizontal flow. *In*: SERIZAWA, A.; FUKANO, T.; BATAILLE, J. (eds.). **Advances in Multiphase Flow 1995: Proceedings of the Second International Conference on Multiphase Flow**. Kyoto, Japan: Elsevier Science B.V., 1995. p. 347–354. <https://doi.org/10.1016/B978-0-444-81811-9.50035-4>.

MARIA, L. D.; ROSA, E. S. Void fraction and pressure waves in a transient horizontal slug flow. **International Journal of Multiphase Flow**, vol. 84, p. 229–244, 2016. <https://doi.org/10.1016/j.ijmultiphaseflow.2016.05.008>.

MARTIN, C. S.; PADMANABAHN, M.; WIGGERT, D. C. Pressure wave propagation in two-phase bubbly air-water mixtures. 1976. **2nd International Conference on Pressure Surges** [...]. [*S. l.*: *s. n.*], 1976. p. 47–66.

MATSUI, G.; SUGIHARA, M.; ARIMOTO, S. Propagation characteristics of pressure wave through gas-liquid plug-train system (1st report, step response). **Bulletin of the JSME**, vol. 22, no. 173, p. 1562–1569, 1979. <https://doi.org/10.1299/jsme1958.22.1562>.

MIYAZAKI, K.; FUJII-E, Y.; SUITA, T. Propagation of pressure wave in air-water two-phase system, (I). **Journal of Nuclear Science and Technology**, vol. 8, no. 11, p. 606–613, 1971. <https://doi.org/10.1080/18811248.1971.9733020>.

NGUYEN, D. L.; WINTER, E. R. F.; GREINER, M. Sonic velocity in two-phase systems. **International Journal of Multiphase Flow**, vol. 7, p. 311–320, 1981. [https://doi.org/10.1016/0301-9322\(81\)90024-0](https://doi.org/10.1016/0301-9322(81)90024-0).

NICHOLSON, M. K.; AZIZ, K.; GREGORY, G. A. Intermittent two phase flow in horizontal pipes: predictive models. **The Canadian Journal of Chemical Engineering**, vol. 56, p. 653–663, 1978. <https://doi.org/10.1002/cjce.5450560601>.

- NYDAL, O. J. **An experimental investigation of slug flow**. 1991. University of Oslo, 1991.
- OMGBA-ESSAMA, C. **Numerical modelling of transient gas-liquid flows (Application to stratified & slug flow regimes)**. 2009. 252 f. Cranfield University, 2009.
- PARK, J. W.; DREW, D. A.; LAHEY, R. T. The analysis of void wave propagation in adiabatic monodispersed bubbly two-phase flows using an ensemble-averaged two-fluid model. **International Journal of Multiphase Flow**, vol. 24, no. 7, p. 1205–1244, 1998. [https://doi.org/10.1016/S0301-9322\(98\)00020-2](https://doi.org/10.1016/S0301-9322(98)00020-2).
- PRINGLE, C. C. T.; AMBROSE, S.; AZZOPARDI, B. J.; RUST, A. C. The existence and behaviour of large diameter Taylor bubbles. **International Journal of Multiphase Flow**, vol. 72, p. 318–323, 2015. <https://doi.org/10.1016/j.ijmultiphaseflow.2014.04.006>.
- RODRIGUES, H.T.; MORALES, R. E.; MAZZA, R. A.; ROSA, E. S. A comparative study of closure equations for gas-liquid slug flow. 2007. **19th International Congress of Mechanical Engineering [...]**. [S. l.: s. n.], 2007. p. 5–9.
- RODRIGUES, Hendy T. **Numerical simulation of slug flow employing a lagrangian tracking algorithm**. 2009. Federal Technological University at Curitiba, 2009.
- ROSA, E. S.; MAZZA, R. A.; MORALES, R. E.; RODRIGUES, H. T.; COZIN, C. Analysis of slug tracking model for gas-liquid flows in a pipe. **Journal of the Brazilian Society of Mechanical Sciences and Engineering**, vol. 37, no. 6, p. 1665–1686, 2015. <https://doi.org/10.1007/s40430-015-0331-7>.
- SAIDJ, F.; HASAN, A.; BOUYAHIAOUI, H.; ZEGHLOUL, A.; AZZI, A. Experimental study of the characteristics of an upward two-phase slug flow in a vertical pipe. **Progress in Nuclear Energy**, vol. 108, p. 428–437, 2018. <https://doi.org/10.1016/j.pnucene.2018.07.001>.
- SAKAGUCHI, T. Correlations for large bubble length, liquid slug length, slug unit length and slug period of gas-liquid two-phase slug flow in vertical pipes. 2001. **4th International Conference of Multiphase Flow, ICMF 2001 [...]**. [S. l.: s. n.], 2001.
- SAMUEL MARTIN, C.; PADMANABHAN, M. Pressure pulse propagation in two-component slug flow. **Journal of Fluids Engineering, Transactions of the ASME**, vol. 101, no. March, p. 44–52, 1979. <https://doi.org/10.1115/1.3448733>.
- SCHULKES, R. Slug frequencies revisited. 2011. **BHR Group - 15th International Conference on Multiphase Production Technology [...]**. [S. l.: s. n.], 2011. p. 311–325.

SHOHAM, O. **Mechanistic modeling of gas-liquid two-phase flow in pipes**. [S. l.]: Society of Petroleum Engineers, 2006. <https://doi.org/10.2118/9781555631079>.

TAITEL, Yehuda; BARNEA, D. Effect of gas compressibility on a slug tracking model. **Chemical Engineering Science**, vol. 53, no. 11, p. 2089–2097, 1998. [https://doi.org/10.1016/S0009-2509\(98\)00007-4](https://doi.org/10.1016/S0009-2509(98)00007-4).

TAITEL, Yehuda; BARNEA, D. Two-phase slug flow. **Advances in Heat Transfer**, New York, vol. 20, p. 83–132, 1990. [https://doi.org/10.1016/S0065-2717\(08\)70026-1](https://doi.org/10.1016/S0065-2717(08)70026-1).

TAITEL, Yehuda; BARNEA, D.; DUKLER, A. E. Modelling flow pattern transitions for steady upward gas-liquid flow in vertical tubes. **AIChE Journal**, vol. 26, no. 3, p. 345–354, 1980. <https://doi.org/10.1002/aic.690260304>.

TAITEL, Yemada; DUKLER, A. E. A model for predicting flow regime transitions in horizontal and near horizontal gas-liquid flow. **AIChE Journal**, vol. 22, no. 1, p. 47–55, 1976. <https://doi.org/10.1002/aic.690220105>.

THÉRON, B. **Ecoulements instationnaires intermittents de gaz et de liquide en conduite horizontale**. 1989. Inst. Natl Polytech de Toulouse, 1989.

VAN HOUT, R.; SHEMER, L.; BARNEA, D. Spatial distribution of void fraction within a liquid slug and some other related slug parameters. **International Journal of Multiphase Flow**, vol. 18, no. 6, p. 831–845, 1992. [https://doi.org/10.1016/0301-9322\(92\)90062-L](https://doi.org/10.1016/0301-9322(92)90062-L).

VIGNERON, F.; SARICA, C.; BRILL, J. P. Experimental analysis of imposed two-phase flow transients in horizontal pipelines. 14., 1995. **7th International Conference on Multiphase Production, Organized and sponsored by BHR Group Limited [...]**. [S. l.: s. n.], 1995. vol. 14, p. 199–217.

WALLIS, G. B. **One-dimensional two-phase flow**. [S. l.]: McGraw-Hill, Inc., 1969.

WANG, X.; GUO, L.; ZHANG, X. Development of liquid slug length in gas-liquid slug flow along horizontal pipeline: experiment and simulation. **Chinese Journal of Chemical Engineering**, vol. 14, no. 5, p. 626–633, 2006. [https://doi.org/10.1016/S1004-9541\(06\)60125-0](https://doi.org/10.1016/S1004-9541(06)60125-0).

XU, X.-X.; GONG, J. A united model for predicting pressure wave speeds in oil and gas two-phase pipeflows. **Journal of Petroleum Science and Engineering**, vol. 60, p. 150–160, 2008. <https://doi.org/10.1016/j.petrol.2007.05.012>.

ZABARAS, G. J. Prediction of slug frequency for gas/liquid flows. **SPE Journal**, vol. 5, no. 3, 2000. <https://doi.org/10.2118/56462-MS>.

ZHENG, G.; BRILL, J. P.; TAITEL, Y. Slug flow behavior in a hilly terrain pipeline. **International Journal of Multiphase Flow**, vol. 20, no. 1, p. 63–79, 1994. [https://doi.org/10.1016/0301-9322\(94\)90006-X](https://doi.org/10.1016/0301-9322(94)90006-X).

ZUBER, N.; FINDLAY, J. A. Average volumetric concentration in two-phase flow systems. **Journal of Heat Transfer**, , p. 453–468, 1965. <https://doi.org/10.1115/1.3689137>.

APPENDIX A – Review of pressure wave propagation velocity

	Method	Main results	Research gap	Simplified equation
Wallis (1969)	- Homogeneous model.	<ul style="list-style-type: none"> - The pressure wave velocity in a two-phase flow is less than the acoustic velocity of each phase; - The pressure wave velocity achieves its minimum at 50% of the void fraction. 	- The homogeneous case is unsuitable for slug flow.	$c_p = \frac{1}{\sqrt{[\alpha_U \rho_G + (1 - \alpha_U) \rho_L] \left(\frac{1 - \alpha_U}{\rho_L a_L^2} + \frac{\alpha_U}{\rho_G a_G^2} \right)}}$
Henry et al. (1971)	<ul style="list-style-type: none"> - Idealized model for slug flow; - Experimental method. 	<ul style="list-style-type: none"> - The model reproduces their experimental data; - The model for slug flow is a simple equation that depends on the void fraction and the acoustic velocity of each fluid. 	<ul style="list-style-type: none"> - The idealized model does not reproduce the real hydrodynamics of the slug flow; - The authors found that the pressure wave velocity decreased with void fraction. However, other models found a U-shaped curve with a minimum when the void fraction is 0.5. 	$c_p = \left[\frac{\alpha}{a_G} + \frac{(1 - \alpha)}{a_L} \right]^{-1}$

	Method	Main results	Research gap	Simplified equation
Miyazaki et al. (1971)	<ul style="list-style-type: none"> - Homogeneous model; - Stagnant mixture of gas-liquid to focus on the drift flux; - Experimental method. 	<ul style="list-style-type: none"> - The pressure wave velocity appeared to be independent of the pressure pulse; - They presented a mass-spring simplified model to study the pressure propagation in a heterogeneous media; - As in Wallis (1969), the authors found that the pressure wave velocity in a two-phase flow is less than in each phase separately. 	<ul style="list-style-type: none"> - They analyzed only vertical flows; - Does not consider the shape change of the pressure wave along the pipe; - They evaluated the pressure wave for the void fraction range 0 to 60% and used a single model for this range; - For the higher void fraction within the operating range, the model presented higher deviation when compared with the experimental data; however, this higher void fraction is where the slug pattern tends to occur. 	-

	Method	Main results	Research gap	Simplified equation
Martin et al. (1976)	<ul style="list-style-type: none"> - Homogeneous model; - Method of characteristics; - Experimental method. 	<ul style="list-style-type: none"> - The homogeneous one-dimensional model can predict the pressure transient. 	<ul style="list-style-type: none"> - The model is suitable only for bubbly flow. 	-
Samuel Martin and Padmanabhan (1979)	<ul style="list-style-type: none"> - Mixture models: homogeneous and drift-flux; - Experimental method. 	<ul style="list-style-type: none"> - The proposed homogeneous model presented better results for the pressure wave velocity than Henry et al.'s (1971) model; - They found that the pressure wave velocity for slug flow predicted by the drift-flux model is the same as that by the homogeneous model. 	<ul style="list-style-type: none"> - The authors suggested that a two-fluid model is more suitable for studying the pressure wave velocity. 	$\frac{c_P}{a_G} = \left\{ \begin{array}{l} \alpha_U (1 - \alpha_U) \frac{\rho_L}{\rho_G} + \alpha_U^2 + \\ + \left(\frac{a_G}{a_L} \right)^2 \left[(1 - \alpha_U)^2 + \alpha_U (1 - \alpha_U) \frac{\rho_G}{\rho_L} \right] \end{array} \right\}^{-0.5}$

	Method	Main results	Research gap	Simplified equation
Matsui et al. (1979)	<ul style="list-style-type: none"> - Mass-spring model using linear and non-linear approaches; - Similar model of idealized slug flow previously proposed by Henry et al. (1971); - Experimental method; they injected air and water alternately into the pipe to reproduce the idealized slug. 	<ul style="list-style-type: none"> - The natural frequency has its minimum at 50% of void fraction, and it is symmetrical to this point; - The model and experimental results agreed qualitatively; - The number of cells within the pipe influences the pressure wave velocity; the results also agreed qualitatively for more than ten cells. 	<ul style="list-style-type: none"> - The idealized model does not reproduce the real hydrodynamics of the slug flow; 	$c_p = \sqrt{\frac{\gamma P}{\rho_L \beta (1 - \beta)}}$
Nguyen et al. (1981)	<ul style="list-style-type: none"> - Idealized model for slug flow; 	<ul style="list-style-type: none"> - The model depends on the void fraction and the acoustic velocity of each fluid; - The model presented good results compared with experimental data of stratified, slug, and homogeneous flow for all void fraction ranges. 	<ul style="list-style-type: none"> - The idealized model does not reproduce the real hydrodynamics of the slug flow; - They found the same relation for slug flow as Henry et al. (1971). 	$c_p = \left[\frac{\alpha}{a_G} + \frac{(1 - \alpha)}{a_L} \right]^{-1}$

	Method	Main results	Research gap	Simplified equation
Akagawa et al. (1982)	<ul style="list-style-type: none"> - Oscillatory mass-spring model; - Homogeneous model with a similar approach to water hammer analysis; - Experimental method. 	<ul style="list-style-type: none"> - The pressure profile depends on the flow configuration adjacent to the valve when it closes. It can vary accordingly to the configuration, even for the same gas and liquid flow rates; - The transient profile when of slug type has high oscillation frequency and fast amplitude decrease; - The mass-spring model presented good results with experimental data when the adjacent configuration is gas type. 	<ul style="list-style-type: none"> - The homogeneous model is unsuitable for slug flow. 	-
Caussade et al. (1989)	<ul style="list-style-type: none"> - Drift-flux model; - Experimental method. 	<ul style="list-style-type: none"> - The pressure wave has a higher velocity than the void fraction wave; - They described the propagation mechanism of the pressure and void waves. - The void fraction wave is shape-conservative. 	<ul style="list-style-type: none"> - The authors quote that the experimental results are limited to capturing waves with an amplitude higher than a limit and waves that travel downstream. 	-

	Method	Main results	Research gap	Simplified equation
Vigneron et al. (1995)	<ul style="list-style-type: none"> - Comparison with commercial software; - Experimental method. 	<ul style="list-style-type: none"> - The void propagation velocity is almost equal to the bubble's nose velocity at the second steady state, either for an increase or decrease of the liquid flow rate; - The data showed that a change in the gas flow rate causes fast transients, and the liquid flow rate causes slow transients. 	<ul style="list-style-type: none"> - The experimental test section has a large diameter (77.9 mm). 	-
Fabre et al. (1995)	<ul style="list-style-type: none"> - Drift-flux model; - Experimental method. 	<ul style="list-style-type: none"> - The void wave is shape-conservative and propagates with the elongated bubble's nose velocity; - The pressure wave has a dispersive feature. 	<ul style="list-style-type: none"> - The model underpredicts the pressure wave velocity. 	-

	Method	Main results	Research gap	Simplified equation
Huang et al. (2005)	<ul style="list-style-type: none"> - Experimental method; - Comparison with numerical results. 	<ul style="list-style-type: none"> - The pressure wave in slug flow has a dispersive feature sharper than in the bubbly regime; -The pressure wave velocity and wave attenuation increase with the frequency; - The pressure propagation velocity has no significant variation for void fractions less than 50%; however, it increases after this value. 	<ul style="list-style-type: none"> - The results presented focus more on the bubbly regime; - The authors found a different trend for the pressure wave velocity as a function of the void fraction. 	-
Ambrose et al. (2016)	<ul style="list-style-type: none"> - CFD – finite volume method; 	<ul style="list-style-type: none"> - They found that the bubble ascended with variable translational velocity, accelerating and decelerating. This phenomenon occurs only at the bubble’s nose. - The experimental findings agreed with the numerical results only in the initial part of the pipe; -The oscillation frequency depends on the average bubble length. 	<ul style="list-style-type: none"> - They studied the bubble oscillation rising in a stagnant liquid; - Due to the mesh, tiny bubbles are not captured by the numerical model. 	-

	Method	Main results	Research gap	Simplified equation
Ishikawa et al. (2014)	<ul style="list-style-type: none"> - Mass-spring-damper analogy; - Lumped mass approach; - Perturbation theory. 	<ul style="list-style-type: none"> - The model agreed well with experimental data of an air conditioning system. 	<ul style="list-style-type: none"> - The model is based on the bubbly flow; - The model validation was for a one-component flow in an air conditioning system. 	$c_p = \sqrt{\frac{K_G}{\alpha_U [\rho_G \alpha_U + \rho_L (1 - \alpha_U)]}}$
Maria and Rosa (2016)	<ul style="list-style-type: none"> - Experimental method; 	<ul style="list-style-type: none"> - The results showed a time delay of 6 seconds between the two steady states; this time depends on the experimental setup; - Comparison with the previous models to predict the pressure wave propagation velocity; - They suggested that the properties of the slug flow at the second steady state are more suitable for predicting the pressure wave propagation velocity; - They presented important features of the pressure and void waves in horizontal flow. 	<ul style="list-style-type: none"> - The experimental approach involves the test repetition 100 times for each point; this is time-consuming. - The test grid has a few points. 	-

	Method	Main results	Research gap	Simplified equation
Gonçalves and Mazza (2022)	<ul style="list-style-type: none"> - Slug tracking; - Mass-spring-damper analogy coupled by the liquid velocity at the slug; 	<ul style="list-style-type: none"> - The time delay between the two steady states influences the pressure wave velocity; however, do not influence the void fraction wave; - Reproduce the experimental results of Maria and Rosa (2016) with a less than 10% deviation. 	<ul style="list-style-type: none"> - Despite presenting a good agreement with the experimental data of Maria and Rosa (2016), the simulation of pressure and void waves using slug tracking is a demanding task; - The slug tracking simulations need an initial condition, which they used the experimental data. However, when no experimental data are available, it is complex to provide this initial condition. 	$b_1\ddot{u}_s + b_2\dot{u}_s + b_3u_s = f(t)$
Xu and Gong (2008)	<ul style="list-style-type: none"> - Two-fluid model. 	<ul style="list-style-type: none"> - For all values of the virtual mass coefficient tested, the pressure wave velocity has a sharp decrease in the void fraction range of 0 – 5%; - The pressure wave velocity versus void fraction curve remains almost the same for virtual mass coefficients larger than 1. 	<ul style="list-style-type: none"> - No mention of the oscillation frequency. 	$c_p = \sqrt{\frac{\left[\frac{c_{vm}\rho_L}{\alpha_U(1-\alpha_U)^2} + \frac{\rho_G}{\alpha_U} + \frac{\rho_L}{(1-\alpha_U)} \right]}{\left[\frac{\rho_L}{(1-\alpha_U)a_G^2} + \frac{\rho_G}{\alpha_U a_L^2} \right] \left\{ 1 + c_{vm} \left[\frac{\alpha_U}{(1-\alpha_U)} + \frac{\rho_L}{\rho_G} \right] \right\}}}$

	Method	Main results	Research gap	Simplified equation
Li et al. (2012)	<ul style="list-style-type: none"> - Two-fluid model; - Method of characteristics; 	<ul style="list-style-type: none"> - The pressure wave velocity increases with the angular frequency until 100 rad/s; - They compared the results with data from measurement while drilling, finding a good agreement. 	<ul style="list-style-type: none"> - They used the frequency fixed at 50 rad/s; - The model equations presented typographical errors. 	-
Lin et al. (2013)	<ul style="list-style-type: none"> - Two-fluid model; - Method of characteristics; 	<ul style="list-style-type: none"> - The pressure wave velocity has a sharp decrease in the void fraction range of 0 – 5%; - The pressure wave velocity versus void fraction curve presented a U shape, as reported by Xu and Gong (2008) previously. 	<ul style="list-style-type: none"> - The results presented are for annular pipes; - They used the frequency fixed at 50 rad/s; - The model equations presented typographical errors. 	-

	Method	Main results	Research gap	Simplified equation
Li et al. (2016)	<ul style="list-style-type: none"> - Two-fluid model; - Method of characteristics; 	<ul style="list-style-type: none"> - The comparison with Henry et al.'s (1971) experimental data showed that 88% of these are in $\pm 25\%$ deviation; - For the attenuation coefficient, they compared to Huang et al.'s (2005) data and found that the model could predict with less than 20% deviation; - The pressure wave velocity and attenuation coefficient change with the angular frequency; - As reported previously, the pressure wave velocity versus the void fraction curve presented a U shape. 	<ul style="list-style-type: none"> - They did not investigate the frequency parameter needed as an input value on their model; - The model equations presented typographical errors. 	-

	Method	Main results	Research gap	Simplified equation
Li et al. (2022a)	<ul style="list-style-type: none"> - Two-fluid model presented by Li et al. (2016); - Method of characteristics; 	<ul style="list-style-type: none"> - They presented the influencing parameter on the pressure wave velocity and attenuation factor: void fraction, operating frequency, and system pressure; - The pressure wave increases fast with the frequency at lower frequencies range and reaches an approximately constant value. 	<ul style="list-style-type: none"> - They used the frequency fixed at 50 rad/s; - The model equations presented typographical errors. 	-
Li et al. (2022b)	<ul style="list-style-type: none"> - Two-fluid model; - Method of characteristics; 	<ul style="list-style-type: none"> - They compared the results with the experimental data from Huang et al. (2005) and Henry et al. (1971) in a void fraction range from 0 to 30% and found a good agreement; - The model could predict the gas kick occurrence 7 to 9 minutes earlier than previous models. 	<ul style="list-style-type: none"> - The model equations presented typographical errors. 	-

APPENDIX B – Two-fluid model mathematical details

This chapter presents the details of two-fluid modeling based on the models of Li et al. (2022a, 2012, 2016), Li et al. (2022b), and Lin et al. (2013). Some typographical errors in the previous research were corrected in the following equations. We started with the closure relations needed in the model evaluation. Then, we approached the continuity and momentum equations for gas and liquid phases.

Closure relations

The two-fluid model is evaluated using closure relations. Equation (B.1) gives the force in the interface wall-liquid.

$$F_{WL} = \frac{2}{D} C_{f_{WL}} \rho_L V_L |V_L|, \quad (\text{B.1})$$

where $C_{f_{WL}}$ is the Fanning friction factor, given by the equation proposed by Colebrook (1939), as shown in Eq. (B.2):

$$\frac{1}{\sqrt{C_f}} = -4 \log_{10} \left(\frac{\varepsilon/D}{3.7} + \frac{1.256}{Re_L \sqrt{C_f}} \right), \quad (\text{B.2})$$

where Re_L is the Reynolds number of the liquid phase, as shown in Eq. (B.3):

$$Re_L = \frac{\rho_L V_L D}{\mu_L}. \quad (\text{B.3})$$

As shown in Eq. (B.4), the force in the gas-liquid interface is assumed to be the sum of the drag and virtual mass forces.

$$F_{GL} = F_D + F_{vm}. \quad (\text{B.4})$$

The two following equations give the drag and virtual mass forces:

$$F_D = \frac{3}{8} \frac{c_{dg} \alpha_U \rho_L (V_G - V_L) |V_G - V_L|}{R_b}, \quad (\text{B.5})$$

$$F_{vm} = c_{vm} \alpha_U \rho_L \left[\left(\frac{\partial V_G}{\partial t} + V_G \frac{\partial V_G}{\partial x} \right) - \left(\frac{\partial V_L}{\partial t} + V_L \frac{\partial V_L}{\partial x} \right) \right], \quad (\text{B.6})$$

where c_{dg} is the drag coefficient, R_b is the bubble radius, and c_{vm} is the virtual mass coefficient. Equation (B.7) shows the drag coefficient proposed by Lin et al. (2013), and Eq. (B.8) shows the virtual mass coefficient proposed by Nicholson et al. (1978), both for slug flow:

$$c_{dg} = 110(1 - \alpha_U)^3 R_b, \quad (\text{B.7})$$

$$c_{vm} = 3.3 + 1.7 \left[\frac{\left(1 - \frac{\sqrt{\alpha_U}}{15} \right)}{\left(1 - \frac{\sqrt{\alpha_U}}{45} \right)} \right]. \quad (\text{B.8})$$

We can also employ the two-fluid model for different patterns, only changing the virtual mass and drag coefficients closure relations. For dispersed bubble flow, Ishii and Mishima (1984) proposed the following:

$$c_{dg} = \frac{4}{3} R_b \sqrt{\frac{g(\rho_G - \rho_L)}{\sigma}} \left[\frac{1 + 17.67(1 - \alpha_U)^{9/7}}{18.67(1 - \alpha_U)^{1.5}} \right]^2, \quad (\text{B.9})$$

$$c_{vm} = \frac{1}{2} \alpha_U \frac{1 + 2\alpha_U}{1 - \alpha_U}, \quad (\text{B.10})$$

where σ is the interfacial tension between the gas and liquid phases. Park et al. (1998) suggested a correlation to obtain this parameter, as shown in Eq. (B.11):

$$\sigma = -0.3\rho_L(V_G - V_L)^2. \quad (\text{B.11})$$

Two-fluid model

Equations (B.12) and (B.13) show the mass conservation equations for gas and liquid phases:

$$\frac{\partial}{\partial t}(\alpha_U \rho_G) + \frac{\partial}{\partial x}(\alpha_U \rho_G V_G) = 0, \quad (\text{B.12})$$

$$\frac{\partial}{\partial t}[(1 - \alpha_U) \rho_L] + \frac{\partial}{\partial x}[(1 - \alpha_U) \rho_L V_L] = 0. \quad (\text{B.13})$$

Equations (B.14) and (B.15) show the momentum conservation equations for gas and liquid phases:

$$\frac{\partial}{\partial t}(\alpha_U \rho_G V_G) + \frac{\partial}{\partial x}(\alpha_U \rho_G V_G^2) + \alpha_U \frac{\partial P}{\partial x} = -F_{GL} - F_{WG} - \alpha_U \rho_G g \sin\theta, \quad (\text{B.14})$$

$$\frac{\partial}{\partial t}[(1 - \alpha_U) \rho_L V_L] + \frac{\partial}{\partial x}[(1 - \alpha_U) \rho_L V_L^2] + (1 - \alpha_U) \frac{\partial P}{\partial x} = F_{GL} - F_{WL} + (1 - \alpha_U) \rho_L g \sin\theta. \quad (\text{B.15})$$

Assuming that the in situ velocities of the phases are related to superficial velocities by the equations above for gas and liquid phases, respectively:

$$V_G = \frac{J_G}{\alpha_U}, \quad (\text{B.16})$$

$$V_L = \frac{J_L}{(1-\alpha_U)}. \quad (\text{B.17})$$

The pressure differential and the density differential of the phase are related to the sound speed in that phase by Laplace's equation, as shown below for gas and liquid phases, respectively:

$$a_G^2 = \frac{\partial P}{\partial \rho_G}, \quad (\text{B.18})$$

$$a_L^2 = \frac{\partial P}{\partial \rho_L}. \quad (\text{B.19})$$

Rewriting the continuity equations shown in (B.12) and (B.13), we have the Eqs. (B.20) and (B.21):

$$\rho_G \frac{\partial \alpha_U}{\partial t} + \frac{\alpha_U}{a_G^2} \frac{\partial P}{\partial t} + \rho_G V_G \frac{\partial \alpha_U}{\partial x} + \frac{\alpha_U V_G}{a_G^2} \frac{\partial P}{\partial x} + \alpha_U \rho_G \frac{\partial V_G}{\partial x} = 0, \quad (\text{B.20})$$

$$-\rho_L \frac{\partial \alpha_U}{\partial t} + \frac{(1-\alpha_U)}{a_L^2} \frac{\partial P}{\partial t} - \rho_L J_L \frac{\partial \alpha_U}{\partial x} + \frac{(1-\alpha_U) V_L}{a_L^2} \frac{\partial P}{\partial x} + (1-\alpha_U) \rho_L \frac{\partial V_L}{\partial x} = 0. \quad (\text{B.21})$$

Rewriting the momentum equations presented in (B.14) and (B.15), we have the Eqs. (B.22) and (B.23):

$$\begin{aligned} \alpha_U \rho_G \frac{\partial V_G}{\partial t} + \alpha_U V_G \frac{\partial \rho_G}{\partial t} + \rho_G V_G \frac{\partial \alpha_U}{\partial t} + 2\alpha_U \rho_G V_G \frac{\partial V_G}{\partial x} + \alpha_U V_G^2 \frac{\partial \rho_G}{\partial x} + \\ + \rho_G V_G^2 \frac{\partial \alpha_U}{\partial x} + \alpha_U \frac{\partial P}{\partial x} = -F_{GL} - F_{WG} - \alpha_U \rho_G g \sin \theta \end{aligned}, \quad (\text{B.22})$$

$$\begin{aligned}
& -\rho_L V_L \frac{\partial \alpha_U}{\partial t} + (1 - \alpha_U) \rho_L \frac{\partial V_L}{\partial t} + \frac{(1 - \alpha_U) V_L}{a_L^2} \frac{\partial P}{\partial t} - \rho_L V_L^2 \frac{\partial \alpha}{\partial x} + \\
& + 2(1 - \alpha_U) V_L \rho_L \frac{\partial V_L}{\partial x} + \frac{(1 - \alpha_U) V_L^2}{a_L^2} \frac{\partial P}{\partial x} + (1 - \alpha_U) \frac{\partial P}{\partial x} = F_{GL} - F_{WL} + \cdot \quad (B.23) \\
& \quad \quad \quad - (1 - \alpha_U) \rho_L g \sin \theta
\end{aligned}$$

Applying the closure relations (Eq. (B.1), (B.4), (B.5), and (B.6)) in the momentum equations and neglecting the force at the wall-gas interface ($F_{WG} = 0$), we have the following for gas and liquid phases:

$$\begin{aligned}
& \alpha_U (\rho_G + c_{vm} \rho_L) \frac{\partial V_G}{\partial t} - c_{vm} \alpha_U \rho_L \frac{\partial V_L}{\partial t} + \frac{\alpha_U V_G}{a_G^2} \frac{\partial P}{\partial t} + \rho_G V_G \frac{\partial \alpha_U}{\partial t} + \rho_G V_G^2 \frac{\partial \alpha_U}{\partial x} + \\
& + V_G \alpha_U (2\rho_G + c_{vm} \rho_L) \frac{\partial V_G}{\partial x} + \alpha_U \left(1 + \frac{V_G^2}{a_G^2} \right) \frac{\partial P}{\partial x} - c_{vm} \alpha_U \rho_L J_L \frac{\partial V_L}{\partial x} = \quad , \quad (B.24) \\
& \quad \quad \quad = -\frac{3 c_{dg} \alpha_U \rho_L (V_G - V_L)^2}{8 R_b} - \alpha_U \rho_G g \sin \theta
\end{aligned}$$

$$\begin{aligned}
& -c_{vm} \alpha_U \rho_L \frac{\partial V_G}{\partial t} + \rho_L [(1 - \alpha_U) + c_{vm} \alpha_U] \frac{\partial V_L}{\partial t} + \frac{(1 - \alpha_U) V_L}{a_L^2} \frac{\partial P}{\partial t} - \rho_L V_L \frac{\partial \alpha_U}{\partial t} + \\
& -\rho_L V_L^2 \frac{\partial \alpha_U}{\partial x} + V_L \rho_L [2(1 - \alpha_U) + c_{vm} \alpha_U] \frac{\partial V_L}{\partial x} + (1 - \alpha_U) \left(1 + \frac{V_L^2}{a_L^2} \right) \frac{\partial P}{\partial x} + \quad . \quad (B.25) \\
& -c_{vm} \alpha_U \rho_L V_G \frac{\partial V_G}{\partial x} = \frac{3 c_{dg} \alpha_U \rho_L (V_G - V_L)^2}{8 R_b} - \frac{2}{D} C f_{WL} \rho_L V_L |V_L| - (1 - \alpha_U) \rho_L g \sin \theta
\end{aligned}$$

As shown in Eq. (B.26), the perturbation theory says that one variable is the sum of its value on the unperturbed state with a small oscillatory amount.

$$Z = Z_0 + Z', \quad (B.26)$$

where Z is one of the following variables: V_G , V_L , P , and α_U ; thus, rewriting the continuity equations, we have the following:

$$\rho_G \frac{\partial \alpha_U'}{\partial t} + \frac{\alpha_{U0}}{a_G^2} \frac{\partial P'}{\partial t} + \rho_G V_{G0} \frac{\partial \alpha_U'}{\partial x} + \frac{\alpha_{U0} V_{G0}}{a_G^2} \frac{\partial P'}{\partial x} + \alpha_{U0} \rho_G \frac{\partial V_G'}{\partial x} = 0, \quad (\text{B.27})$$

$$-\rho_L \frac{\partial \alpha_U'}{\partial t} + \frac{(1-\alpha_{U0})}{a_L^2} \frac{\partial P'}{\partial t} - \rho_L V_{L0} \frac{\partial \alpha_U'}{\partial x} + \frac{(1-\alpha_{U0}) V_{L0}}{a_L^2} \frac{\partial P'}{\partial x} + (1-\alpha_{U0}) \rho_L \frac{\partial V_L'}{\partial x} = 0. \quad (\text{B.28})$$

Also, rewriting the momentum equations with Eq. (B.26) and neglecting high-order terms, we have the following:

$$\begin{aligned} & \alpha_{U0} (\rho_G + c_{vm} \rho_L) \frac{\partial V_G'}{\partial t} - c_{vm} \alpha_{U0} \rho_L \frac{\partial V_L'}{\partial t} + \frac{\alpha_{U0} V_{G0}}{a_G^2} \frac{\partial P'}{\partial t} + \rho_G V_{G0} \frac{\partial \alpha_U'}{\partial t} + \\ & + \rho_G V_{G0}^2 \frac{\partial \alpha_U'}{\partial x} + V_{G0} \alpha_{U0} (2\rho_G + c_{vm} \rho_L) \frac{\partial V_G'}{\partial x} + \alpha_{U0} \left(I + \frac{V_{G0}^2}{a_G^2} \right) \frac{\partial P'}{\partial x} + \quad , \quad (\text{B.29}) \\ & - c_{vm} \alpha_{U0} \rho_L V_{L0} \frac{\partial V_L'}{\partial x} = \frac{3 c_{dg} \alpha_{U0} \rho_L (V_{G0} V_L' + V_{L0} V_G')}{4 R_b} - (\alpha_{U0} + \alpha_U') \rho_G g \sin \theta \end{aligned}$$

$$\begin{aligned} & - c_{vm} \alpha_{U0} \rho_L \frac{\partial V_G'}{\partial t} + \rho_L [(1-\alpha_{U0}) + c_{vm} \alpha_{U0}] \frac{\partial V_L'}{\partial t} + \frac{(1-\alpha_{U0}) V_{L0}}{a_L^2} \frac{\partial P'}{\partial t} + \\ & - \rho_L V_{L0} \frac{\partial \alpha_U'}{\partial t} - \rho_L V_{L0}^2 \frac{\partial \alpha_U'}{\partial x} + V_{L0} \rho_L [2(1-\alpha_{U0}) + c_{vm} \alpha_{U0}] \frac{\partial V_L'}{\partial x} + \quad .(\text{B.30}) \\ & + (1-\alpha_{U0}) \left(I + \frac{V_{L0}^2}{a_L^2} \right) \frac{\partial P'}{\partial x} - c_{vm} \alpha_{U0} \rho_L V_{G0} \frac{\partial V_G'}{\partial x} = - \frac{3 c_{dg} \alpha_{U0} \rho_L (V_{G0} V_L' + V_{L0} V_G')}{4 R_b} + \\ & - \frac{4}{D} C_{f_{WL}} \rho_L V_{L0} V_L' - [1 - (\alpha_{U0} + \alpha_U')] \rho_L g \sin \theta \end{aligned}$$

Equation (B.31) shows the small oscillatory equation:

$$Z' = \delta Z_0 e^{i(\omega t - \kappa x)}, \quad (\text{B.31})$$

where κ is the wave number, x is the position, and Z_0 is one of the following variables: V_{G0} , V_{L0} , P_0 , and α_{U0} . Rewriting and reorganizing the continuity and momentum equations (Eqs. (B.27) to (B.30)), we have:

$$\rho_G (\omega - \kappa V_{G0}) \alpha_U' + \frac{\alpha_{U0}}{a_G^2} (\omega - \kappa V_{G0}) P' - \alpha_{U0} \rho_G \kappa V_G' = 0, \quad (\text{B.32})$$

$$-\rho_L (\omega - \kappa V_{L0}) \alpha_U' + \frac{(1 - \alpha_{U0})}{a_L^2} (\omega - \kappa V_{L0}) P' - (1 - \alpha_{U0}) \rho_L \kappa V_L' = 0, \quad (\text{B.33})$$

$$\begin{aligned} & [\rho_G V_{G0} (\omega - \kappa V_{G0}) - i \rho_G g \sin \theta] \alpha_U' + \left[\frac{\alpha_{U0} V_{G0}}{a_G^2} (\omega - \kappa V_{G0}) - \alpha_{U0} \kappa \right] P' + \\ & + \left[\alpha_{U0} (\rho_G + c_{vm} \rho_L) (\omega - \kappa V_{G0}) - \rho_G V_{G0} \alpha_{U0} \kappa + \frac{3}{4} i \frac{c_{dg} \alpha_{U0} \rho_L V_{L0}}{R_b} \right] V_G' +, \quad (\text{B.34}) \\ & + \left[-c_{vm} \alpha_{U0} \rho_L (\omega - V_{L0} \kappa) + \frac{3}{4} i \frac{c_{dg} \alpha_{U0} \rho_L V_{G0}}{R_b} \right] V_L' = \alpha_{U0} i \rho_G g \sin \theta \end{aligned}$$

$$\begin{aligned} & [\rho_L V_{L0} (\omega - \kappa V_{L0}) - i \rho_L g \sin \theta] \alpha_U' - \left[\frac{V_{L0}}{a_L^2} (1 - \alpha_{U0}) (\omega - \kappa V_{L0}) - \kappa (1 - \alpha_{U0}) \right] P' + \\ & + \left[c_{vm} \alpha_{U0} \rho_L (\omega - \kappa V_{G0}) + \frac{3}{4} i \frac{c_{dg} \alpha_{U0} \rho_L V_{L0}}{R_b} \right] V_G' + \\ & - \left\{ \begin{aligned} & \rho_L [(1 - \alpha_{U0}) + c_{vm} \alpha_{U0}] (\omega - \kappa V_{L0}) - \kappa (1 - \alpha_{U0}) V_{L0} \rho_L + \\ & - \frac{3}{4} i \frac{c_{dg} \alpha_{U0} \rho_L V_{G0}}{R_b} - \frac{4}{D} i C f_{WL} \rho_L V_{L0} \end{aligned} \right\} V_L' = \quad (\text{B.35}) \\ & = -(1 - \alpha_{U0}) i \rho_L g \sin \theta \end{aligned}$$

Finally, we can write the Eqs. (B.32) to (B.35) in the format of a inhomogeneous linear system as presented previously in Chapter 3.

APPENDIX C – Slug tracking model details

This appendix presents the mathematical details of the slug tracking model. A complete description of the modeling and programming is in Rosa et al. (2015) and Rodrigues (2009).

Figure 3.1 shows the representation of the j^{th} cell, its structures, and the model's variables of interest. The figure is repeated below for convenience:

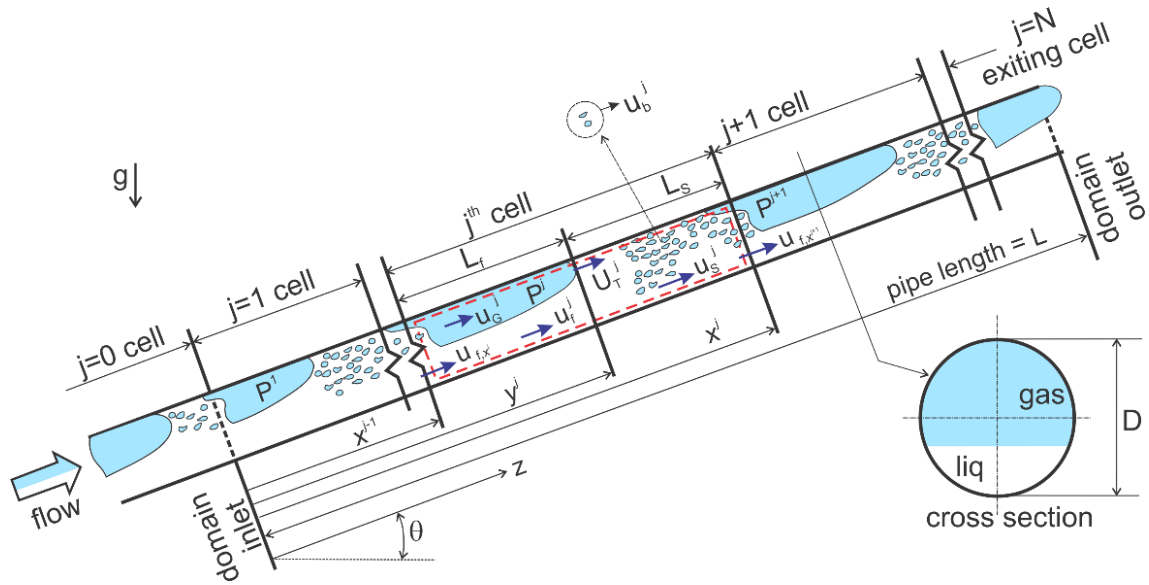


Figure B.1. Properties and index of the cells in the slug tracking model - Rosa et al. (2015) adapted.

The coordinates x and y are parallel to the pipe axis and are measured from a stationary frame of reference. The x and y coordinates have a special role in the model; they track the heads of each liquid slug and gas bubble. These coordinates also define the bubble head velocity and the axial lengths of the liquid slug and the liquid film:

$$U_T^j = \frac{dy^j}{dt}, \quad (\text{C.1})$$

$$L_S^j = x^j - y^j \Rightarrow \frac{dL_S^j}{dt} = \frac{dx^j}{dt} - \frac{dy^j}{dt}, \quad (\text{C.2})$$

$$L_f^j = y^j - x^{j-1} \Rightarrow \frac{L_f^j}{dt} = \frac{dy^j}{dt} - \frac{dx^{j-1}}{dt}. \quad (\text{C.3})$$

The mass flow rates of the liquid and gas phases crossing the y^j boundary are defined as:

$$\dot{m}_{L,y^j} = \rho_L \left(u_{f,y^j} - \frac{dy^j}{dt} \right) R_{f,y^j} A \equiv \rho_L \left(u_{s,y^j} - \frac{dy^j}{dt} \right) R_{s,y^j} A, \quad (\text{C.4})$$

$$\dot{m}_{G,y^j} = \rho_{G,y^j}^j \left(u_{G,y^j} - \frac{dy^j}{dt} \right) (1 - R_{f,y^j}) A \equiv \rho_{G,y^j}^j \left(u_{b,y^j} - \frac{dy^j}{dt} \right) (1 - R_{s,y^j}) A. \quad (\text{C.5})$$

Since R_s , u_s , and u_b are considered uniform throughout the slug region and representative of the corresponding averaged values, the associated boundary values at y^j are also coincident with the lumped values:

$$R_{s,y^j} = R_s^j, \quad (\text{C.6})$$

$$u_{s,y^j} = u_s^j, \quad (\text{C.7})$$

$$u_{b,y^j} = u_b^j. \quad (\text{C.8})$$

Therefore, the face subscripts can be dropped, except for the gas density, which varies significantly. Thus, the Eqs. (C.4) and (C.5) are simplified to:

$$\dot{m}_{L,y^j} = \rho_L \left(u_s^j - \frac{dy^j}{dt} \right) R_s^j A, \quad (\text{C.9})$$

$$\dot{m}_{G,y^j} = \rho_{G,y^j}^j \left(u_b^j - \frac{dy^j}{dt} \right) (1 - R_s^j) A. \quad (\text{C.10})$$

Similarly, the mass flow rates of the liquid and gas phases crossing the x^j boundary are defined as:

$$\dot{m}_{L,x^j} = \rho_L \left(u_{f,x^j} - \frac{dx^j}{dt} \right) R_{f,x^j} A \equiv \rho_L \left(u_{S,x^j} - \frac{dx^j}{dt} \right) R_{S,x^j} A, \quad (\text{C.11})$$

$$\dot{m}_{G,x^j} = \rho_{G,x^j}^j \left(u_{G,x^j} - \frac{dx^j}{dt} \right) (1 - R_{f,x^j}) A \equiv \rho_{G,x^j}^j \left(u_{b,x^j} - \frac{dx^j}{dt} \right) (1 - R_{S,x^j}) A. \quad (\text{C.12})$$

Using the same assumptions, the face subscripts are dropped. Thus, the Eqs. (C.11) and (C.12) are simplified to:

$$\dot{m}_{L,x^j} = \rho_L \left(u_s^j - \frac{dx^j}{dt} \right) R_s^j A, \quad (\text{C.13})$$

$$\dot{m}_{G,x^j} = \rho_{G,x^j}^j \left(u_b^j - \frac{dx^j}{dt} \right) (1 - R_s^j) A. \quad (\text{C.14})$$

The hypothesis of a uniform liquid slug velocity u_s throughout the liquid slug does not accurately predict the mass flow rate crossing the x^j and y^j boundaries because the velocity field is truly tri-dimensional on these boundaries. Also, liquid slug hold-up R_s is non-uniform; it has a high value in the wake of the elongated bubble and then decreases.

Liquid and gas mass equation

Liquid and gas mass balance at the unit cell can be written by:

$$A \frac{d}{dt} (\rho_L R_f^j L_f^j + \rho_L R_s^j L_s^j) + \dot{m}_{L,x^j} - \dot{m}_{L,x^{j-1}} = 0, \quad (\text{C.15})$$

$$A \frac{d}{dt} \left[\rho_G^j (1 - R_f^j) L_f^j + \rho_G^j (1 - R_s^j) L_s^j \right] + \dot{m}_{G,x^j} - \dot{m}_{G,x^{j-1}} = 0. \quad (\text{C.16})$$

Substituting the Eqs. (C.1) to (C.3) and Eq. (C.13) into Eq. (C.15):

$$\left(R_s^{j-1} - R_f^j \right) \frac{dx^{j-1}}{dt} + \left(R_f^j - R_s^j \right) \frac{dy^j}{dt} + L_f^j \frac{dR_f^j}{dt} + L_s^j \frac{dR_s^j}{dt} = u_s^{j-1} R_s^{j-1} - u_s^j R_s^j. \quad (\text{C.17})$$

Now, substituting the Eqs. (C.1) to (C.3) and Eq. (C.14) into Eq. (C.16):

$$\begin{aligned} & - \left(R_f^j - R_s^j \right) \frac{dy^j}{dt} - \left[I - \frac{\rho_{G,x^{j-1}}^{j-1}}{\rho_{G,x^j}^j} - R_f^j + \frac{\rho_{G,x^{j-1}}^{j-1}}{\rho_{G,x^j}^j} R_s^{j-1} \right] \frac{dx^{j-1}}{dt} - L_f^j \frac{dR_f^j}{dt} - L_s^j \frac{dR_s^j}{dt} = \\ & -u_b^j (1 - R_s^j) + u_b^{j-1} \frac{\rho_{G,x^{j-1}}^{j-1}}{\rho_{G,x^j}^j} (1 - R_s^{j-1}) - \left[(1 - R_f^j) L_f^j + (1 - R_s^j) L_s^j \right] \frac{1}{\rho_G^j} \frac{d\rho_G^j}{dt} \end{aligned} \quad (\text{C.18})$$

The gas and liquid mass equation is the sum of the Eqs. (C.17) and (C.18), shown as:

$$\begin{aligned} & \left[(1 - R_f^j) L_f^j + (1 - R_s^j) L_s^j \right] \frac{1}{\rho_G^j} \frac{d\rho_G^j}{dt} = - \left[R_s^{j-1} \left(I - \frac{\rho_{G,x^{j-1}}^{j-1}}{\rho_{G,x^j}^j} \right) - I + \frac{\rho_{G,x^{j-1}}^{j-1}}{\rho_{G,x^j}^j} \right] \frac{dx^{j-1}}{dt} + \\ & + u_s^{j-1} R_s^{j-1} - u_s^j R_s^j - u_b^j (1 - R_s^j) + u_b^{j-1} \frac{\rho_{G,x^{j-1}}^{j-1}}{\rho_{G,x^j}^j} (1 - R_s^{j-1}) \end{aligned} \quad (\text{C.19})$$

Momentum equation

The procedures to get the transient gas-liquid momentum are based on the steady-state approach of Taitel and Barnea (1990). The balance is performed at the j^{th} cell for the gas and liquid using a stationary and inertial frame of reference. The frame encompasses the j^{th} cell, with one of its surfaces coincident with the pipe wall while the others match the pipe cross-section. For the j^{th} cell, the cross-section coincides with the j^{th} bubble tail position at x^{j-1} upstream and the $(j+1)^{\text{th}}$ bubble tail position at x^j downstream. Under these assumptions, the gas and liquid momentum balance over the j^{th} cell is:

$$\begin{aligned}
& \frac{d}{dt} \int_0^{L_f} \left(\rho_L R_f^j u_f^j + \rho_G^j (1 - R_f^j) u_G^j \right) A dz_f + \frac{d}{dt} \int_0^{L_s} \left(\rho_L R_s^j u_s^j + \rho_G^j (1 - R_s^j) u_b^j \right) A dz_s + \\
& + \left(u_{L,x^j} \dot{m}_{L,x^j} + u_{G,x^j} \dot{m}_{G,x^j} \right) - \left(u_{L,x^{j-1}} \dot{m}_{L,x^{j-1}} + u_{G,x^{j-1}} \dot{m}_{G,x^{j-1}} \right) = (P_G^j - P_G^{j+1}) A + \\
& - g \sin \theta \left\{ \left[\rho_L R_f^j + \rho_G^j (1 - R_f^j) \right] L_f^j + \left[\rho_L R_s^j + \rho_G^j (1 - R_s^j) \right] L_s^j \right\} A + \quad .(C.20) \\
& - \tau_s^j S L_s^j - \left(\tau_f^j S_f^j + \tau_G^j S_G^j \right) L_f^j + g \cos \theta D \left[\rho_L \xi_{L,x^{j-1}} R_{f,x^{j-1}} - \rho_L \xi_{L,x^j} R_{f,x^j} \right] A + \\
& + g \cos \theta D \left\{ \rho_{G,x^{j-1}} \xi_{G,x^{j-1}} \left(1 - R_{f,x^{j-1}} \right) - \rho_{G,x^j} \xi_{G,x^j} \left(1 - R_{f,x^j} \right) \right\} A
\end{aligned}$$

The film region for the j^{th} cell, the cross-section is coincident with the j^{th} bubble nose position at y^j downstream and with the j^{th} bubble tail position at x^{j-1} upstream, and the momentum balance at this region is:

$$\begin{aligned}
& \frac{d}{dt} \int_0^{L_f} \left(\rho_L R_f^j u_f^j + \rho_G^j (1 - R_f^j) u_G^j \right) A dz_f + \left(u_{L,y^j} \dot{m}_{L,y^j} + u_{G,y^j} \dot{m}_{G,y^j} \right) + \\
& - \left(u_{L,x^{j-1}} \dot{m}_{L,x^{j-1}} + u_{G,x^{j-1}} \dot{m}_{G,x^{j-1}} \right) = -g \sin \theta \left\{ \left[\rho_L R_f^j + \rho_G^j (1 - R_f^j) \right] L_f^j \right\} A + \quad .(C.21) \\
& - \left(\tau_f^j S_f^j + \tau_G^j S_G^j \right) L_f^j + g \cos \theta D \left[\rho_L \xi_{L,x^{j-1}} R_{f,x^{j-1}} - \rho_L \xi_{L,y^j} R_{f,y^j} \right] A + \\
& + g \cos \theta D \left\{ \rho_{G,x^{j-1}} \xi_{G,x^{j-1}} \left(1 - R_{f,x^{j-1}} \right) - \rho_{G,y^j} \xi_{G,y^j} \left(1 - R_{f,y^j} \right) \right\} A
\end{aligned}$$

Substituting the Eq. (C.21) into the momentum balance of the j^{th} cell represented by the Eq. (C.20), the momentum time rate in the film region can be expressed, and the momentum equation of the j^{th} cell turns to:

$$\begin{aligned}
& A \frac{d}{dt} \left[\left(\rho_L R_s^j u_s^j + \rho_G^j (1 - R_s^j) u_b^j \right) L_s^j \right] + \left(u_{L,x^j} \dot{m}_{L,x^j} - u_{L,y^j} \dot{m}_{L,y^j} \right) + \\
& + \left(u_{G,x^j} \dot{m}_{G,x^j} - u_{G,y^j} \dot{m}_{G,y^j} \right) = (P_G^j - P_G^{j+1}) A - g \sin \theta \left\{ \left[\rho_L R_s^j + \rho_G^j (1 - R_s^j) \right] L_s^j \right\} A + \quad .(C.22) \\
& - \tau_s^j S L_s^j + g \cos \theta D \rho_L \left(\xi_{L,y^j} R_{f,y^j} - \xi_{L,x^j} R_{f,x^j} \right) A + \\
& + g \cos \theta D \left[\rho_{G,y^j} \xi_{G,y^j} \left(1 - R_{f,y^j} \right) - \rho_{G,x^j} \xi_{G,x^j} \left(1 - R_{f,x^j} \right) \right] A
\end{aligned}$$

Considering that the gas density is much less than the liquid's density ($\rho_G \ll \rho_L$), the

equation simplifies to:

$$A \frac{d}{dt} (\rho_L R_S^j u_S^j L_S^j) + (u_{L,x^j} \dot{m}_{L,x^j} - u_{L,y^j} \dot{m}_{L,y^j}) = (P_G^j - P_G^{j+1}) A + \rho_L R_S^j L_S^j A g \sin \theta - \tau_s^j S L_S^j + g \cos \theta D \rho_L (\xi_{L,y^j} R_{f,y^j} - \xi_{L,x^j} R_{f,x^j}) A \quad (C.23)$$

Substituting the mass liquid flow rate definition at y and x cross-sections through the Eqs. (C.9), (C.11), and (C.13). Although, other definitions need to rewrite this term as demonstrated in Eqs. (C.24) and (C.25). The liquid velocity crossing the y transverse section is the liquid's velocity in the liquid slug itself:

$$u_{L,y^j} = u_S^j. \quad (C.24)$$

Equation (C.25) shows the liquid velocity crossing the x transversal section is the liquid velocity at the film of the j^{th} cell, which is related to u_S^j Eq. (C.11).

$$u_{L,x^j} = u_{f,x^j} = u_S^j \left(\frac{R_S^j}{R_f^{j+1}} \right) + \left(\frac{R_f^{j+1} - R_S^j}{R_f^{j+1}} \right) \frac{dx^j}{dt}. \quad (C.25)$$

So, rewritten the second term of Eq.(C.23) as:

$$\begin{aligned} (u_{L,x^j} \dot{m}_{L,x^j} - u_{L,y^j} \dot{m}_{L,y^j}) = & \left[u_S^j \left(\frac{R_S^j}{R_f^{j+1}} \right) - \frac{dx^j}{dt} \left(\frac{R_S^j}{R_f^{j+1}} - 1 \right) \right] \left\{ \rho_L \left(u_S^j - \frac{dx^j}{dt} \right) R_S^j A \right\} + \\ & - \left\{ u_S^j \rho_L R_S^j A \left(u_S^j - \frac{dy^j}{dt} \right) \right\} \end{aligned} \quad (C.26)$$

The x position of the j^{th} cell coincides with the bubble's tail of the $j+1^{\text{th}}$ cell. Therefore, the liquid hold-up at x is the liquid film hold-up of the $j+1^{\text{th}}$ cell. In addition, the coordinates of the center of pressure are equal in these positions:

$$R_{f,x^j} = R_f^{j+1}, \quad (C.27)$$

$$\xi_{L,x^j} = \xi_L^{j+1}. \quad (\text{C.28})$$

The y position coincides with the elongated bubble's nose for the j th cell, and it considers that the liquid slug occupies the entire cross-section. Considering an aerated slug piston, the liquid hold-up and the coordinate of the center of pressure for the liquid and gas is:

$$R_{f,y^j} = R_S^j, \quad (\text{C.29})$$

$$\xi_{L,y^j} = \frac{1}{2}, \quad (\text{C.30})$$

where the center of pressure of the liquid and gas are determined hereafter. Finally, the momentum balance as a function of u_s , u_b , and geometrical parameters of the j th cell is:

$$\begin{aligned} & \rho_L R_S^j L_S^j \frac{du_s^j}{dt} + \rho_L R_S^j (u_s^j)^2 \left\{ \left(\frac{R_S^j}{R_f^{j+1}} - 1 \right) \left(1 - \frac{dx^j/dt}{u_s^j} \right)^2 \right\} = \\ & = \left(P_G^j - P_G^{j+1} \right) - \rho_L R_S^j L_S^j g \sin \theta - \tau_s^j \frac{S}{A} L_S^j + g \cos \theta D \rho_L R_S^j \left(\frac{1}{2} - \xi_L^{j+1} \frac{R_f^{j+1}}{R_S^j} \right) \end{aligned} \quad (\text{C.31})$$

The mass and momentum balances are complicated to be solved directly, and more simplifications should be made. It is considered a smooth gas density variation between two consecutive cells; thus, we have the Eq. (C.32):

$$\frac{\rho_{G,x^{j-1}}^{j-1}}{\rho_{G,x^j}^j} \approx 1. \quad (\text{C.32})$$

The liquid and gas mass conservation in the j th is:

$$\begin{aligned} & \left[(1 - R_f^j) L_f^j + (1 - R_s^j) L_s^j \right] \frac{1}{\rho_G^j} \frac{d\rho_G^j}{dt} = u_s^{j-1} R_S^{j-1} - u_s^j R_S^j + u_b^{j-1} (1 - R_S^{j-1}) + \\ & - u_b^j (1 - R_S^j) \end{aligned} \quad (\text{C.33})$$

It is considered a perfect gas state equation to the gas phase along an isothermal process to relate the gas density to pressure as:

$$\frac{1}{\rho_G^j} \frac{d\rho_G^j}{dt} = \frac{1}{P_G^j} \frac{dP_G^j}{dt}. \quad (\text{C.34})$$

Substituting the Eq. (C.34) into Eq. (C.33), we obtain the liquid and gas mass balance in the j^{th} :

$$\left[(1 - R_f^j) L_f^j + (1 - R_s^j) L_s^j \right] \frac{1}{P_G^j} \frac{dP_G^j}{dt} = u_s^{j-1} R_s^{j-1} - u_s^j R_s^j + u_b^{j-1} (1 - R_s^{j-1}) + u_b^j (1 - R_s^j). \quad (\text{C.35})$$

The gas velocity in the liquid slug is related to the mixture velocity with a constitutive relationship, as shown in Eq. (C.36):

$$u_b^j = c_b^j u_M^j + u_d^j. \quad (\text{C.36})$$

In addition, the mixture velocity is related to the liquid velocity in the liquid slug:

$$u_M^j = u_s^j R_s^j + u_b^j (1 - R_s^j). \quad (\text{C.37})$$

Substituting the Eq. (C.37) into Eq. (C.36), the gas velocity in the liquid slug is:

$$u_b^j = \frac{c_b^j u_s^j R_s^j + u_d^j}{1 - c_b^j (1 - R_s^j)}. \quad (\text{C.38})$$

Substituting the Eq. (C.38) into Eq. (C.37), the mixture velocity is:

$$u_M^j = \frac{u_s^j R_s^j}{1 - c_b^j (1 - R_s^j)} + \frac{u_d^j (1 - R_s^j)}{1 - c_b^j (1 - R_s^j)}. \quad (\text{C.39})$$

Substituting the Eq. (C.39) into Eq. (C.35), the mass balance in the j^{th} is:

$$\begin{aligned} \left[(1-R_f^j)L_f^j + (1-R_s^j)L_s^j \right] \frac{1}{P_G^j} \frac{dP_G^j}{dt} = & \frac{u_s^{j-1}R_s^{j-1}}{1-c_b^{j-1}(1-R_s^{j-1})} - \frac{u_s^j R_s^j}{1-c_b^j(1-R_s^j)} + \\ & + \frac{u_d^{j-1}(1-R_s^{j-1})}{1-c_b^{j-1}(1-R_s^{j-1})} - \frac{u_d^j(1-R_s^j)}{1-c_b^j(1-R_s^j)} \end{aligned} \quad (\text{C.40})$$

Regarding the momentum balance, is used a closure relationship for wall shear stress for turbulent flow in the liquid slug as:

$$\tau_s^j = C_f^j \frac{1}{2} \rho_M^j u_M^j |u_M^j|. \quad (\text{C.41})$$

Substituting Eq. (C.39) into Eq. (C.41):

$$\tau_s^j = C_f^j \frac{1}{2} \rho_M^j |u_M^j| \frac{u_s^j R_s^j}{1-c_b^j(1-R_s^j)} + C_f^j \frac{1}{2} \rho_M^j |u_M^j| \frac{u_d^j(1-R_s^j)}{1-c_b^j(1-R_s^j)}. \quad (\text{C.42})$$

Thus, substituting Eq. (C.42) into Eq.(C.31), and disregarding the hydrostatic term, the momentum balance becomes:

$$\begin{aligned} \frac{du_s^j}{dt} = & -(u_s^j)^2 \left\{ \frac{1}{L_s^j} \left(\frac{R_s^j}{R_f^{j+1}} - 1 \right) \left(1 - \frac{dx^j/dt}{u_s^j} \right)^2 \right\} + \frac{(P_G^j - P_G^{j+1})}{R_s^j L_s^j \rho_L} - g \sin \theta + \\ & - u_s^j \left[2C_f^j \frac{\rho_M^j}{\rho_L} \frac{|u_M^j|}{D} \frac{1}{R_s^j} \frac{R_s^j}{1-c_b^j(1-R_s^j)} + 2C_f^j \frac{\rho_M^j}{\rho_L} \frac{|u_M^j|}{DR_s^j} \frac{u_d^j}{u_s^j} \frac{(1-R_s^j)}{1-c_b^j(1-R_s^j)} \right]. \end{aligned} \quad (\text{C.43})$$

The fourth-order Runge-Kutta method numerically evaluates the mass and momentum equations using Object Oriented Programming in FORTRAN.

APPENDIX D – Two-fluid model code on Wolfram Mathematica

Oscillation model

```
in[ ]:= Clear["Global`*"]
|apaga
```

Section 1: Definitions

i = Imaginary number [--]
 g = Gravity [m/s^2]
 θ = Pipe inclination [rad]
 ϵ = Pipe roughness [m]
 σ = Superficial tension [N/m]
 a_G = Sound velocity in gas [m/s]
 a_L = Sound velocity in liquid [m/s]
 μ_L = Liquid dynamic viscosity [Pa.s]
 ρ_G = Gas density [kg/m^3]
 ρ_L = Liquid density [kg/m^3]
 J_G = Gas superficial velocity [m/s]
 J_L = Liquid superficial velocity [m/s]
 V_G = Gas velocity [m/s]
 V_L = Liquid velocity [m/s]
 α = Cell's void fraction [--]
 f = Frequency [Hz]
 ω = Angular frequency [rad/s]
 cdg = drag force coefficient [--]
 cvm = virtual mass coefficient [--]
 Re_L = Liquid's Reynolds number [--]
 C_f = Fanning friction factor [--]
 κ = Wave number [rad/m]
 R_b = Bubble radius [m]
 c = Pressure wave velocity [m/s]
 η = Attenuation coefficient [--]

Section 2: Flow conditions

```

(*Fixed parameters*)
i =  $\sqrt{-1}$ ;
g = 9.81 (*m/s2*);
Diameter = 0.026 (*m*);
 $\theta$  = 0 (*rad*);
 $\epsilon$  = 0 (*m*);
 $\sigma$  = 0.075;
aG = 347.1 (*m/s*); (*Li et al., 2016*)
aL = 1501 (*m/s*); (*Li et al., 2016*)
 $\mu_L$  =  $8.55 \cdot 10^{-4}$  (*Pa.s*);
 $\mu_G$  =  $1.7 \cdot 10^{-5}$  (*Pa.s*);
 $\rho_G$  = 1.18 (*kg/m3*);
 $\rho_L$  = 999 (*kg/m3*);

(*Variable parameters*)
JG = (*insert value*) (*m/s*);
JL = (*insert value*) (*m/s*);
 $\alpha$  = (*insert value*);
f = (*insert value*) (*Hz*);

```

Section 3: Two-fluid model

```

(*Parameters*)
VG = JG /  $\alpha$ ;
VL = JL / (1 -  $\alpha$ );
 $\omega$  = 2 * Pi * f (*rad/s*);
[número pi]
cdg = 110 (1 -  $\alpha$ )3 * Rb; (*For slug flow - Lin, Y. et al, 2013*)
[para cada]
cvm = 3.3 + 1.7 *  $\left( \frac{\left(1 - \frac{\sqrt{\alpha}}{15}\right)}{\left(1 - \frac{\sqrt{\alpha}}{45}\right)} \right)$ ; (*Nicholson et al., 1978*)
ReL =  $\frac{\rho_L * VL * Diameter}{\mu_L}$ ;
Cf = FindRoot [encontra raíz]  $\left[ -4 * \text{Log}_{10} \left[ \frac{e}{Diameter} + \frac{1.256}{ReL * \sqrt{fm}} \right] = \frac{1}{\sqrt{fm}}, \{fm, 0.001\} \right]$  [logaritmo n base 10] [[1, 2]];

(*Collebrook, 1939*)

(*Matrix first line*)
a11 =  $\rho_G * (\omega - \kappa * VG)$ ;
a12 =  $\frac{\alpha}{aG^2} * (\omega - \kappa * VG)$ ;
a13 =  $-\alpha * \rho_G * \kappa$ ;

```

```

a14 = 0;

(*Matrix second line*)
a21 = -ρL * (ω - κ * VL);
a22 =  $\frac{(1 - \alpha)}{aL^2} * (\omega - \kappa * VL)$ ;
a23 = 0;
a24 = -(1 - α) * ρL * κ;

(*Matrix third line*)
a31 = ρG * VG * (ω - κ * VG) - i * ρG * g * Sin[θ];
a32 =  $\frac{\alpha * VG}{aG^2} * (\omega - \kappa * VG) - \kappa * \alpha$ ;
a33 = α * (ρG + cvm * ρL) * (ω - κ * VG) - ρG * VG * α * κ +  $\frac{3}{4} * i * \frac{cdg * \alpha * \rho L * VL}{Rb}$ ;
a34 = -cvm * α * ρL * (ω - κ * VL) +  $\frac{3}{4} * i * \frac{cdg * \alpha * \rho L * VG}{Rb}$ ;

(*Matrix fourth line*)
a41 = ρL * VL * (ω - κ * VL) - i * ρL * g * Sin[θ];
a42 = - $\frac{VL}{aL^2} * (1 - \alpha) * (\omega - \kappa * VL) + \kappa * (1 - \alpha)$ ;
a43 = cvm * α * ρL * (ω - κ * VG) +  $\frac{3}{4} * i * \frac{cdg * \alpha * \rho L * VL}{Rb}$ ;
a44 = -ρL * ((1 - α) + cvm * α) * (ω - κ * VL) +
κ * (1 - α) * VL * ρL +  $\frac{3}{4} * i * \frac{cdg * \alpha * \rho L * VG}{Rb} + \frac{4}{Diameter} * i * Cf * \rho L * VL$ ;

(*Determinant*)
Equation = Det[{{a11, a12, a13, a14},
{a21, a22, a23, a24}, {a31, a32, a33, a34}, {a41, a42, a43, a44}}];

(*Results*)
κ1 = Roots[Equation == 0, κ][[1, 2]] (*rad/m*)
κ2 = Roots[Equation == 0, κ][[2, 2]] (*rad/m*)

```

Section 4: Results

$$\begin{aligned}
 \text{In[]:= } c &= \frac{1}{2} * \left(\frac{\omega}{\text{Abs}[\text{Re}[\kappa1]]} + \frac{\omega}{\text{Abs}[\text{Re}[\kappa2]]} \right) \text{ (*Pressure propagation velocity*)} \\
 \eta &= \frac{1}{2} * (\text{Abs}[\text{Im}[\kappa1]] + \text{Abs}[\text{Im}[\kappa2]]) * \frac{1}{2 * \text{Pi}} \text{ (*rad→Np*)} * \\
 &\quad \frac{1}{0.1151} \text{ (*Np→dB*)} \text{ (*Attenuation coefficient in dB/m*)}
 \end{aligned}$$

APPENDIX E – MATLAB code to obtain the FFT

```

clc

clear all
close all

%import data from file
file=load ('Test1_Station1_CompleteSignal.txt');

%determine time range and frequency
N = length(file); %vector length
dt=100/N; %time step, change the numerator for the time
window
t=0:dt:100-dt; %time vector
dF=1/(N*dt);
F=1/dt; %sampling frequency
f=(0:dF:F-dF); %frequency vector
P=file(:,2); %pressure vector from file
Ut=file(:,3); %Traslational velocity vector from file

%Fast Fourier Transform
Pfft=fft(P);
MagPfft=abs(Pfft)/N;
Utfft=fft(Ut);
MagUtfft=abs(Utfft)/N;

%Write results in a txt file
Data=table(f',MagPfft,MagUtfft)
writetable(Data,'FFT_Test1_Station1_CompleteSignal.txt');

%Plots
figure (1)
plot(t,P)
title('Complete Signal - Pressure')
xlabel('time [s]')
ylabel('Pressure [kPa]')

figure(2)
plot (f,MagPfft)
title('FFT Complete Signal - Pressure')
xlabel('frequency [Hz]')
ylabel(' |Pressure| ')

figure (3)
plot(t,Ut)

```

```
title('Complete Signal - Ut')
xlabel('time [s]')
ylabel('Ut [m/s]')

figure(4)
plot (f, MagUtfft)
title('FFT Complete Signal - Ut')
xlabel('frequency [Hz]')
ylabel('|Ut|')
```